Luminescence at Defects in h-BN : Excitons at Stacking Faults and Single Photon Emitters

Romain Bourrellier

UNIVERSITÉ PARIS-SUD

ÉCOLE DOCTORALE 564 :
PHYSIQUE EN ÎLE-DE-FRANCE

Laboratoire de Physique des Solides

THÈSE DE DOCTORAT

PHYSIQUE

par

Romain Bourrellier

Luminescence at Defects in h-BN: Excitons at Stacking Faults and Single Photon Emitters

Date de soutenance : 28/10/2014

Composition du jury

Directeur de thèse :	Odile Stéphan	Professeur (Université Paris Sud)
Rapporteurs :	Quentin Ramasse	Professeur (Université de Liverpool)
	Jürgen Christen	Professeur (Université de Magdeburg)
Examinateurs :	Alberto Zobelli	Maître de Conférence (Université Paris Sud)
	Bernard Gil	Directeur de recherche (Université Montpellier)
	Jean-François Roch	Directeur de laboratoire (Université Paris Sud)

TABLE OF CONTENTS

CHAPTER 1

INTRODUCTION

SEMICONDUCTING materials have been over the latest fifty years one of the most important topics in both academic and industrial material science research. A long term effort on the study of the optical behavior of III-V and II-VI compounds made them to be extensively employed in current optoelectronic devices [1, 2]. After the discovery of the high efficiency and brightness of luminescent electron diodes (LED) based on AlGaN and InGaN alloys, great attention is posed now on III-V nitride (InN, GaN, AlN, BN). However, research on this class of materials is relatively recent and many fundamental questions remain still open. This can be mainly attributed to the very complex process required to synthesize III-V nitride and to control their crystalline level. It is the case, for instance, of GaN, the most commonly used nitride, which decomposes freeing N_2 before melting [3]. Usual synthesis methods can then not be employed and new techniques involving high pressure and high temperature had to be developed. Production of high quality crystals is however not yet fully mastered and samples might have a relative high defect density affecting their optical behavior. From another side, optical properties can also be deliberately tuned by producing structures of reduced dimensionality.

To achieve an in-depth understanding of the ultimate optical properties of semiconductor materials it is fundamental to be able to correlate at the atomic scale optical response and structure. Traditional optical methods are diffraction limited and they can provide only overall information at a sub-micrometric scale. The required spatial resolution for the study of defects in semiconductors can be achieved by transmission electron mi-

croscopy techniques. Electron microscopy can be combined with different spectroscopic techniques and thus, besides the topology of the system investigated, several physical properties may become accessible. The use of focused electron probes in scanning electron microscopes (SEM) and scanning transmission electron microscopes (STEM) permit to explore the optical response on a sub-wavelength scale. Through electron energy loss spectroscopy (EELS) in a STEM microscope, it has for instance been possible to map plasmon absorptions in the visible range within individual metallic nano-particles [4]. Recombination phenomena can also be explored by acquiring cathodoluminescence signals [5, 6]. Compared to absorption, luminescence peaks are intrinsically sharper and thus may provide more accurate information on the optical and/or electronic properties of the material of interest. In particular, CL has been massively employed for studying III-V hetero-structures and their optical active defects, with a recent focus on III-nitrides. This is the case for hetero-structures such as quantum dots [7, 8], quantum wells [9, 10, 11] or quantum wires [12, 13] and for defects such as dislocations [14, 15, 16, 17] or stacking faults [18].

Besides the high spatial resolution, cathodoluminescence with high energetic electrons has also the fundamental advantage to be able to excite high energy states where optical techniques would require short wavelength lasers. The capability of CL to access to the UV and far UV range is thus solely limited by the collection optical chain, the spectrometer and the acquisition camera.

The most energetic radiations that can propagate in air without significant attenuation are in the far UV region (4.4-6.3 eV). There is thus a strong technological interest in efficient light emitting devices in this spectral window for applications going from microbial sterilization to surgery tools. The well known drawbacks of standard UV lamps (poor lifetime, limited output powers, chemical hazards) have provided strong motivations to search for a convenient solid state alternative. III-V nitrides are currently among the most promising candidates as optical sources in this energy range. Whereas AlN based LEDs emitting at 5.9 eV have been already built, their low efficiency, due to a high density of defects quenching

the emission, strongly limits their technological potential [19, 20]. In the last years, hexagonal boron nitride (h-BN) appeared among III-V nitrides as a promising alternative candidate for optoelectronic applications in the far UV region [21, 22]. BN based LED might be not realistic due to the difficulty to introduce shallow dopants in the system. However, an efficient BN based UV light emitter in the 5.3-5.9 eV energy range has been recently obtained using accelerated electrons as the pumping source [23].

BN is a synthetic material whose massive production in micrometric powders has been performed since the 1960s. Macroscopic crystals were successfully synthesized only in 2004 [21] through a complex process involving high temperature and pressure. Whereas other nitrides crystallize in a wurtzite form, the most stable BN allotrope has an hexagonal layered structure with atomic orbitals in an sp^2 hybridization state. h-BN has thus strong structural analogies with graphite and the same analogies can be found in derived low dimensional structures.

A great number of sp^2 carbon based nano-forms have been synthesized within the latest thirty years, to mention the discovery in 1985 of fullerenes [24], or in 1991 of carbon nanotubes [25]. This lead to many technological applications such as gas sensors, electron gun, transistors, Li-ion battery and composite material. More recently, the isolation of graphene flakes in 2004 and the experimental proof of their unique electronics properties has been awarded with the Nobel prize of physics in 2010 [26]. Boron nitride have followed a close evolution, and nano-form similar to those of carbon based have been obtained with a little delay. The BN nanotubes stability has been predicted in 1994 [27] and the first experimental evidences have been reported in 1995 [28]. The first h–BN mono-layer has been isolated in 2008 [29] through exfoliation from macroscopic crystals. Whereas the structure of BN materials can be compared to those of carbon systems, their electronic properties strongly differ. As for other B-V compounds such as boron phosphate or boron arsenide, h–BN and BN based nano-forms are indirect band gap semiconductors. The h–BN wide gap ($\sim$ 6.8 eV) makes it of no interest for electronic applications except for being the ideal substrates for graphene: all atoms at the h–BN are saturated

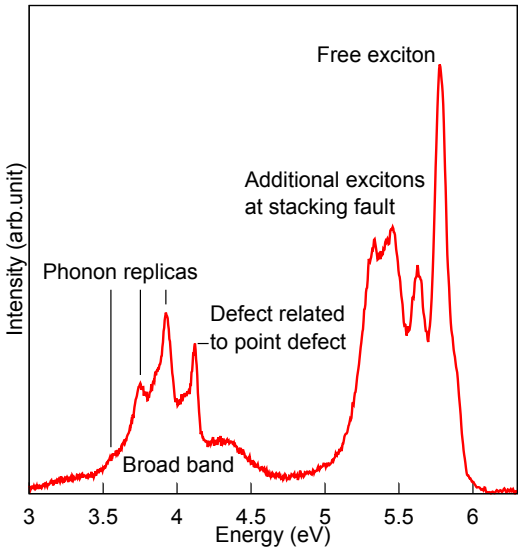

Figure 1.1: *Full cathodoluminescence spectrum obtained on a thin h-BN flakes. The two parts are visible, excitonic emission and middle of band gap emission.*

and thus no bonds can be formed with graphene preserving its unique electronic properties [30, 31, 32, 33].

Theoretical and experimental works have demonstrated that the emission spectrum of h–BN is dominated by a strong Frenkel type exciton at 5.75 eV [21, 22] making it highly interesting for UV optical applications. However, a single emission peak appears only in good quality macroscopic crystals that, as we discussed above, can be obtained only in a limited amount through high pressure and high temperature synthesis processes [34]. Common h–BN samples present a more complex emission spectrum with a series of sharp emissions close to the main exciton in the 5.3-5.9 eV energy range. An additional broad emission occurs within the electronic band gap in the energy range 3.2-4.5 eV on which a series of three sharp lines might be superposed depending on the BN sample purity [35, 36] (Fig. 1.1).

These spectral features indicate that defects have a fundamental role in defining the ultimate optical behavior of h-BN. In the latest years the structure of point defects in BN materials has been extensively studied by high resolution transmission electron microscopy. It has for instance be shown

that vacancies appear mainly in the boron sub-lattice and from these point defects more extended triangular holes can be grown [37, 38, 39], that few layer BN edges reconstruct forming nano-arches [40], that grain boundaries in BN mono-layer can have complex non hexagonal rings configurations [41], that stacking faults might occur in chemically exfoliated flakes [42].

Individual boron vacancies have also been studied by atomic resolved EELS spectroscopy showing changes of core edge fine structures for nitrogen atoms neighboring nitrogen [43]. Whereas numbers of works dealt with the structure of defects, their relation with the complex emission spectrum of h–BN remains still largely undetermined. Indeed, up to now no study has been reported combining optical measurements and structural analysis at the atomic scale. The aim of this thesis work has been to fill this lack of knowledge and to provide a new look on the optical behavior of BN based systems. To achieve this purpose an original approach has been adopted combing new cathodoluminescence methodologies resolved at the nanometric scale, high resolution transmission electron microscopy and state of the art theoretical spectroscopy simulations. Furthermore, the capability of highly resolved CL to address individual defects has been combined with interferometric techniques giving access to the quantum nature of specific emission peaks. This has shown that certain defects in boron nitride can be used as single photon emitters in the UV spectral region.

This thesis is structured as follows. The second chapter will introduce the structural properties of BN in its hexagonal phase and in derived nanoforms with a particular attention posed on synthesis procedures currently used by industry and research laboratories. Different exfoliation methods to obtain mono-layer flakes from bulk crystals will be also presented, emphasizing for each of them advantages and drawbacks and discussing purification thermal treatments. The chapter will conclude with a brief introduction to h-BN optical properties.

Chapter three will be dedicated to the presentation of the experimental techniques employed. In the first part, imaging modes in conventional

transmission electron microscopy and scanning transmission electron microscopy will be illustrated in relation to their use in this work. In the second part, the basic principles of Electron Energy Loss Spectroscopy, Cathodoluminescence and hyper-spectral imaging will be provided. The major differences between CL filtered image and CL fitted maps will be also discussed, showing the limits of CL filtered images to spatially separate emission signals with a close energy.

In chapter four we will discuss the h-BN emission spectrum in the high energy region and the occurrence of supplementary sharp peaks around the 5.75 eV free exciton. Combining CL and high resolution focal series in a STEM microscope we will show that these additional peaks are strongly localized along lines crossing the flakes that corresponds to layers folds. As for multiwalled BN-nanotubes, these folds facets leading to a discrete number of high symmetry stacking configuration different from the bulk one. Complementary theoretical spectroscopy simulations have allowed then to associate specific emission lines to local stacking changes. Finally we will show how the same situation can be encountered on multiwalled boron nitride nanotubes where different emission spectra correspond to different facets.

The fifth chapter will focus on middle band gap emissions which were attributed up to now to generic defects or impurities [35, 36, 34, 44, 45, 46, 47]. Through nanometric resolved cathodoluminescence we show that these emission are extremely localized within individual h-BN flakes, appearing as bright spots of only few tens of nanometer of width. The quantum character of these additional emission will be investigated using an Handburry and Brow Twiss interferometer coupled to our CL system and we will show that the 4.09 eV line correspond to a bright and fast single photon emitter source in the UV.

To conclude in chapter six we will discuss the perspective that this work might open, such as the role of stacking fault in low loss EELS or the search for new single photon emitters in other III-V semiconductors.

CHAPTER 2

STRUCTURE AND PROPERTIES

BORON NITRIDE was discovered by Balmain in 1842 by fusing boron sesqui oxide with potassium cyanide [48], but its true nature was determined and the compound prepared in a nearly pure state only later in 1850 by Wöhler [49]. Nowadays BN can be synthesized in various different phases: hexagonal BN (h-BN) and cubic BN (c-BN) phases, structurally close analogs to graphite and diamond respectively, and a wurtzite phase. Research on the synthesis of macroscopic crystals for these phases is currently a hot topic with numerous groups working on developing new synthesis processes. The case of h-BN is a typical example: up to now only a few groups in the world master the synthesis of perfect mono-crystals. Alternatively, commercial samples in few microns sized shape containing impurities are available in large quantity at low price. BN is already largely used in number of technological applications. As a matter of fact, due to its layered structure, h-BN is a very good candidate for applications in the lubricant field such as motors or turbines. Also h-BN applications cover various fields such as biological use in cosmetic products (white color) due to its chemically inert [50] character and its non toxicity. In this chapter, the structural properties of the different BN phases will be presented, followed by a description of the most used techniques of synthesis. Finally, the major physical effects involved in the optical properties of this material will be briefly described and an overview of the actual knowledge on h-BN optical properties from a theoretical and experimental point of view will be given.

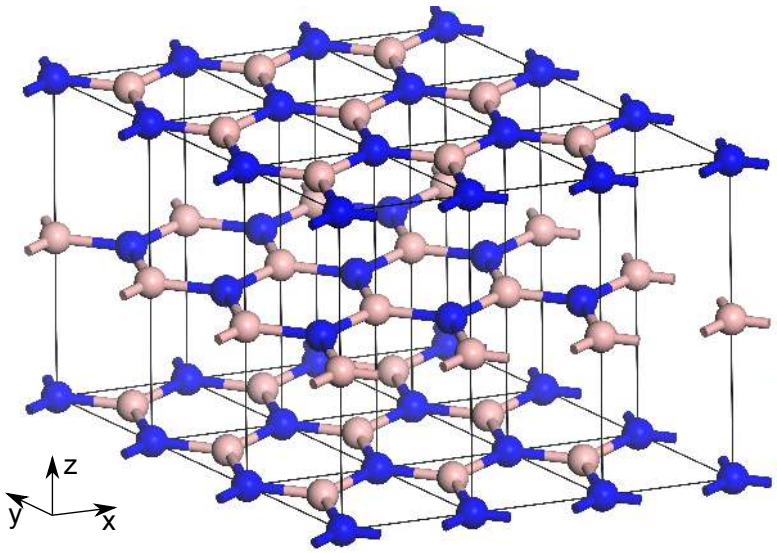

Figure 2.1: *Atomic structure of an h-BN crystal*

2.1 h-BN

The hexagonal phase of Boron Nitride has strong structural analogies with graphite, both crystals are constituted by piled up and weakly interacting mono-atomic layers (Fig. 2.1). Within the layers, atoms are arranged in hexagons, with an alternation of boron and nitrogen, leading to three covalent bonds per atom (bond length 1.44 Å, lattice parameters $a = b = 2.45$ Å). In graphite the AB stacking is obtained by translating every other layer by a vector $(\frac{1}{3}, \frac{2}{3})$. The AA′ stacking of h-BN is obtained by applying to every other layer a 180° basal plane rotation followed by a $(\frac{1}{3}, \frac{2}{3})$ vector translation. In this structure all atoms are thus arranged in columns alternating boron and nitrogen atoms, with an inter-layer distance of 3.3 Å. h-BN has been also reported to stabilize in ABC polytype, precursor of the cubic phase, or in more disordered pyrolitic phases.

2.1.1 Synthesis

Research of a high scalable industrial way to produce high quality crystals of layered materials is a burning issue. Commercial samples are available

in micrometer sized powder, but larger size crystals are still limited to research labs. However, the synthesis of macroscopic h-BN crystals is not yet fully mastered, despite a large number of studies. In this section, a short overview of the main line of the synthesis process currently employed for h-BN mono-crystal synthesis and comercial powder will be given.

Macroscopic mono-crystals The first synthesis of large sized h-BN mono crystals has been reported in 2004 by Tanagushi and coworkers (National Institute for Material Science, NIMS, Tsukuba, Japan) [51]. This new phase was obtained as a side product of experiments carried out to produce high quality BN cubic crystals. The synthesis process basically consists in pressing under 4-5 GPa at 1600 °C a h-BN powder in a barium boron- nitrate solvent ($Ba_3B_2N_4$). The crystal obtained are then a few hundreds of microns thick with a few millimeters lateral size (Fig. 2.2). Only the over mentioned Japanese group currently masters such a technique based on a complex and heavy equipment and it remains the only provider of perfect h-BN mono-crystals world wide. The high crystallinity level of such samples is reflected in their high transparency and absence of any absorption impurities in the optical spectrum. Only very recently an alternative commercial provider for millimeter sized mono-crystals have emerged, but synthesis details remain still protected.

Figure 2.2: ***Left**: picture of h-BN crystals synthesized by high pressure and high temperature process at NIMS, Tsukuba, Japan [34]. **Right**: crystal synthesized by a new commercial provider (HQ-graphene http://www.hqgraphene.com/). Both crystals are few millimeter sized and display a very high crystallinity level.*

Figure 2.3: *white micrometer sized powder of h-BN sold by a chemical provider*

Commercial available powders h-BN micrometer sized powders are produced at large scale using a basic chemical industrial reaction (Fig. 2.3). Boric acid (H_3BO_3, hydrate phase of boron oxide) or a natural borax mineral ($Na_2B_4O_7$-10 H_2O) are mixed at high temperature (more than 900 °C) in the presence of a nitrogen source (ammonia, melamine). The process leads to amorphous BN which is then recrystallized at a high temperature (1500-1600°C) under a nitrogen atmosphere. h-BN crystallites from a few hundreds of nano-meters up to few micrometers in size can be obtained. Others synthesis methods provide a powder of lower purity and crystallinity. The simplicity of the synthesis technique makes h-BN powder a rather cheap product which is thus massively employed in number of applications, from cosmetics to lubricants for technological applications.

2.2 Nanotubes

Layered material derived nano-forms have been known for about 30 years since the discovery in 1985 of carbon fullerenes [24] and in 1991 of carbon nanotubes [25]. The structural analogy between graphite and h-BN allows this latter material to be used as a precursor for other hexagonal

based nano-forms. The stability of boron nitride based nanotubes has been first theoretically proposed by Rubio *et al.* [52] and experimentally demonstrated in 1995 [53] shortly after the discovery of carbon nanotubes (Fig. 2.4). They can be described as a rolled up sheet of h-BN and they are structurally a close analog to carbon nanotubes. Diameters of h-BN nanotubes vary from a few nanometers for single walled tubes up to hundreds of nanometers for multi-walled. Their length can finally reach several micrometers. For multiwalled BN nanotubes, the inter tubular distance is about 3.44 Å, slightly above the inter layer spacing in h-BN.

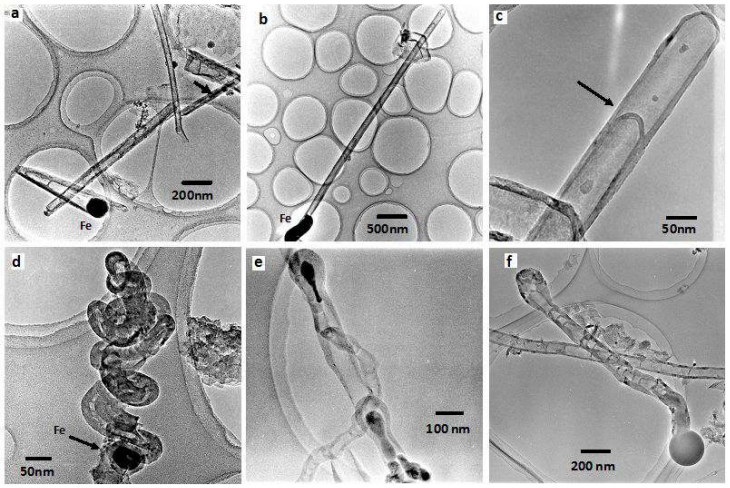

Figure 2.4: *TEM images of h-BN nanotubes [54].*

2.2.1 h-BN Nanotube synthesis

Multiwalled BN nanotubes have been successively synthesized by Chopra *et al.* [53] using a simple arc discharge technique and currently their production is routine in number of laboratories. The synthesis of single walled nanotubes is a more difficult task. Introducing catalytic particles in an arc discharge reactor Loiseau *et al.* [55] firstly obtained single walled nanotubes. Pioneering experiments on laser ablation of hexagonal or cubic BN targets were carried out by D. Golberg in 1996 [56], and then improved using a catalyst free process by Lee and co-workers in 2001 [57].

Arc discharge BN nanotubes were first discovered by Chopra *et al.* [53] analyzing the debris of an arc-discharge experiment using a hollow tungsten electrode filled by BN. One year later, Loiseau *et al.* [55], obtained a little amount of single walled nanotubes introducing catalytic particles in the electrodes and performing the experiment in a N_2 atmosphere using a graphite cathode and a HfB_2 anode. This alternative set up lead to higher quality tubes presumably due to the physical separation between the carbon electrode and the B and N sources. This latter process leads to the production of single walled BN nanotubes, a very hard to synthesize material, which has been used up to now only in a few specific applications such as piezoelectric devices.

Laser ablation Pioneering experiments on laser ablation of hexagonal or cubic BN targets were carried out by D. Golberg in 1996 [56], and then improved using a catalyst free process by Lee, Loiseau and co-workers [57]. A continuous CO_2 laser focussed on a target placed in a diamond anvil cell filled with liquid nitrogen. After squeezing of the diamond anvils, a super-high nitrogen pressure of 1020 GPa was generated inside a tiny chamber. A temperature of approximately 5000 °C was estimated on the laser-irradiated BN target surfaces, where dozens of short pure BN nanotubes were found to protrude from an amorphous melted BN residue. The drawback of the synthesis was a relatively small number of BN nanotubes compared to dominant standard amorphous, cubic, or hexagonal BN flakes. Later on, catalyst-assisted laser ablation experiments at high temperature were carried out, and multiwalled BN nanotubes were also generated.

Chemical Vapor Deposition (CVD) In 2005, Golberg and Bando synthesized BN nanotubes using a modified Chemical Vapor Deposition technique involving a multi-precursors process [58]. This method still remains as the most efficient technique for the synthesis of tubes and could be easily developed at an industrial scale. Synthesis is obtained in a furnace at 1100 °C in a two step process. First a metal oxide reacts with a boron

powder to form boron oxide B_2O_2. Afterward, ammonia is introduced and tubes are produced in the gas phase by the reduction of B_2O_2. Using MgO as the oxygen source gives a very poor yield [59] whereas a mixture of MgO and FeO increases the production [58]. This technique leads to the formation of multiwalled BN nanotubes with large diameters from 20 up to 100 nanometers. Recently a modified process using lithium oxide LiO_2, has been shown to provide nanotubes with smaller diameters and a lower number of walls [60].

2.3 Fullerenes

The formation of fullerenes with a reduced number of layers (typically 3) of BN was firstly reported by Stephan and co-workers in 1998 [61, 62]. BN nanotubes were subjected to *in situ* electron irradiation at 20 °C and 490 °C in a high resolution 300 kV transmission electron microscope (HRTEM). The formation of spherical cages was then observed and electron energy loss spectroscopy confirmed a B/N stoichiometry of 1. HRTEM images revealed that fullerenes had a rectangle-like shape when viewed in specific projections, unlike the quasi-spherical carbon fullerene morphology (Fig. 2.5). The carbon fullerenes curvature is obtained by introducing pentagonal rings in the hexagonal network. A similar structure in BN would lead to the formation of homo-nuclear bonds, which are strongly energetically unfavorable. It has thus been proposed that in BN fullerenes and BN nanotube caps, the curvature is obtained through square rings with no homo-nuclear bonds or eventually through paired pentagonal rings that minimize homo-nuclear bonds [63]. Whereas this later structure has been proposed to be energetically more stable, it has not yet been experimentally identified.

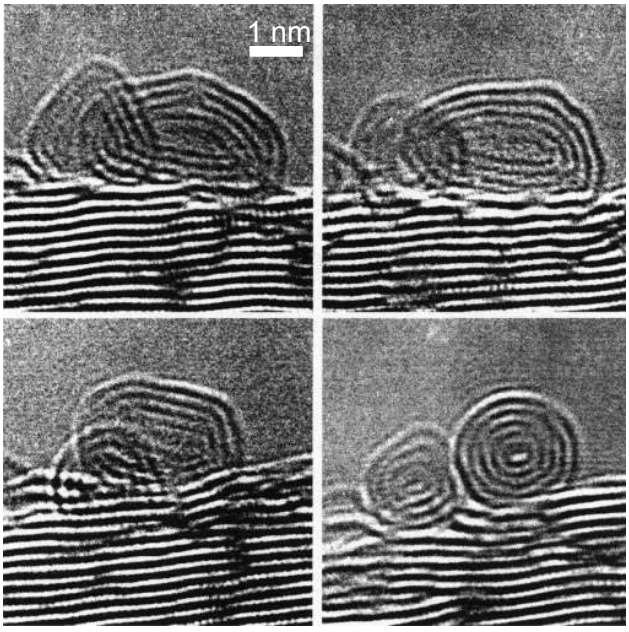

Figure 2.5: *TEM images of h-BN fullerenes [61].*

2.4 BN monolayers

Physisorbed h-BN on metal surfaces has been firstly obtained in 1995 by Nagashima and co-worker by epitaxial formation on Ni(111) [64]. However, only after the recent isolation of graphene, a large number of studies focused on the synthesis of these atomic thick crystals. In particular, this material is currently largely studied as a substrate for graphene since it allows to conserve its pristine transport properties. Furthermore, h-BN is integrated as an insulating layer in hetero-structures of layered materials. Pacile and co-worker in 2008 [65] obtained extended thin crystals of h-BN by mechanical exfoliation. Atomic thick crystals are anyway more difficult to obtain than graphene through this technique due to stronger inter-plan interactions and the difficulty to synthesize extended h-BN crystals. Thus other synthesis methods such as CVD, previously developed for graphene, are more commonly employed for the synthesis of h-BN monolayers.

2.4.1 Synthesis

In this section, different well known techniques used to produce mono-layer materials from bulk crystals will be presented. All these techniques consist in exfoliating the bulk of a layered material into thinner flakes or mono-layers.

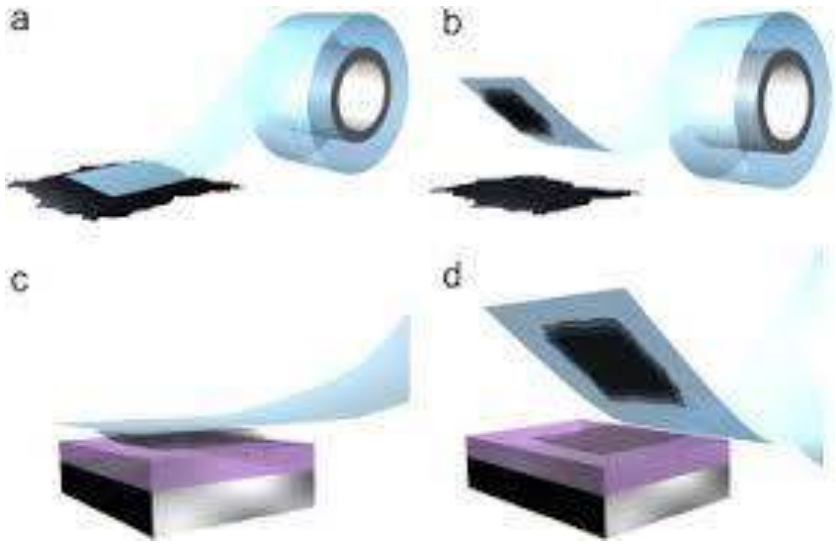

Figure 2.6: *Micromechanical exfoliation of 2D crystals.* ***a*** *Adhesive tape is pressed against a 2D crystal so that the top few layers are attached to the tape* ***b****.* ***c*** *The tape with crystals of layered material is pressed against a surface of choice.* ***d*** *Upon peeling off, the bottom layer is left on the substrate. [66].*

Mechanical peeling h-BN crystal is cleaved repeatedly with an adhesive tape until a mono-layer is obtained (Fig. 2.6). Formally, any kind of adhesive tape can be employed, but best results are obtained through the use of dust free clean room tapes, which leave less glue residues. The adhesive tape is afterward deposited on a silicon oxide substrate. After removing the tape, h-BN flakes are left on the surface. The flakes can be imaged by optical microscopy in order to identify their thickness by their color contrast on the substrate. Figure 2.7 displays h-BN flakes obtained in this work and deposited on a silicon oxide substrate. This image shows two flakes of similar shape, but of different thickness coming from the same

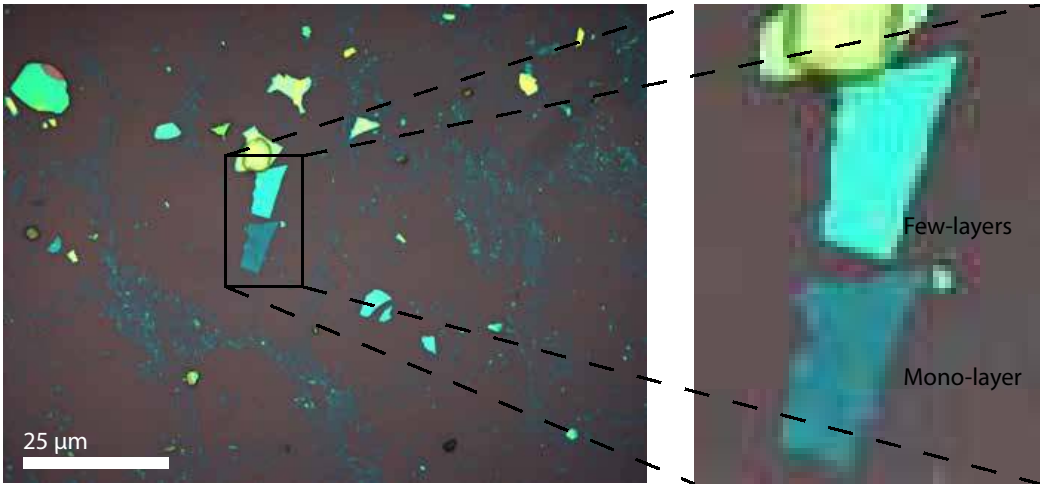

Figure 2.7: *SiO_2 wafer on which is deposited h-BN flakes, color contrast allow to distinguish mono from few layer h-BN.*

crystal. The transparent flake at the bottom is a mono-layer contrary to the upper flake, which displays a lighter color characteristic to a higher thickness. This technique is quite easy to set up, it does not need any heavy equipment. However, very large crystals should be preferred as precursor to obtain relatively large mono-layer flakes.

Chemical exfoliation Chemical exfoliation is a well known technique to produce few layer flakes in a cheap and highly scalable way. It was used for the first time in 1957 to exfoliate a water solution of graphene oxide crystals, produced by the Hummer's method [67]. Very recently, Coleman and coworkers have developed a chemical exfoliation protocol involving organic solvents valid for any kind of layered structures [68]. For h-BN, a micrometer powder is sonicated for a few hours in a solution of isopropyl alcohol, N-methyl-2-pyrrolidone or 1,2-Dichloroethane. During sonication, the organic solvent interposes between the layers which then separate (Fig. 2.8). Successively the solution is centrifuged and the supernatant (transparent part of the solution), which is mostly composed of thin flakes, is collected. This highly diluted solution is quite stable and it can be kept a few months without re-aggregation.

This technique is very easy to set up and to handle. The produced

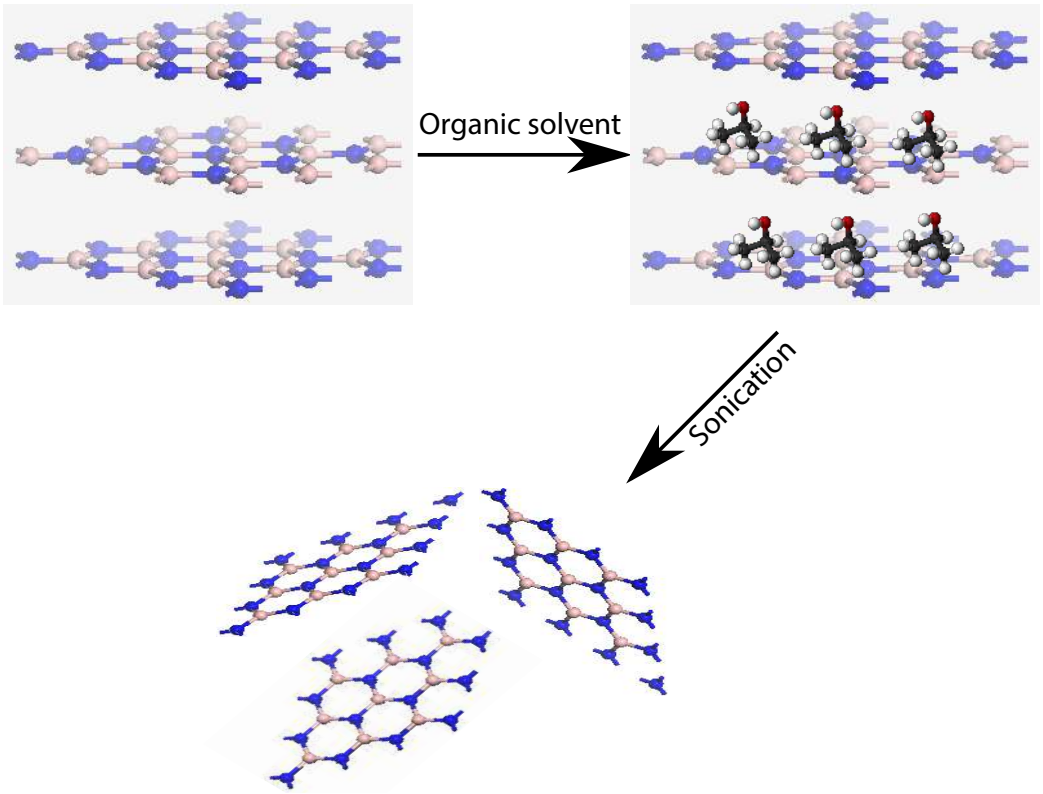

Figure 2.8: *scheme of the chemical exfoliation process.*

flakes are generally a few microns large and only a few layers thick with eventually mono-layer regions at the edges. However, large mono-layers are difficult to obtain because the sonication process tends to destroy them.

Anodic bonding Anodic bonding allows to exfoliate graphite by a dry process, avoiding any glue contamination contrary to standard mechanical peeling methods [69]. A layered material mono-crystal is deposited on a "Pyrex" glass substrate and placed between two electrodes. Afterward, a 1000 V potential difference is applied to the cathode connected to the substrate. This leads to a polarization of the glass substrate and a migration of Na^+ and O^- ions which bond to the crystal (Fig. 2.9). A sacrificial layer is formed by the bonding of the h-BN layer to the glass. After removal of the electrodes, only a few layer flakes are found to remain on the glass and optical microscopy can be used for a rapid control of their thickness and size. This technique produces only a few layers thick very large flakes (>10 μm). The drawback is the requirement of very large mono-crystals as precursors.

2.5 Sample preparation

For the purpose of Transmission Electron Microscopy (TEM) investigations, further sample preparation steps need to be undertaken. In this section, different techniques used to transfer the flakes from the substrate to an appropriate TEM support (TEM grid) will be presented. Furthermore, all techniques presented in the previous section introduce amorphous contamination at the surface of the h-BN flakes. We will also describe purification techniques used to remove this contamination and consisting in different thermal treatment under specific gas atmosphere.

2.5.1 TEM preparation

Direct transfer In order to have a sample transparent to electrons for subsequent electron microscopy observations, it is necessary to transfer

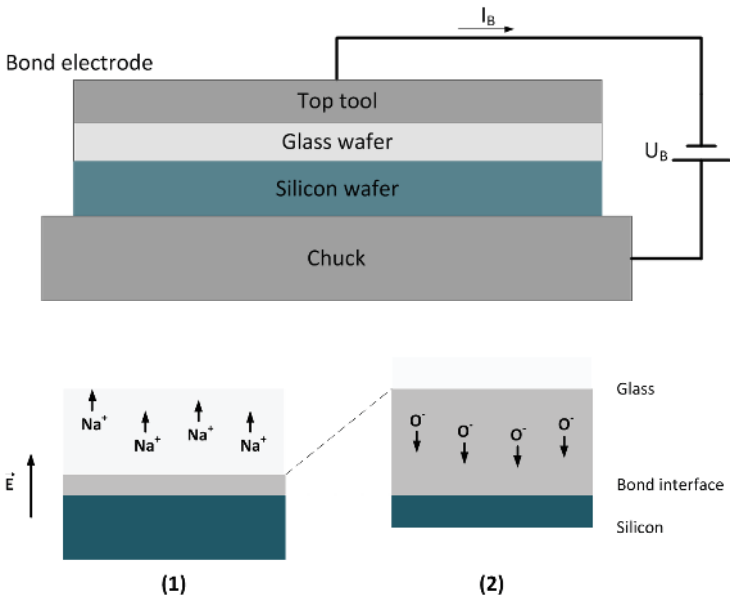

Figure 2.9: *Scheme of anodic bonding procedure. The top tool works as a cathode and the chuck as anode. Ion drifting in bond glass influenced by electrostatic field.* ***1*** *Formation of depletion zone (gray) through Na+ drifting.* ***2*** *Drift of O- ions in the depletion zone.*

the h-BN flakes from the substrate to a TEM grid. To do so, a home made wet transfer process has been developed, consisting in sticking the amorphous carbon web of the TEM grid to the silicon oxide substrate using an organic solvent (Methyl alcohol) while the substrate is heated at 60°C. The TEM grid is then removed at room temperature by casting an additional drop of the same solvent on it, which leads to the unsticking of the grid from the substrate. When the grid is removed, it collects part of the sticking h-BN flakes to the amorphous carbon web. This process can be repeated to increase the number of flakes needed on the TEM grid. Due to the weakness of the amorphous carbon web of the TEM grid, this technique is relatively difficult to set up and gives a low efficiency rate, mainly leading to breaking the amorphous web of the grid (Fig. 2.10). A higher efficiency can be obtained by relying on optical microscopy to select areas of interest on the substrate that contain mono-layer flakes.

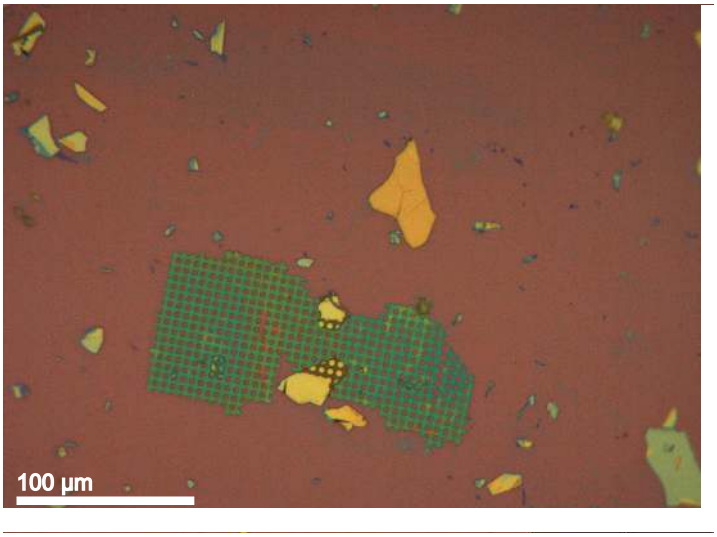

Figure 2.10: *Optical image of a SiO_2 wafer supporting h-BN flakes and part of a carbon film coming from a TEM grid after a failed transfer.*

Polymer transfer Another process, easier to set up, consists in collecting h-BN flakes from the substrate with a polymer. In this case, a hydrophobic polymer (C-tab) is used. A very thin polymer layer is spin coated on the substrate before it is emerged into water. The hydrophobic character of the polymer forces it to detach from the substrate and to float on the water surface. The polymer layer is then fished and deposited on the TEM grid where it is dissolved using the appropriate organic solvent (acetyl acetate). Samples collected by this technique are very thin (mono/bi-layers) and very large. This technique is easy to set up and gives very good results. However, the h-BN flakes are strongly covered by polymer residues. This contamination has therefore to be removed using a technique that will be described in the next section.

2.5.2 Thermal purification

The techniques presented in the previous sections lead to the production of good quality BN flakes, but with varying amounts of contamination in their surface, as clearly seen by TEM imaging (Fig. 2.11). This contamination needs to be eliminated for accessing to an unambiguous character-

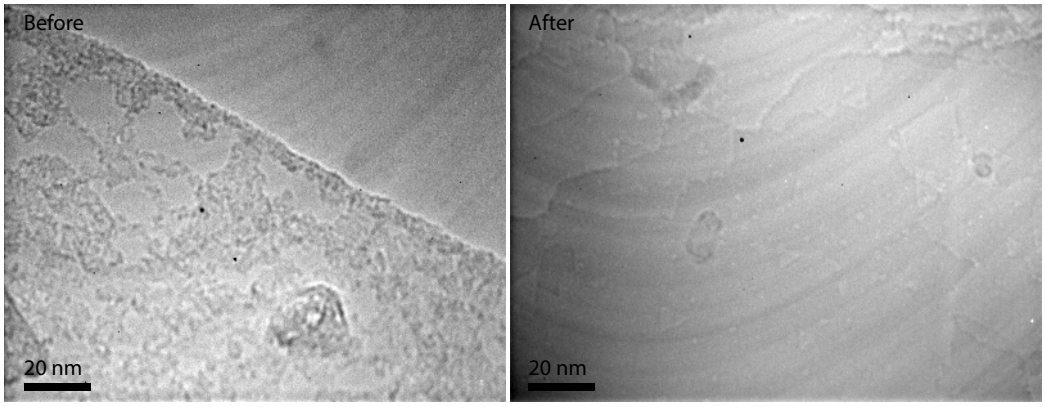

Figure 2.11: *TEM image of h-BN before and after thermal treatment where the complete removal of the contamination layer on the surface is clearly visible.*

ization of the intrinsic structural and optical properties of h-BN. A first try was made using a thermal treatment in vacuum (10^{-6}mbar) which leads to the formation of only a limited number of small areas free of contamination. A very efficient way was found by using a thermal treatment under a reductive atmosphere (forming gas: 5% H_2 and 95% N_2) at 400°C under a pressure of 500 mbar. After such a treatment, a complete removal of the contamination was observed (Fig. 2.11).

This thermal treatment is also used to remove residues coming from the adhesive tape glue used for mechanical peeling (Fig. 2.12).

2.6 Optical properties of h-BN

h-BN is a layered material with a sp^2 hybridization. Its band structure, at first look seems relatively similar to those of graphite. Hybridization within the layers appears between s, p_x and p_y electron states, and it forms σ bands responsible for the cohesion of the system. The third p orbital, p_z, orthogonal to sp^2 orbitals remain isolated and it generates the so called π band. Due to h-BN ionicity, a gap appears between the π bands (contrary to graphite).

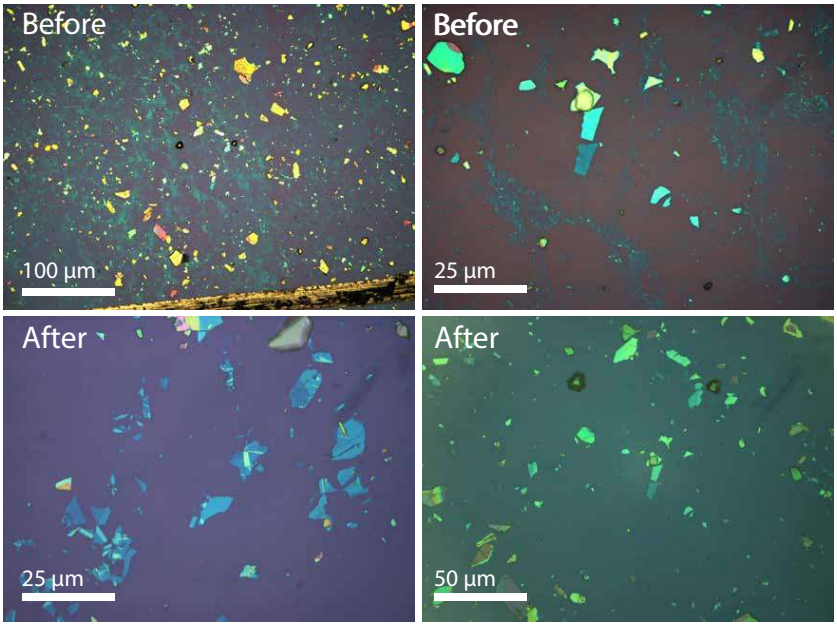

Figure 2.12: *Optical microscopy image of a SiO_2 substrate on which mechanically exfoliated h-BN flakes are deposited.*

2.6.1 *h*-BN band structure

Theoretical calculation of the *h*-BN band structure had been performed since the beginning of the 1950s [70]. These calculations predicted a direct gap using a tight binding calculation theory. In 1985 Catellani *et al.* [71] used an *ab-initio* approach based on the Density Functional Theory (DFT) and the Local Density Approximation (LDA). This calculation takes into account all the electrons in the system and predicts an indirect band gap of 5 eV. However, this work only gives valid energies for fundamental states. A more complete theory is needed. For example, a N body theory, using a Green function formalism, can be used. It introduces a dynamically screened interaction potential W (due to the screening of the Coulombian interaction between quasi- particles because of presence of hole cloud around the electrons). This method is also called GW [72]. The most recent and accurate determination of the *h*-BN band structure using this calculation was performed by Arnaud *et al.* [73] and Wirtz *et al.* [74] (Fig. 2.13). An indirect gap of 5.95 eV and a direct gap of 6.47 eV at H point (com-

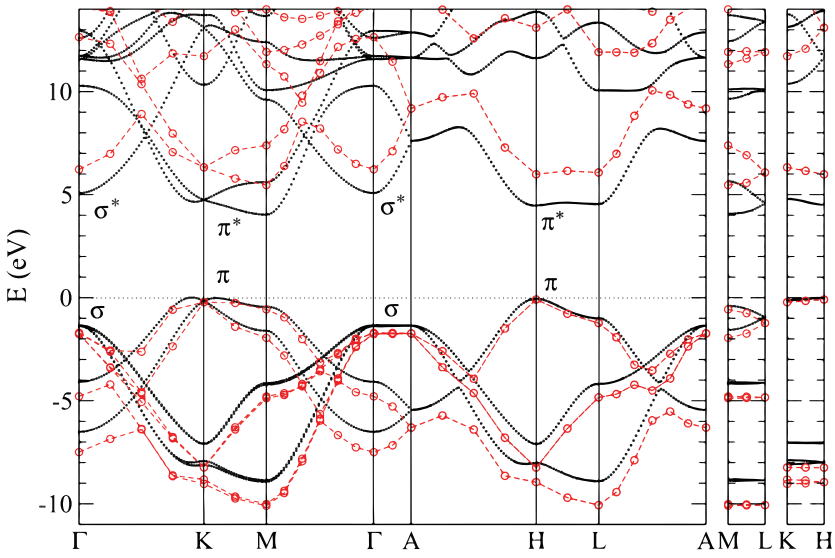

Figure 2.13: *electronic band structure of h-BN calculated using GW technique [74].*

pared to 4.02 eV and 4.46 eV respectively using LDA calculation) has been obtained by these authors. Using different approximations, Wirtz *et al.* predicted an indirect band gap between 5.53 ad 5.99 eV and a direct band gap between 6.03 and 6.48 eV [74].

From an experimental point of view, only a few papers discuss the gap energy of *h*-BN and the proposed values are very disparate (from 3.2 to 6.3 eV). First optical measurements of the optical band gap were reported in 1950s using reflectivity techniques, electro-luminescence and photoluminescence with specific detection equipments adapted to UV [75, 76, 77]. In 1976, Zunger *et al.* [78] published a study performed on a 100 nm thick *h*-BN film synthesized by CVD. The optical absorption spectrum gives the first experimental proof that *h*-BN is a large gap semiconductor, with a gap around 6 eV. An emission spectrum showing features peaking at energies higher than 5 eV has been recorded by Taylor *et al.* [79] using cathodoluminescence on a *h*-BN film deposited on a silicon oxide substrate. This work shows emission peaks at 4.9 eV, 5.31 eV and 5.5 eV and no shift in energy when the temperature varies from 4.2 K to 250 K. An emission signal is also detected around 4 eV peaking at 4.4 eV, 3.84 eV and 3.4 eV

attributed by the authors to deeper transitions in the gap. Then in 2004 a luminescence experiment by Watanabe *et al.* [51] performed on a pure single mono-crystal of h-BN showed a strong luminescence peak at 5.8 eV. This work increased the interest of researchers for h-BN as a good candidate for applications in the far UV range. This huge luminescence appears stronger than the one seen in diamond or cubic BN crystals. Further investigation of the optical properties of BN shows additional emission peaks around the exciton emission at 5.8 eV together with an emission band around 4 eV. Up to now the true origin of the additional emission is not clear. In this thesis, we will combine spatially resolved cathodoluminescence to HREM and mechanical quantum calculation to investigate the correlation between the additional emission and specific defects in the structure of the h-BN material.

2.6.2 Excitonic transition in h-BN

Wannier-Mott excitons In semiconductors, the dielectric constant is generally large. Consequently, electric field screening tends to reduce the Coulomb interaction between electrons and holes. The result is a Wannier exciton [80], with a radius larger than the lattice spacing. The effect of the lattice potential can thus be incorporated into the effective masses of the electron and hole. Likewise, because of the lower masses and the screened Coulomb interaction, the binding energy is usually low, typically on the order of 0.01 eV. This type of exciton was named for Gregory Wannier and Nevill Francis Mott. Wannier-Mott excitons are typically found in semiconductor crystals with small energy gaps and high dielectric constants, but have also been identified in liquids, such as liquid xenon.

Frenkel excitons In materials with a small dielectric constant, the Coulomb interaction between an electron and a hole may be strong and the excitons thus tend to be small, of the same order as the size of the unit cell. Molecular excitons may even be entirely located on the same molecule, as in fullerenes. This Frenkel exciton, named after Yakov Frenkel, has a typi-

cal binding energy on the order of 0.1 to 1 eV. Frenkel excitons are typically found in alkali halide crystals and in organic molecular crystals composed of aromatic molecules, such as anthracene and tetracene.

Despite standard nitride emission can be usually interpreted using the Wannier model, *h*-BN seems to display a peculiar behavior. Although, the first experimental results of photoluminescence performed on high quality *h*-BN crystals by Watanabe *et al.* [51] in 2004 (Fig. 2.14) had been interpreted using this model, ab initio calculations by Wirtz [74] and Arnaud [73] contradicted this later interpretation. These calculations take into account electron-hole Coulomb interaction using Bethe-Salpeter equation and predict strong excitonic effects in *h*-BN with an exciton binding energy of 700 meV. However, these calculations assumed non moving atoms (frozen atom picture). Marini *et al.* [81] showed afterward that vibrations (and exciton phonon coupling) have to be taken into account, even a 0 K. Such effect lowers the binding energy to 520 meV (at 0 K).

Arnaud *et al.* has calculated the wave function of the exciton fixing the position of the hole and calculating the probability of finding the electron. They show that the exciton stays in the hexagonal plan and that it is strongly localized within it. All these elements are in good agreement with the hypothesis of a *h*-BN exciton of Frenkel type.

2.6.3 *h*-BN nanotubes

Using GW calculation, Blase *et al.* [27] showed that whereas carbon nanotubes can be metallic or semiconducting depending on the rolling direction and radius, BN nanotubes are all semiconductors and their gap is not dependent of their diameters. According to this calculation, this gap non-dependence with the diameter of the tube do not work for small ones (less than 95 nm diameter). BN nanotubes optical properties have been studied experimentally using several techniques such as optical absorption and Electron Energy Loss Spectroscopy (EELS). In 2005, Arenal *et al.* [82] performed EELS on isolated nanotubes and estimated the optical band gap of single walled, bi-walled and three-walled BN nanotubes

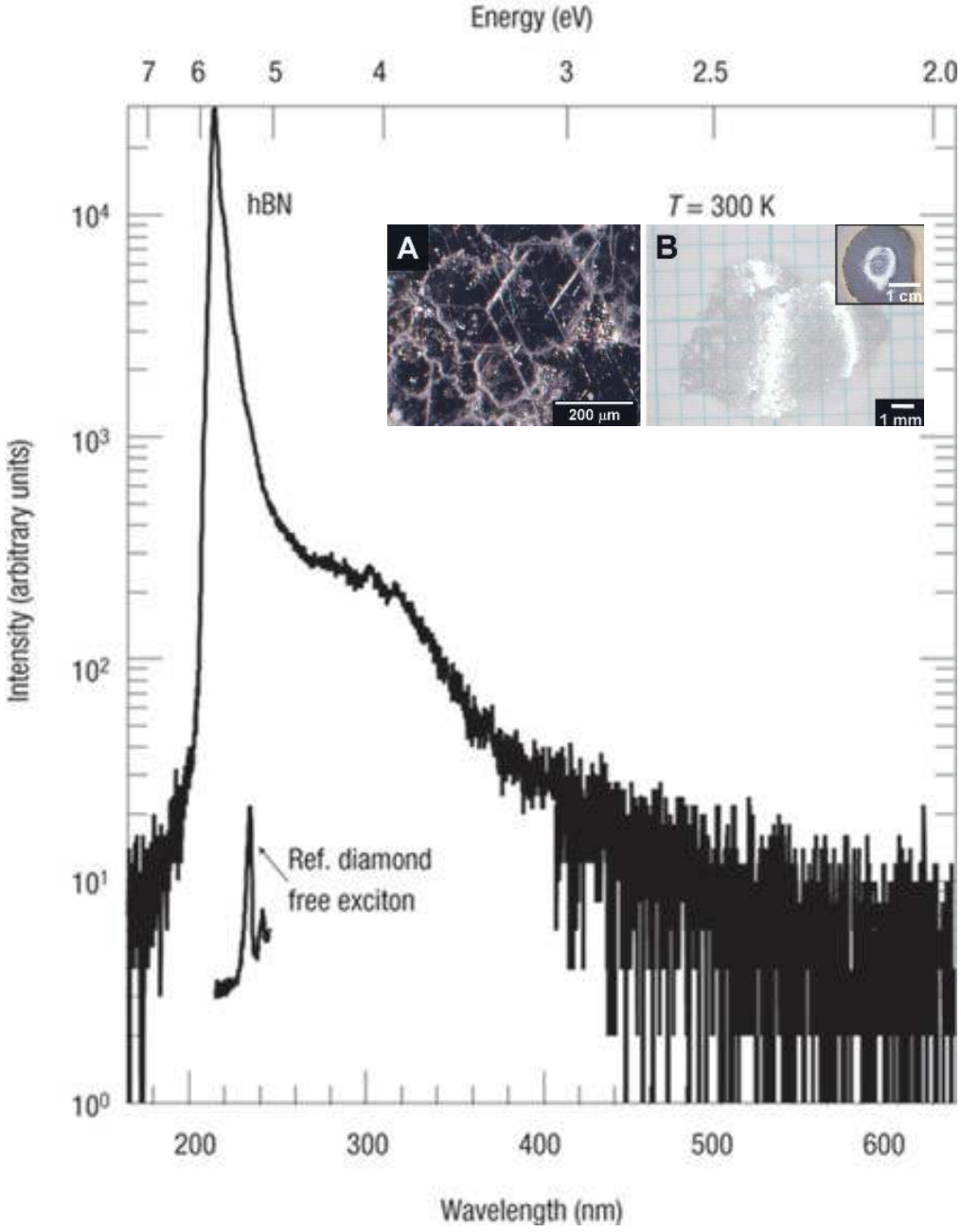

Figure 2.14: *Luminescence spectrum obtained on a perfect h-BN crystal (spectrum extracted from [51]).*

to be around 5.8 eV. This work has been conducted in the framework of the thesis of Raul Arenal at the Laboratoire de physiques des solides, Orsay. Alex Zettl's team performed the first luminescence experiments on BN multi-walled nanotubes. In this study, they compared luminescence spectra of BN nanotubes excited at 244 NM, BxCyNz nanotubes and standard h-BN crystal. All spectra show a similar luminescence band around 4 eV. Based on a lifetime study of the probed excitations, they attributed this emission to inter-band transitions and estimated the gap of h-BN and BN nanotubes as around 4 eV. Zhi *et al.* [83] then performed cathodoluminescence measurements on multi-walled BN nanotubes and saw an intense emission around 3.3 eV and a smaller one at 4 eV. They proposed the same interpretation, however, they supposed that this emission could originate from transitions of defect levels in the gap. A more recent study measuring the absorption spectrum on macroscopic samples of multi-walled BN nanotubes performed by Lauret *et al.* [84] showed 3 absorption bands at 4.45 eV, 5.5 eV and 6.2 eV. The authors provided the following interpretation: the 4.45 eV band is associated to an exciton of high binding energy (Frenkel), the 5.5 eV band to van Hove singularity absorption and the 6.2 eV band to h-BN inter band transition. This Interpretation will be discussed further in Chapter 3 of this manuscript.

h-BN material displays very interesting optical properties in the far UV. It displays a very complex emission spectrum covering a large energy range (from 4 eV to 6 eV) dominated by a very strong excitonic emission peak at 5.75 EV characterized as associated to a Frenkel exciton. This thesis will investigate these optical properties at a nanometric scale. Using the different techniques described in this chapter, we are now able to rely on very good quality samples to perform such a study at a nanometer scale on well crystallized and isolated flakes. The techniques used for characterization will be described in the next chapter.

CHAPTER 3

CHARACTERIZATION TECHNIQUES

THIS THESIS is investigating the structure of defects in h-BN materials and their associated optical properties both from a theoretical and an experimental point of view. In particular, we combine transmission electron microscopy with spatially resolved cathodoluminescence and quantum optics methodologies. This chapter will give a basic overview of all the experimental techniques employed. In the first part of the chapter, we will rapidly describe microscopy imaging techniques: standard transmission electron microscopy, used for a quick characterization of synthesized h-BN flakes (Sec. 3.1.1), and STEM microscopy with elements on spherical aberration correction, employed for more advanced structural characterizations (Sec. 3.1.2). The second part of the chapter will be focused on spectroscopic techniques within a transmission electron microscope. We will thus provide the basis of electron energy loss spectroscopy and more recent cathodoluminescence techniques implemented within a STEM microscope. To conclude, at the end of the chapter, we will describe the coupling of an Handburry Brown and Twiss interferometer to a STEM microscope for nanometric resolved quantum optics experiments.

3.1 Imaging techniques

Imaging a small object always confronts to resolution problems directly linked to the radiation used and to the aberrations of the optical system. Progresses in electron lenses have allowed to overcome the resolution limit

of classical optical microscopy by employing accelerated electrons as the imaging radiation. In 1931 Ernest Ruska built a 10 nm resolution microscope, opening the field of electron microscopy. The resolution obtained was not as high as predicted due to the high chromatic aberrations of the electronic lenses used. Ernst Ruska was awarded with the Nobel prize in Physics in 1986 for this development. Recent spectacular progresses in the electron emission field and in aberration correction of electron lenses have allowed to reach resolutions below 1 Å in modern TEM.

3.1.1 Conventional TEM

In Figure 3.1 we provide a simplified schematic representation of a conventional transmission electron microscope (TEM). A field emission gun emits a stream of monochromatic electrons that are accelerated at an usual operating energy in the range between 80 and 300 keV. These electrons are then converted by a system of condenser lenses into a thin parallel beam. At this stage, the beam is restricted by a condenser aperture, knocking out electrons diffused at a high angle (those far from the optic axis). Afterward, the beam illuminates the sample and it is partially transmitted. An objective lens focuses the transmitted electrons generating an image which is successively enlarged by several intermediate and projector lenses. In the diffraction mode, the focal plane is projected. The final image is observed on a phosphorus screen or on alternative detection systems such as photo films or CCD (charge-coupled device) cameras. Several optional objective and selected area metallic apertures can restrict the beam respectively at the focal or image plane. In the bright field operation mode the objective aperture enhances the contrast by blocking out high-angle diffracted electrons. In the diffraction mode, the selected area aperture allows the user to examine the diffraction pattern of electrons scattered by limited regions of the sample while maintaining a parallel electron beam. Compared to conventional microscopy, high resolution transmission electron microscopy (HRTEM) does not use only amplitudes for the image formation, i.e. absorption by the sample. On the contrary, the contrast arises

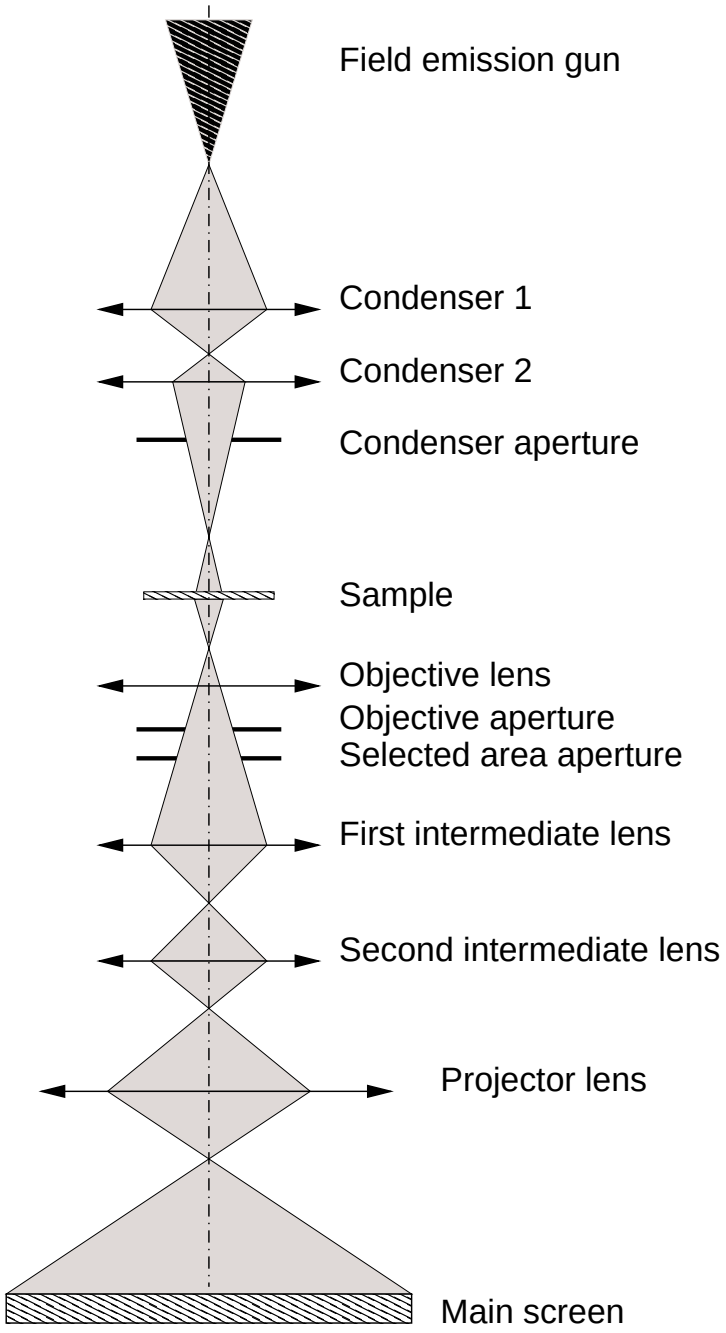

Figure 3.1: *Schematic representation of a conventional TEM microscope.*

from the self-interference in the image plane of the electron wave with itself. This allows to image crystallographic or amorphous structures at an atomic scale and makes HRTEM one of the main tools for morphological and structural studies of solids, nano- structures and biological samples. This interference process resulting in high resolution image formation has been described in several text books (see for instance [85]) and we will give here just a few elements of it. At the sample surface, the wave function of an incident electron can be approximated with a plane wave. The electronic plane wave invests homogeneously the specimen which diffracts in a set of plane waves whose frequencies correspond to the distribution of spatial frequencies of the sample crystal structure. For thin specimens, such as h-BN flakes (light elements and a limited amount of projected atoms), the plane wave function experiences a position dependent phase shift that is related to the total projected atomic potential of the specimen. Absorption effects can be neglected (weak phase object approximation). A frequency dependent dephasing is then introduced by spherical aberrations and the defocusing of the microscope optics. An image is finally produced whose contrast arises from the interference between different diffracted waves. For a HREM-TEM system, several resolution limits may be defined such as point resolution and information limit. Point resolution is defined as the smallest detail that can be interpreted directly from the experimental images in terms of structure, provided that the object is very thin. The information limit represents the smallest detail that can be resolved by the instrument. It is inversely proportional to the highest spatial frequency that is still transferred with appreciable intensity to the image plane from the electron wave field at the exit plane of the specimen.

Experimental set-up High resolution images presented in this work have been obtained with an Akashi Topcon EM-002B transmission electron microscope. This instrument can operate in the 60-200 kV voltage range and has a point-to-point resolution of 0.19 nm. It is equipped with a $\pm 10^{\circ}$ double-tilt specimen holder and it has small probe micro-diffraction capabilities. The pole piece has a spherical aberration of $C_s = 0.4$ mm and a

chromatic aberration of $C_c = 0.8$ mm. The electron source used is a heated LaB_6 tip. The usual nominal vacuum in the vicinity of the sample is around $3 \cdot 10^{-7}$ torr.

3.1.2 Scanning Transmission Electron Microscopy

A schematic representation of a STEM microscope is given in Figure 3.2. Electrons are emitted by a cold field emission gun (FEG) which gives a natural energy width of the electron beam as low as 0.3 eV. A system of electromagnetic lenses focuses the electron beam on the surface of the specimen forming a sub-nanometric probe. Typical STEM microscopes have a small beam convergence angle of around 15 mrad leading to relatively small probe sizes of about 0.5-1 nm. Recent advances in spherical aberration corrections for electromagnetic lenses allow to operate with higher beam convergence angles to obtain sub Angstrom probe sizes. The scanning of the electron beam at the surface of the sample is guaranteed by two coils sitting before the objective lens. Oppositely to conventional TEM microscopes, there are no additional optics after the objective lens in the old setup of dedicated STEM. A series of detectors allows to collect at different angles the electrons elastically or in-elastically scattered.

In STEM microscopes, images are formed sequentially by scanning with the electron probe the surface of the sample and thanks to a synchronized collection of the signal which is generated by a volume defined by the lateral size of the probe and the sample thickness. Images can be registered in different modes using detectors positioned at different angles with respect to the optic axis. Bright field images are obtained by collecting part of the transmitted beam at a low angle, close to the microscope axis. Similarly to standard transmission electron microscopy, the signal results from a coherent process leading to interference effects. High Angle Annular Dark Field images (HAADF) are, on the contrary formed by collecting electrons scattered at high angles. This is possible using a detector centered on the optic axis of the microscope and having a hole at its center. The HAADF intensity depends on the composition, thickness and density

of the sample and it can be estimated according to the formula:

$$I_{el} = I_0 \rho t \sigma_{el} \tag{3.1}$$

where I_0 is the incident beam intensity, ρ is the atom density in the analyzed volume, t is the sample thickness and σ_{el} is the elastic cross section. This last term has a dependence on the atomic number of the target atom given by $Z^{4/3}$. Thus, thicker or densier zones of the sample appear on the images as brighter regions on a darker background. When channeling effect ca be neglected, HAADF images deliver a direct information on the morphology of the nano-object analyzed and they can be used for measuring the quantity of matter at different regions of the specimen.

VG-HB501 In this thesis work, the cathodoluminescence and EELS experiments have been performed in a VG-HB501 STEM microscope equipped with a tungsten cold field-emission gun (Vacuum$10^{-}11$ Torr). The vacuum in the vicinity of the sample was around $5 \cdot 10^{-8}$ torr and it has been obtained with an oil-free pumping system. High mechanical sample stability was obtained by a top-entry sample holder system and the sample stage is cooled at a temperature around 150 K realized after a homemade design. The beam convergence half-angle was set to about 7.5 mrad and the used pole piece has a spherical aberration of $Cs = 3.1$ mm. This corresponds to the formation of an electron probe of around 0.8 nm in diameter at the sample surface for a voltage energy of 100 keV. Electron probe sizes were slightly degraded when lower voltages such as 60 or 80 keV were employed. Bright field (BF) images have been obtained with a collection semi-angle of 1.25 mrad and dark field (DF) images have been obtained with a collection angle between 25 and 200 mrad.

USTEM 200 High resolution scanning transmission electron microscopy experiments have been performed in a NION USTEM 200 equipped with a tungsten cold field-emission gun. The vacuum in the gun is typically in the low 10^{-11} torr range and in the vicinity of the sample the vacuum is

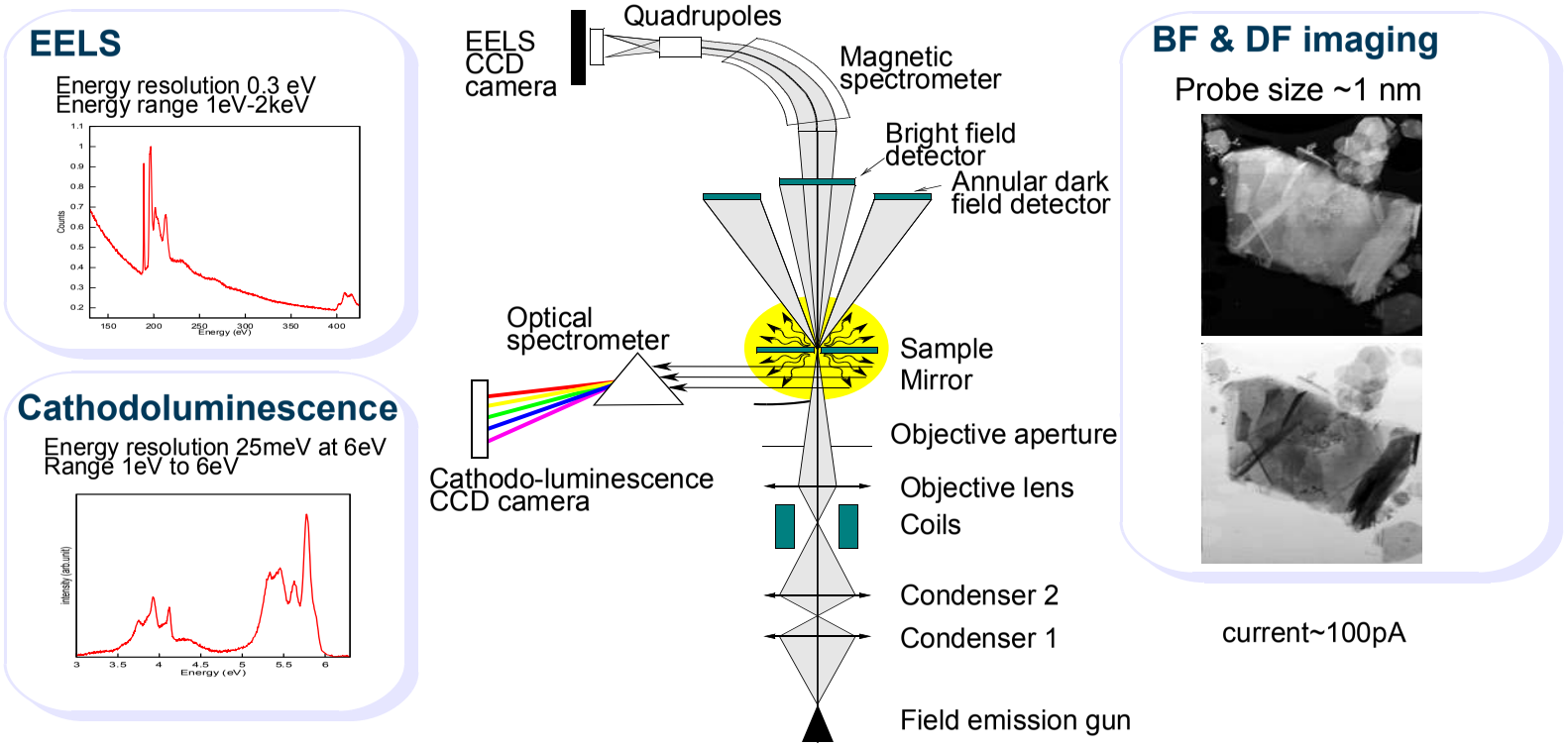

Figure 3.2: *Schematic representation of the VG microscope at the LPS. In the side inserts there are examples of images and spectroscopic signal collectable with this equipment.*

around $1 \cdot 10^{-9}$ torr. The microscope is equipped with an oil-free pumping system. The beam convergence half-angle was set to about 30 mrad. The used pole piece has a spherical aberration of $C_s = 1.1$ mm, zeroed thanks to the aberration corrector and a chromatic aberration of $C_c = 0.95$ mm. For an electron beam energy of 100 keV, it is possible to obtain an electron probe of less than 1 Å in diameter. Electron probe sizes were slightly degraded when the voltage was lowered at 60 keV to decrease radiation damage. Bright Field (BF) images have been obtained with a collection semi-angle of 40 mrad and Dark Field (DF) images have been obtained using a collection angle between 80 and 240 mrad.

3.1.3 h-BN flakes characterization through electron microscopy

Within this work, conventional TEM microscopy was extensively used to optimize the parameters for h-BN chemical exfoliation. TEM microscopy allows indeed a rapid look at the flake lateral size, thickness and surface cleanness. Amorphous contamination on the flake surfaces comes mainly from organic solvents used in the exfoliation and it strongly depends on the type of chemicals employed. TEM microscopy has proved to be very useful to identify the most appropriate solvent, i.e. leaving the lowest amount of residues and to monitor the effect of thermal purification dependently from pressure, time and temperature parameters (Fig. 2.11).

In order to minimize electron irradiation effects, all TEM images have been acquired using the Topcon at an operating voltage of 100 kV. Whereas this value is above the emission energy threshold for boron nitride [86], damages were still limited within the acquisition time.

Higher resolved images of the flakes were obtained by the spherical aberration corrected NION USTEM 200 microscope. This equipment maintains a sub-Angstrom resolution at an acceleration voltage as low as 60 kV, thus granting minimal irradiation effects. Z contrast in HAADF images allows to distinguish boron and nitrogen atoms in h-BN mono-layers regions (Fig. 3.3.a,b). In bi-layer regions, all atomic sites have the same

contrast due to the alternation of B and N atoms along the c axis. Atomic resolution can hardly be obtained in HAADF images for thicker regions of the sample where high resolution bright field STEM microscopy was employed instead. Finally, depth dependent information on the flake structure were obtained by bright field focal series.

3.2 Spectroscopy in a STEM

As discussed above, STEM microscopy allows to scan the sample with very small electron probes. Dependently with detectors equipping the microscope, several spectroscopic information can be acquired synchronously with images. An hyper-spectral or spectrum image can then be built with nanometric or even atomic resolution. Electron spectrometers are commonly installed in STEM microscopes. Energy loss spectra can then be recorded in an energy range going from the visible to the soft X-rays (1 eV to 2500 eV). EELS provide local information on the optical absorption behavior of the sample or its chemical nature. Less commonly, STEM microscopes can be employed also for cathodoluminescence providing a complementary information to EEL spectroscopy [87]. In this section we will give a brief overview of spectroscopic techniques employed in this thesis work.

3.2.1 EELS

Electron Energy Loss Spectroscopy is a technique which consists in measuring the energy lost by an electron inelastically scattered by the sample. Most of the time EEL spectroscopy is performed within a transmission electron microscope. The basic physical principle can be described in a rather simplified way. A monochromatic electron beam illuminates locally the sample and it induces an excitation of energy ΔE to which corresponds an equivalent loss of kinetic energy of the incoming electron. Measuring this energy loss through an electron spectrometer gives access to the energy characteristics of the excitation. This technique allows to cover

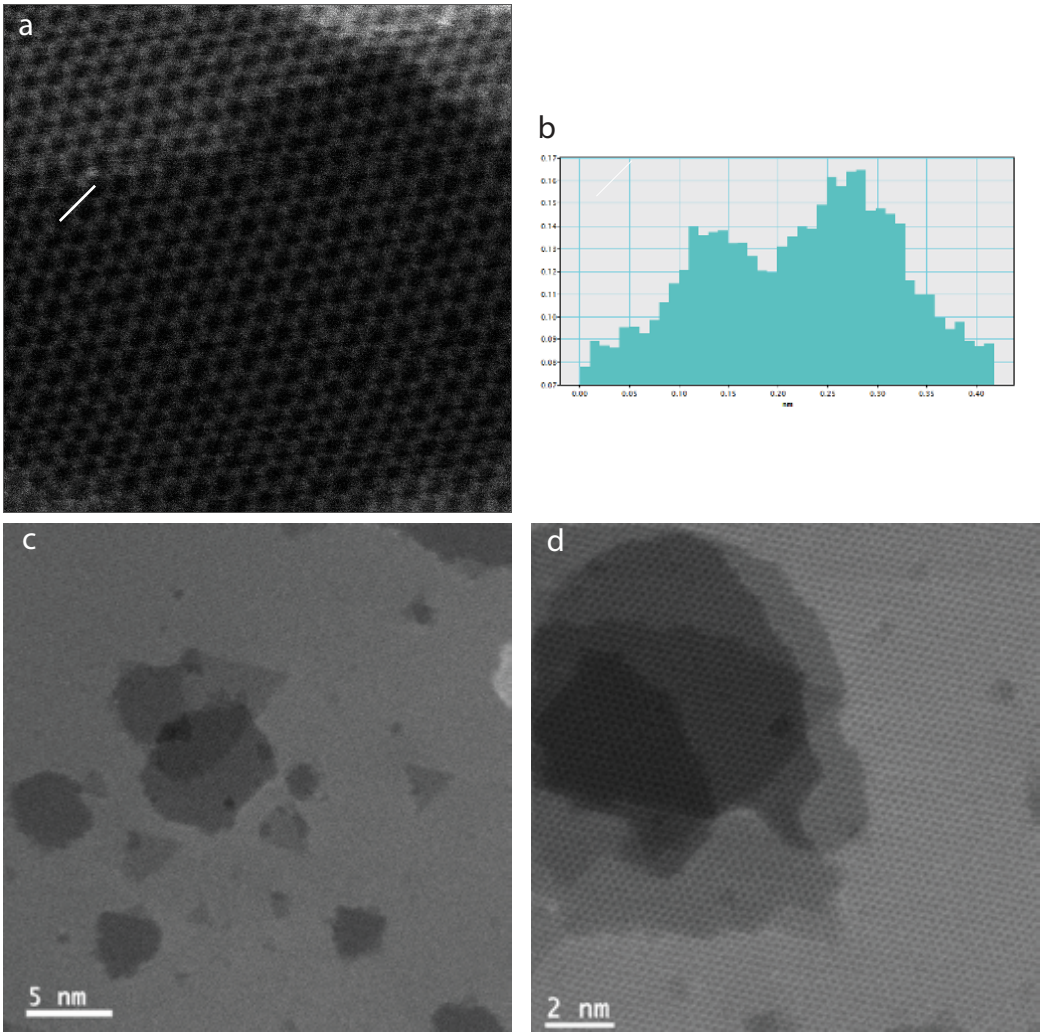

Figure 3.3: ***a,c,d*** *High resolution HADF image obtained with the USTEM 200 operating at 60keV of an h-BN few layers flake. In the image, regions with different number of layers are clearly visible.* ***a*** *In the mono-layer region it is possible to distinguish the alternating of boron and nitrogen atoms on the intensity profile (**b**). These contrast difference is then lost in bi-layer regions and only partially recovered for tri-layer regions.*

an energy range of about 2 keV going from the visible to the soft X-rays. The overall spectrum can be described by dividing it in different regions (Fig. 3.4). The lowest energy part, around 0 eV, corresponds to the zero loss peak where electrons have been collected without any loss of energy. More monochromatic beams provide sharper zero loss signals. The energy range between 0 eV and 40 eV is usually called low loss region. This involves excitations from valence to conduction band states which might have different physical origins: Cerenkov radiation, surface and bulk plasmon, intra-band transitions, excitons in semi-conducting materials. Due to the high localization of the electron probe, low loss EEL spectroscopy provides an optical characterization of the sample at a sub-wavelength spatial resolution. At higher energies, corresponding to the soft X-rays energy range, it occurs the core loss part of the spectrum, which corresponds to excitation of core electrons to the conduction band. The characteristic energy value of the core-levels for a given species, allows a precise elemental mapping of the sample. The analysis of near edge fine structures can provide complementary information on the chemistry of the sample or oxidation states. In aberration corrected STEM microscopes all these chemical information can be acquired at an atomic resolution.

3.2.2 Cathodoluminescence

When bombarding the surface of a material with an incident radiation or particle the emission of an electromagnetic radiation arises, beyond that produced by thermal black body radiation. This emission can be in the visible range (400-700 nm), ultraviolet (<400 nm) or infrared (IR; >700 nm). This general phenomenon is known as luminescence. The types of luminescence are generally distinguished by the type of incident radiation or particles and by the kinetics of the emission process.

Cathodoluminescence is an electromagnetic and optical phenomenon in which electrons colliding on a luminescent material such as phosphor, cause the emission of photons which may have wavelengths in the visible spectrum. The generation of light by an electron beam scanning the

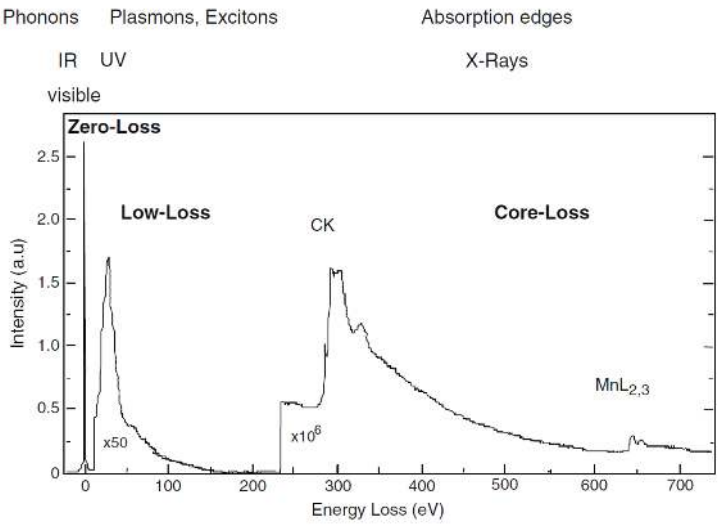

Figure 3.4: *Typical EEL spectrum, extracted from [88]. The ZLP dominates the spectrum at zero energy loss. At higher values of the energy loss in the low-loss region, resonances appear due to valence excitations. At much higher energies in the core-loss region, resonances from core level excitations emerge to a much lesser extent.*

phosphor-coated inner surface of the screen of a television that uses a cathode ray tube is a common example of this phenomena. Cathodoluminescence is basically the inverse of the photoelectric effect in which electron emission is induced by irradiation with photons. Cathodoluminescence occurs because the interaction of a high energy electron beam onto a semiconductor results in the promotion of electrons from the valence band into the conduction band, leaving behind a hole. When a hole and an electron recombine, it is possible to emit a photon [1]. The energy of the emitted photon, and the probability that a photon and not a phonon will be emitted, depends on the nature of the material irradiated, its purity, and its defect state. Considering the band structure, classical semiconductors, insulators, ceramics and glasses can be treated the same way. In geology, mineralogy, materials science and semiconductor engineering, a scanning electron microscope with specialized optical detectors may be used to ex-

[1] The mechanism of light emission for metal nano-particles, now widely used for metal nano-particle characterization, is quite different and not described here. The interested reader may refer to Ref. [89, 5]

amine internal structures of semiconductors, rocks, ceramics, glass, etc. in order to get information on the composition, growth and quality of the material. A review can be found in the book of Yacobi [90].

In such instruments, a focused beam of electrons interact on a sample and induces it to emit light that is collected by an optical system, such as a spherical mirror. From there, the light is transferred out of the microscope where it is separated into its component wavelengths by a monochromator and is then detected by a photomultiplier tube. By scanning the microscope's beam in an X-Y pattern and measuring the light emitted with the beam at each point, a map of the optical emission of the specimen can be obtained. The primary advantages of the electron microscope based technique, and in particular those using a STEM rather than a SEM is the ability to resolve features down to a few nanometers [91](Fig. 3.5) and the ability to measure an entire spectrum at each point (hyper-spectral imaging) if the photomultiplier tube is replaced with a CCD camera. Furthermore, the optical properties of an object can be correlated with structural properties observed with the electron microscope.

These advanced techniques are useful for examining low-dimensional semiconductor structures, such as quantum wells [92, 91], quantum dots [8, 93, 94] and defective semiconductors (see chapter 4 where the case of h-BN is discussed). Although direct bandgap semiconductors such as GaAs or GaN are more easily examined by these techniques, indirect semiconductors such as silicon also give weak cathodoluminescence, and can be examined as well. In particular, the luminescence of dislocated silicon is different from intrinsic silicon, and it can be used to map defects in integrated circuits. Recently, cathodoluminescence performed in electron microscopes has been employed to study surface plasmon resonance in metallic nano-particles [89]. Indeed, metallic nano-particles can absorb and emit visible light because of surface plasmon.

The cathodoluminescence system employed in this work is a home-made system design, integrated within a STEM microscope. Light emitted by the sample under the irradiation of the electron beam is collected by an aluminum parabolic mirror whose focal point is aligned with the focused

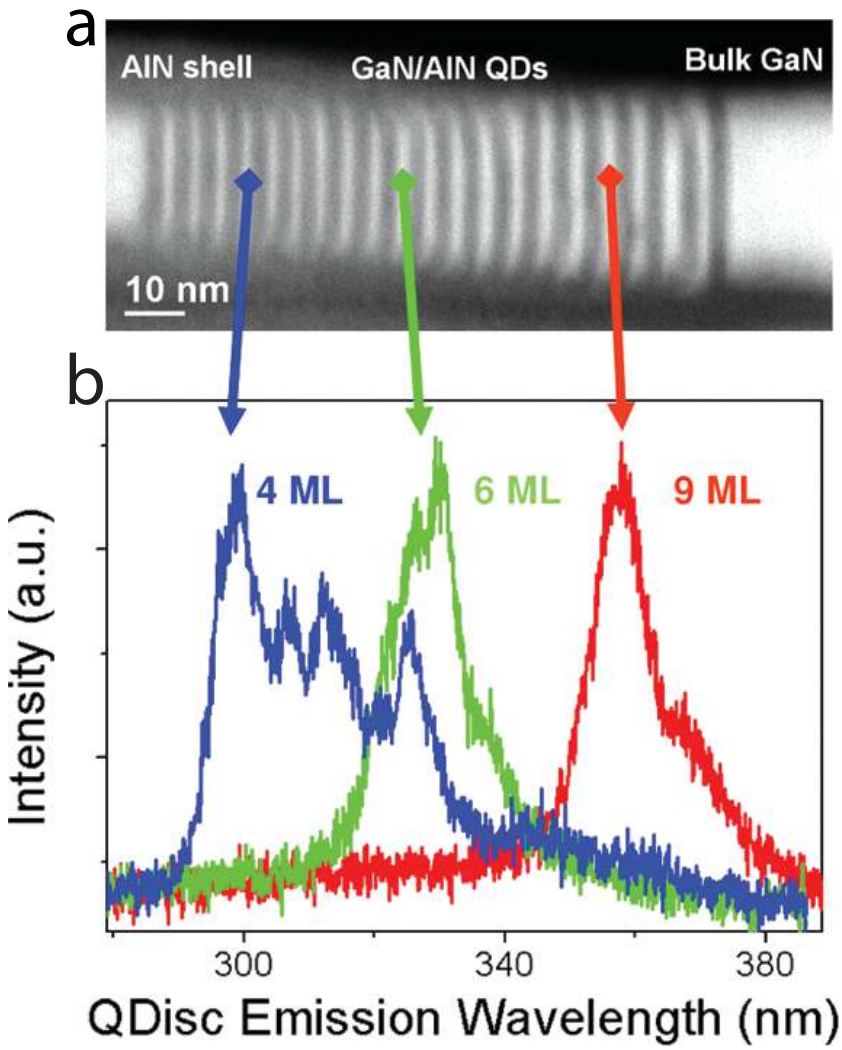

Figure 3.5: *Cathodoluminescence spectral imaging of a stack of individual quantum emitters made up of GaN in AlN quantum discs (QDs) in a scanning transmission electron microscope.* ***a*** *High-angle annular dark field (HAADF) of a typical nano-wire with embedded QDs. GaN appears brighter, AlN darker.* ***b*** *Spectra extracted at positions noted in* ***a*** *from spectrum images [91].*

electron beam. Light is guided from the parabolic mirror to the spectrometer by an optical fiber. The spectrometer is equipped with diffraction gratings and full cathodoluminescence spectra are collected on a CCD camera. The spatial resolution in this cathodoluminescence is driven mainly by three parameters. The first one is defined by the instrumentation used to perform the cathodoluminescence and it relates directly to the size of the electron beam spot used to excite the material. In a STEM microscope, such as the VG HB501, this is typically around 1 nm, although smaller electron probes are now available. The other two parameters defining the resolution are directly related to the nature of the sample studied. When electrons interact with matter in a STEM, an excitation is created in a given volume. A way to reduce this region and thus to increase the resolution is to decrease the thickness of the sample illuminated or to increase the acceleration voltage. These parameters have a low influence in the case of h-BN due to the relatively low thickness of the flakes. The last parameter is intrinsic to the nature of the sample and it is the charge carrier diffusion. It corresponds to the maximum distance which can separate a hole and an electron which recombine, which is around few tens of nanometers in h-BN. In the present work, I have used a STEM system rather than a SEM one. Besides the above mentioned gain in spatial resolution, working in a STEM decreases the electron matter interaction. As detailed in the review [95], this reduces heating and non-linear effects, that can be detrimental within SEM CL, see me. g. [94, 92].

Experimental set up The cathodoluminescence system is integrated in the VG STEM microscope described in section 3.1.2. It is a home-made system with patented technologies [96] helping at obtaining both a very high throughput and spectral resolution. As such, it has a competitive advantage over the only commercial STEM-CL system (Vulcan by GATAN), which poorly conserves both throughput and spectral resolution. The liquid nitrogen cooling stage is motivated by the exigence of optimizing radiative recombination. The cathodoluminescence signal is collected by an aluminum parabolic mirror whose focal point is aligned with the focused

electron beam. The radiation collected by the mirror is then reflected as a plane wave to a lens coupled to a bundle of optical fibers [96]. The light is guided to a SP2300A spectrometer (Princeton Instrument) equipped with a ProEM CCD camera (1600x200 pixels) (Roper scientific). The spectrometer is equipped with three diffraction gratings: a "near infra-red" grating blazed at 1.2 eV covering the 1.1-1.45 eV energy range, a "visible" grating blazed at 2.5 eV covering the 1.5-4.2 eV range and an "ultraviolet" grating blazed at 4.1 eV covering the 3-6 eV range. The latest grating has an efficiency of about 40% at 6 eV. The camera efficiency at 6 eV is about 20%. Despite this relatively low detection efficiency in the UV region, the signal detected from the h-BN excitonic emission was very intense indicating a very strong emission in the UV. Typical acquisition time used with this setup is about a few tens of milliseconds, thus very well resolved hyper-spectral image can be recorded (Fig. 3.6) with a 300x300 pixels, i.e $9 \cdot 10^4$ sequential spectra.

3.2.3 Filtered images and spectrum imaging

Combining the techniques presented before, EELS and cathodoluminescence, with a STEM allows to correlate structure and spectroscopy at a nanometer scale. Standard cathodoluminescence systems only allow to record either a full spectrum of CL or to obtain a filtered image at a specific energy window. The long term and continuous developments conducted within the Orsay group made hyper-spectral imaging to be nowadays a standard tool in EELS spectroscopy [97, 98] which now has been transposed to CL. Hyper-spectral images correspond to record a full CL and/or EELS spectrum at each pixel.

Figure 3.7 shows a schematic representation of a data cube or hyper-spectral image (representation of the image in 3D). The x and y axis correspond to the spatial coordinates and the z axis to the spectrum coordinate. The projection of the hypercube at a given energy (z coordinate) generates filtered images that can be sliced covering all the spectrum energies. A more complete spectral information can however be extracted using more

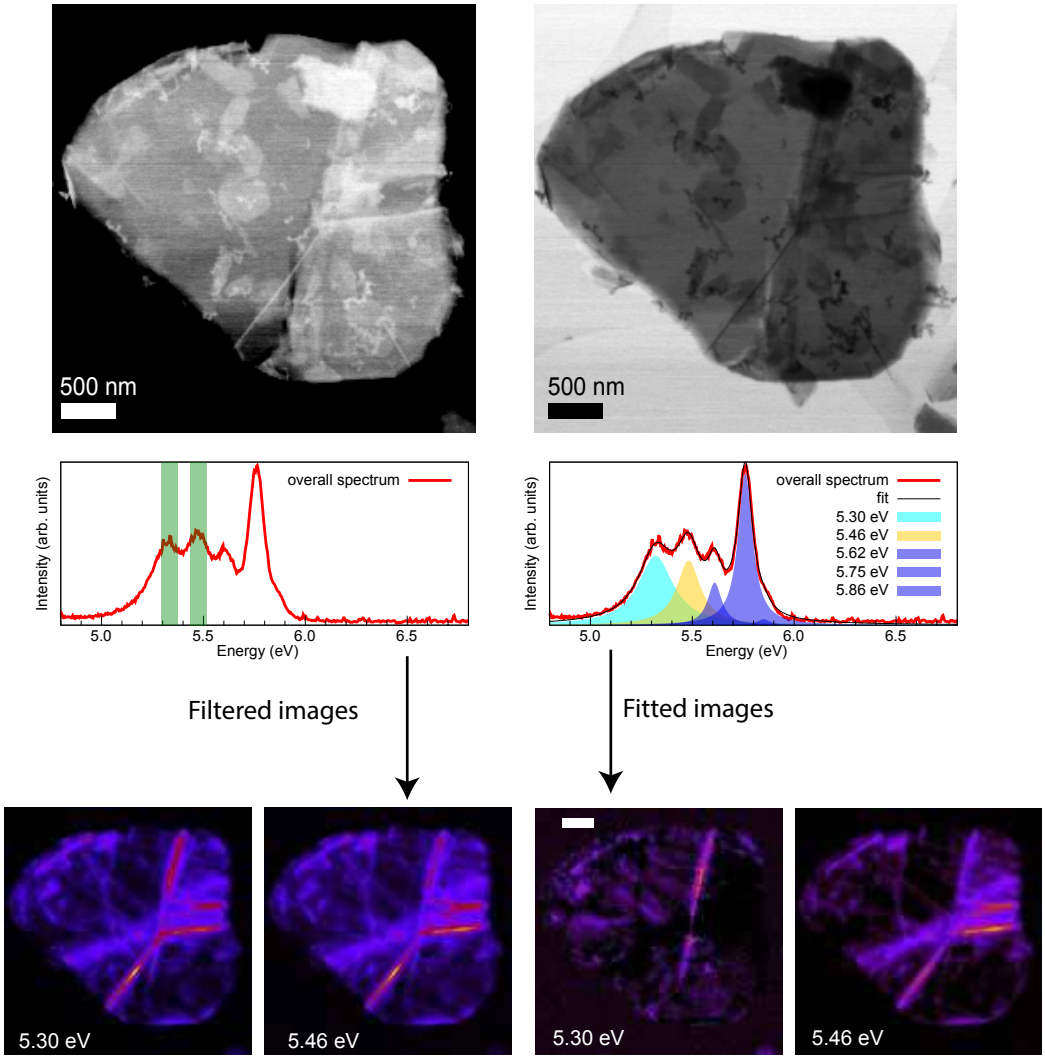

Figure 3.6: *Comparison between an energy filtered imaging technique and a multi fitting imaging technique.*

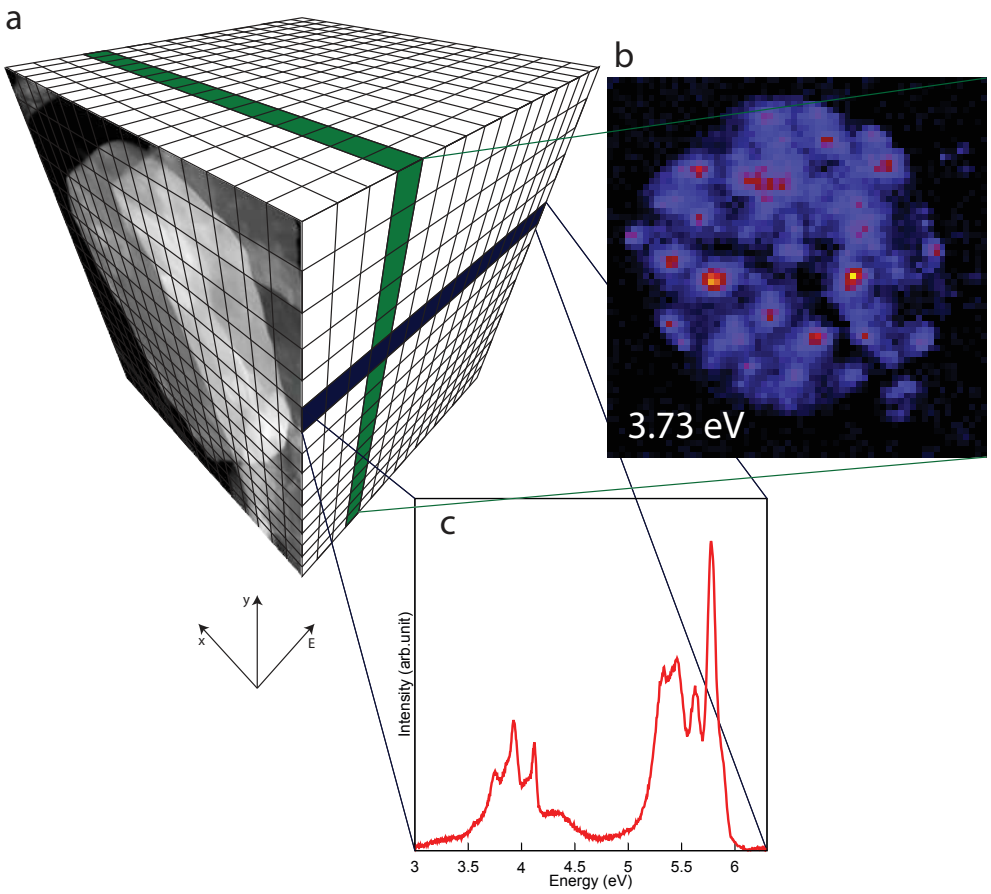

Figure 3.7: ***a*** *Schema of the hyper-spectral image.* ***b*** *Extracted filtered image at a specific wavelength.* ***c*** *Full cathodoluminescence spectrum extracted at one pixel.*

advanced data post processing methodologies. A common tool consists in multi-peak fitting routines using Gaussian functions that permit to extract pixel by pixel, the intensity, energy and FWHM of each spectral component. This technique allows for separate contributions from very close peaks. In the case of h-BN for instance, five sharp peaks appear in the 5.30-5.86 eV range. A brief comparison between filtered images and intensity maps extracted from a multi-fit routine is shown in (Fig. 3.6). It is possible to notice that in filtered images the 5.32 eV and 5.46 eV emissions are less localized compared to fitted maps. Indeed, filtered images at specific wavelength also integrate partially the surrounding components. It is thus impossible to separate each contribution and then both filtered image looks rather similar. On the contrary, in fitted maps, a clear difference appears since the two emission peaks are localized at different lines.

3.3 Quantum optics

A single photon emitter is an object able to emit only one photon at a time. Conceptually, it is a two-level system, which can emit a photon only upon excitation, with a typical delay between two photon emission equal to the lifetime of the emitter. Typical examples of single photon emitters in the optical range are quantum dots or point defects. Single photon sources are key factors for many applications in quantum computing. An assembly of such emitter sources coupled to linear optics elements and photo-detectors could be used to build up a quantum computer [99]. The easiest idea to produce an on demand photon emitting source consists in using an impulsional excitation on a two quantum levels system [100, 101].

3.3.1 Characterization

Single photon emitter sources are well known in quantum optics and usually characterized with an interferometer experiment. In this study, we will use an Handburry Brown and Twiss (HBT) intensity interferometer experiment (Fig. 3.9). A stream of photons is incident on a 50:50 beam

splitter, and is divided equally between the two output ports. The photons impinge on the detectors and the resulting output pulses are sent into an electronic counter/timer. The counter/timer records the time that elapses between the pulses from t_1 and t_2, while simultaneously counting the number of pulses at each input. The results of the experiment are typically presented as a histogram, as show in Figure 3.8. The histogram displays the number of events that are registered at each value of the time τ between the start and stop pulses. An HBT experiment gives a direct measure of the second-order correlation function $g^{(2)}(\tau)$ in the photon interpretation of light. The auto-correlation function is given by the formula:

$$g^2(\tau) = \frac{< I(t)I(t+\tau) >}{< I(t) >< I(t+\tau) >}$$

with $I(t)$ being the light intensity at time t

Coherent light For a coherent light, such as a perfect laser, the arrival of a photon on a detector is totally Poissonian. There is thus no correlation between the two photo-detectors of anHBT experiment. In such a case, $g^2(\tau) = 1$.

Single photon emitter sources The auto-correlation function corresponds to the correlation between two events of detection happening at t and $t + \tau$. In this case, the auto-correlation function can be written: $g(2)(\tau) = 1 - \exp(-(r + \sigma)\tau)$ with r the pumping rate and $\sigma^{(-1)}$ the lifetime. We obtain from this equation that at zero delay, $g^2(0) = 0$ and $g^2(0) < g^2(\tau)$. The Auto-correlation function will show a dip at a zero delay time for single photon emitter sources (Fig. 3.8)

3.3.2 HBT coupled to a STEM

Interferometry experiments (HBT) have been performed within our modified VG microscope equipped with our home made cathodoluminescence system. The interferometer experiment is connected to the cathodolumi-

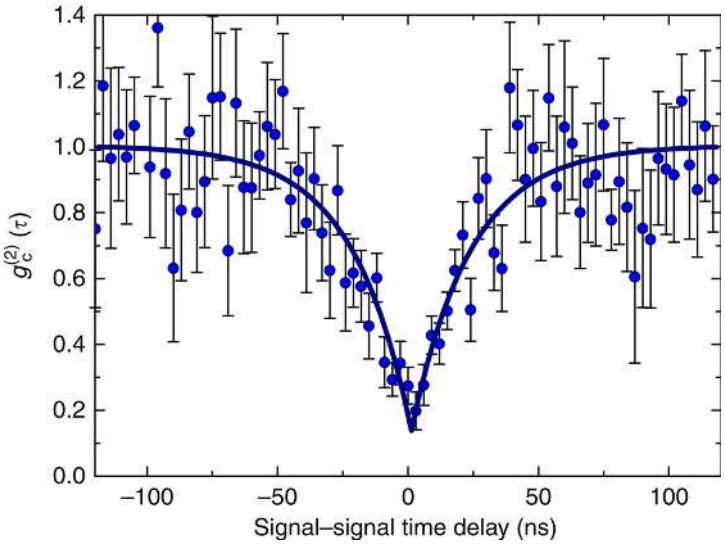

Figure 3.8: *Dip in the auto-correlation function characteristic of single photon emitter [102].*

nescence collection system by an optical fiber (Fig. 3.9). This allows to perform characterization of the quantum state of the emission at a nanometer scale in our microscope and thus to isolate and characterize specific defects in the samples. Photoluminescence HBT experiments are quite common now. However, the implementation of an HBT experiment in a cathodoluminescence is to the best of my knowledge uniquely implemented in our lab. Indeed, Tizei and coworkers have recently published the first results concerning the spatially resolved characterization of single photon emitters using this setup [103]. They were able to isolate color centers in diamond with an ultimate separation of 130 nm.

Experimental set up Emitted light is coupled to an HBT interferometer using an optical multi-mode fiber (100 μm diameter core). Incoming light has been filtered using an optical filter with transmitted wavelength between 300 nm and 340 nm corresponding to the range of interest in the experiments presented in chapter 5. The lenses are covered with a coating optimized in the UV range (290-370 nm) and the beam splitter works in the range of 250-400 nm. Single photons have been detected by two PMT

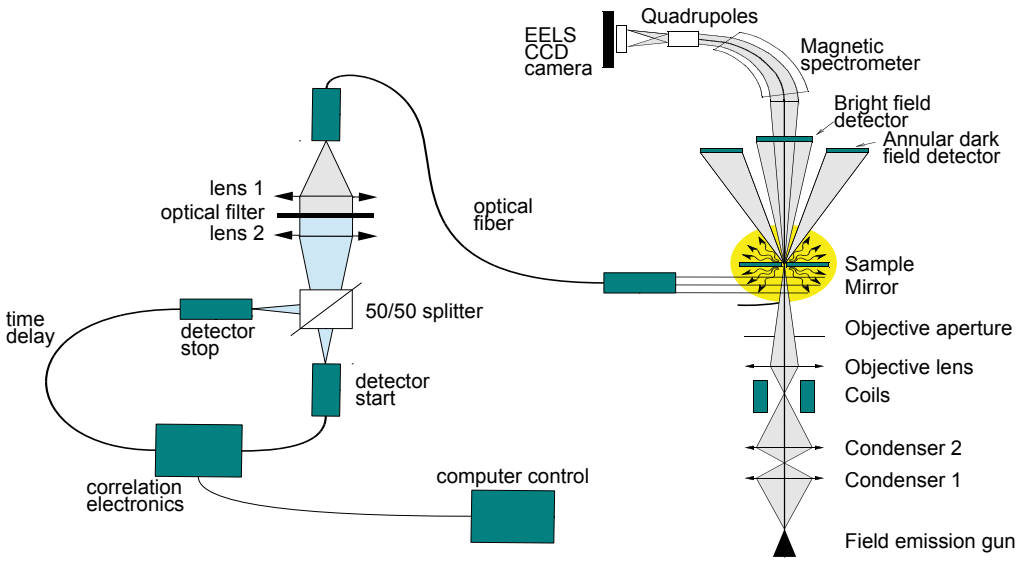

Figure 3.9: *Schema of the HBT interferometer experiment coupled to the home made CL system integrated within our STEM.*

modules. Time delay histograms (which are proportional to the second order correlation function) have been acquired using the Time Harp correlation electronics, from Picoquant. The typical room background noise varied from 200 to 500 count/s. Filtered images have been acquired by measuring the PMT counts signal at each pixels of the image. Typical acquisition time for each correlation curve was around few tens of seconds. Time delay histograms have been normalized to one for $\tau >> 0$, which is justified by the shape of the curve which show no bunching effect. Contrary to standard photoluminescence, no background subtraction has been performed as it cannot be estimated from the collected data.

CHAPTER 4

EXCITONS AND STACKING FAULTS IN h-BN

HEXAGONAL BORON NITRIDE is a very intense luminescent material in the UV, its emission spectra is dominated by a free excitonic emission at 5.75 eV. Additional features appear at lower energy, in the 5-6 eV energy region. The origin of these additional emission patterns is still controversial and it has been attributed to the presence of unidentified structural defects within the flakes [104, 105, 106]. This chapter will tackle the problem using our dedicated STEM cathodoluminescence system to visualize the spatial distribution of additional features at high energy. Afterward, defective structures where additional peaks are localized have been characterized performing high resolution electron microscopy focal series images and different stacking in h-BN has been identified. Quantum mechanical calculations have been performed on these different stacking and additional features have been correlated. Finally, findings on h-BN flakes have been transposed to multiwalled h-BN nanotubes and optical properties have been cleared out.

4.1 Previous observations: h-BN cathodoluminescence in a SEM

h-BN optical response has been investigated for more then fifty years using a wide range of techniques. However, the effective optical properties of h-BN remained controversial up to 2004. In this year Watanabe and

co-workers shown that perfect h-BN crystals have a rather simple emission spectrum dominated by an individual line at 5.75 eV [51]. The complexity of previously observed spectra had then to be associated with the presence of crystal defects. Intrinsic defects such as generic dislocations or grain boundaries have been proposed to be responsible of the origin of emission lines near the free exciton. This hypothesis arise from the observation that these additional peaks can be induced in a pristine perfect crystal by applying a limited mechanical strain (simply by pinching a perfect mono crystal in between the fingers) [104, 107]. Afterwards, the original emission spectrum of h-BN could be partially recovered through thermal annealing. This observation excludes the possibility that these additional emission lines might be associated with extrinsic defects such as crystal impurities. In order to correlate structure and defect related optical properties it is necessary to be able to acquire emission spectra at a high spatial resolution. As we discussed in chapter 3 photoluminescence is not adapted being ultimately limited by diffraction. Cathodoluminescence can reach the suitable spatial resolution when performed within an electron microscope.

The first sub-micrometer emission maps of h-BN were obtained by Jaffrennou and coworkers [108]. Cathodoluminescence (CL) images filtered at 210 nm and 220 nm recorded in a scanning electron microscope shown that the standard exciton is homogeneous in a h-BN crystallite whereas additional peaks present some spatial localization [108]. Complementary dark field electron microscopy images have evidenced that these peaks might occur in a crystallite at the frontier between regions having different crystal orientations [105]. An atomistic description of these defective regions was however not provided and the authors referred to the presence of generic grain boundaries.

More recently the same group confirmed their previous observations by using thinner BN flakes and a renewed CL system integrated in an SEM (Fig. 4.1) with a liquid helium cooled sample stage at 4 K. This new CL equipment uses a high detection system in the far UV region. Furthermore the lower temperature of the sample stage allows to identify the

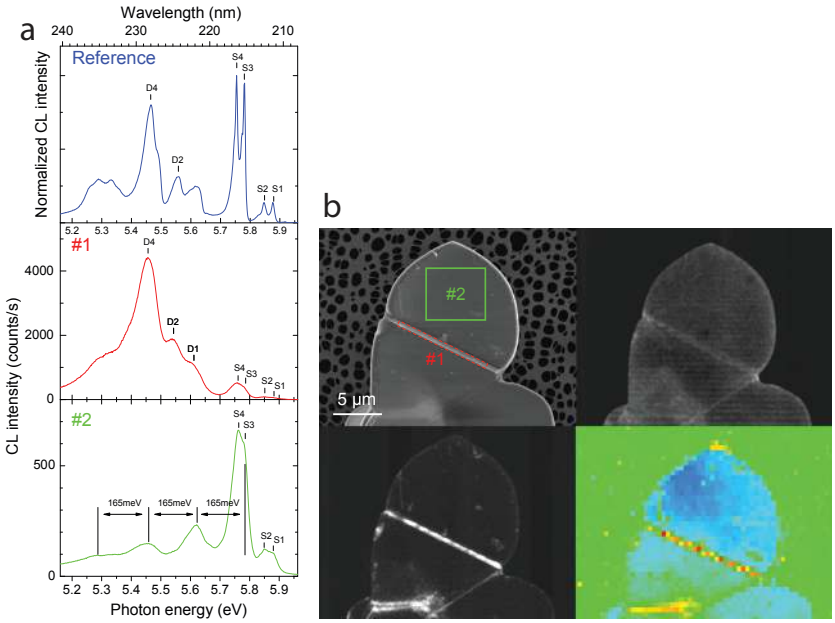

Figure 4.1: ***a*** *Full cathodoluminescence spectrum obtained on a thin h-BN flake . **b** Filtered images recorded on a the same flake (images extracted from[106]).*

splitting of all the luminescence peaks discussed in section 2.6.2. In this work the authors discuss a shift at higher energy of the 5.46 eV peak when the number of layers composing the sample is decreased (Fig. 4.2). The number of layers was determined by complementary AFM measurement. The blue shift observed was discussed as due to changes in the band gap or in the exciton binding energy.

In the same work it was discussed the eventual presence of phonon replicas for the free excitonic emission at 5.75 eV in the defect free region. The authors show a series of additional emission peaks with a constant energy separation of 165 meV between each replica (Fig. 4.1 green spectra). This observation is in contrast with previous photoluminescence results in perfect *h*-BN crystals where no phonon replicas were identified [51].

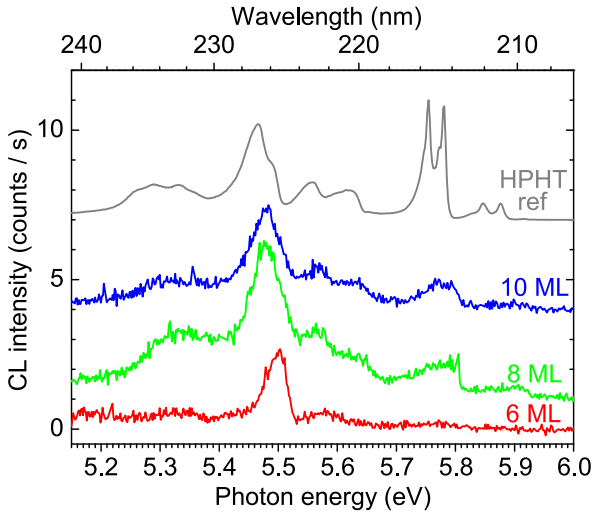

Figure 4.2: *Full cathodoluminescence spectrum obtained on a thin h-BN flakes of variable thickness, where shift of the 5.47 eV peak can be observed (spectra extracted from [106]).*

4.2 Sample preparation

The samples used in this study are thin h-BN flakes produced by chemical exfoliation in isopropanol following the process publish by Coleman *et al.* [68] and described in section 2.4.1.The process involves 10 hours sonication of a comercial h-BN powder in isopropanol, followed by a 2 hours centrifugation at 500 rpm. A thermal treatment consisting in annealing the sample under a reductive atmosphere composed of 5% of H_2 and 95% of N_2 are applied to all the flakes. This thermal treatment removes residual carbon and strongly decreases the middle band gap emission (3-4 eV) but it does not affect high energy emissions (5-6 eV).

4.3 Nanometric resolved CL on h-BN in a STEM

Using our STEM cathodoluminescence system, we have performed a nanometric resolved investigation of h-BN optical properties combining CL and electron imagery. In figure 4.3.a,b we present bright field and HAADF

images synchronously acquired with a hyper-spectral image. This hyper-spectral image presented is composed of 300x300 pixels, i.e $9 \cdot 10^4$ sequential spectra obtained while scanning the sample, total acquisition time was 10 minutes allowing a very small spatial drift of the sample. A series of five emission lines at 5.30, 5.46, 5.62, 5.75 and 5.86 eV is clearly visible in the average cathodoluminescence spectrum of the nano-particle (Fig. 4.3 .c). These energies correspond to previously reported values for h-BN crystals and multi-walled BN nanotubes [109, 105]. Photoluminescence experiments conducted at different temperatures show finer structures for temperatures below 50 K [109]. These additional features are smeared at higher temperature and thus are not visible through our experimental setup operating at about 150 K.

The three example spectra presented in Figure 4.3.c show the strong inhomogeneities in the peak relative intensities occurring at different probe positions. Thin samples present regions in which only the h-BN bulk exciton, usually called the free exciton, occurs. In order to extract the spectral weight of individual emission lines a multi-Lorentzian fitting routine has been applied to each spectrum of the spectrum image. Whereas peak energies were free parameters of the fitting procedure, no relevant energy shifts were detected across individual and between different flakes. Intensity maps derived from this analysis are shown in figure 4.3.d-h. Each map has been normalized independently on the basis of the most intense pixel. Indeed the detection efficiency is strongly energy dependent and the collection at higher energy is less effective. A calibration through all the optical path system is indeed not possible. It should be mentioned however that peaks at 5.62 eV and 5.86 eV are systematically significantly weaker than other emission lines and this behavior cannot be attributed solely to detection efficiency differences.

A detailed analysis of intensity maps demonstrates strong inhomogeneities occurring at lines crossing the flakes as seen in Figure 4.3. The free excitonic emission at 5.75 eV and the two emission peaks at 5.62 eV and 5.86 eV are distributed all across the particle. On the contrary, the two emission peaks at 5.30 eV and 5.46 eV are mostly localized at the lines. All

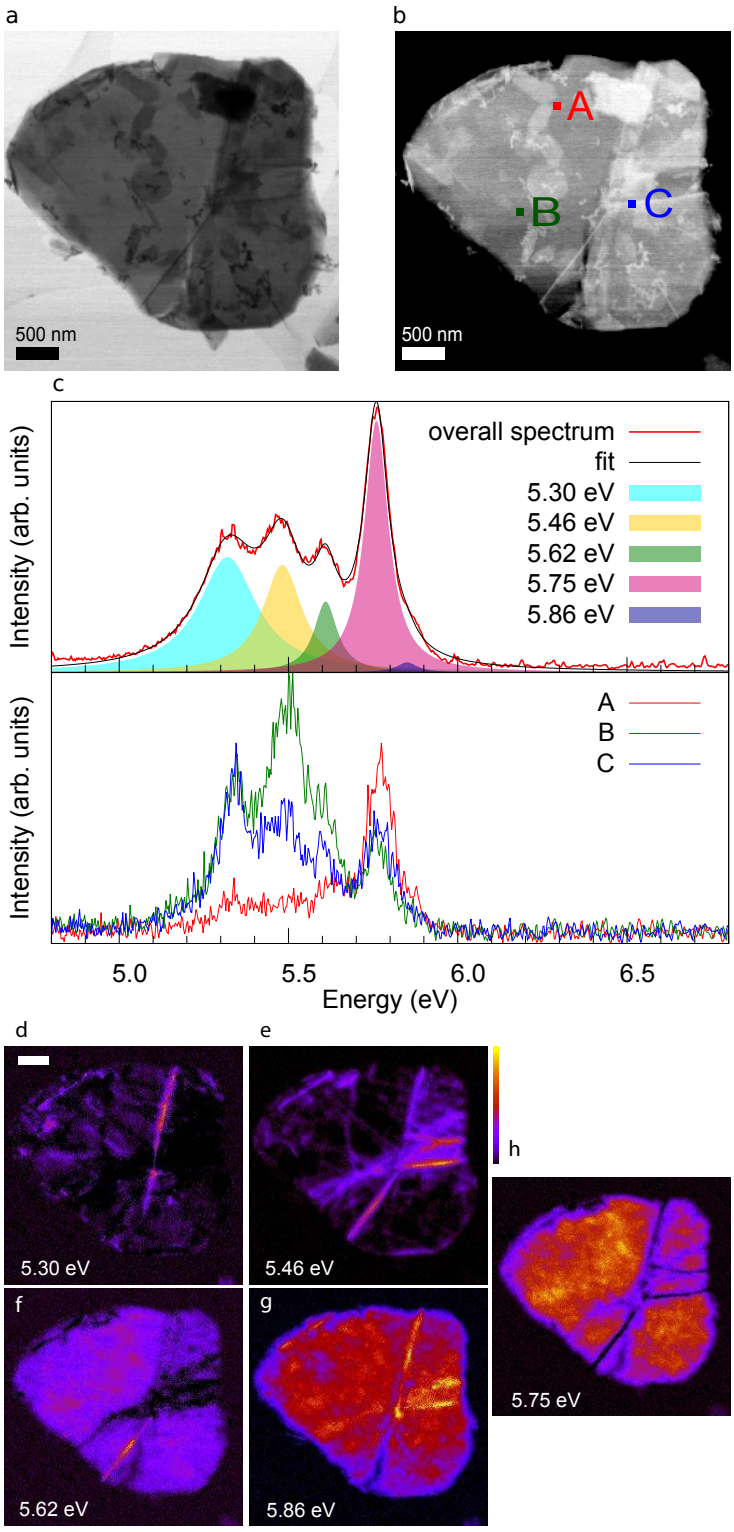

Figure 4.3: ***a*** *Bright field and* ***b*** *dark field images of an individual BN flake.* ***c*** *Overall emission spectrum of the flake and individual spectra taken at specific probe positions indicated in panel b.* ***d-h*** *Emission maps for each individual emission peak. Intensity is normalized independently within each individual map.*

emission maps are clearly not correlated one with another and thus all five emission features should be considered independent.

Figure 4.4 shows an additional map of a very thin region where two parallel bright lines are visible. Intensity maps are extracted applying the same multi fitting routine. In this example, several components of the spectra can be individually measured at separated regions of the flake. For instance, spectrum at position B shows solely the 5.46 eV emission peak while spectrum at position C shows solely the 5.75 eV emission peak. The map corresponding to the free excitonic emission at 5.75 eV is delocalized all over the flake as in the first example presented.

In thin homogeneous regions only the free excitonic emission at 5.75 EV is collected by our cathodoluminescence system. No phonon replicas were observed, contrary to what previously proposed by Pierret *et al.* [106] (see in Figure 4.1) and in good agreement with previous work performed on *h*-BN crystals [51]. The additional emission peak at 5.46 eV appears strongly localized along the line seen in HADF image in good agreement with the previous observation. Furthermore, the additional emission at 5.32 eV appears strongly localized on a line which is not visible in the HADF image and at a different orientation compared to the line corresponding to the 5.46 eV peak. This hyper-spectral image clearly shows that these 2 additional emissions are localized along lines, but at different orientations.

Additionally, no energy shift between different flakes of different thickness has been observed, contrary to the previous work proposed by Pierret *et al.* [106]. This is in good agreement with the previous photoluminescence work which always shows additional emission at the same energy [105].

The localization of the 5.32 eV and 5.46 eV emission peaks along lines has been observed systematically in all investigated flakes which present at least one line crossing the flake (about one hundred). These lines appear clearly in HAADF and bright field images and thus they are associated with local structural changes. Furthermore, they occur mostly in almost parallel pairs separated by a few up to hundred of nanometers (Fig.

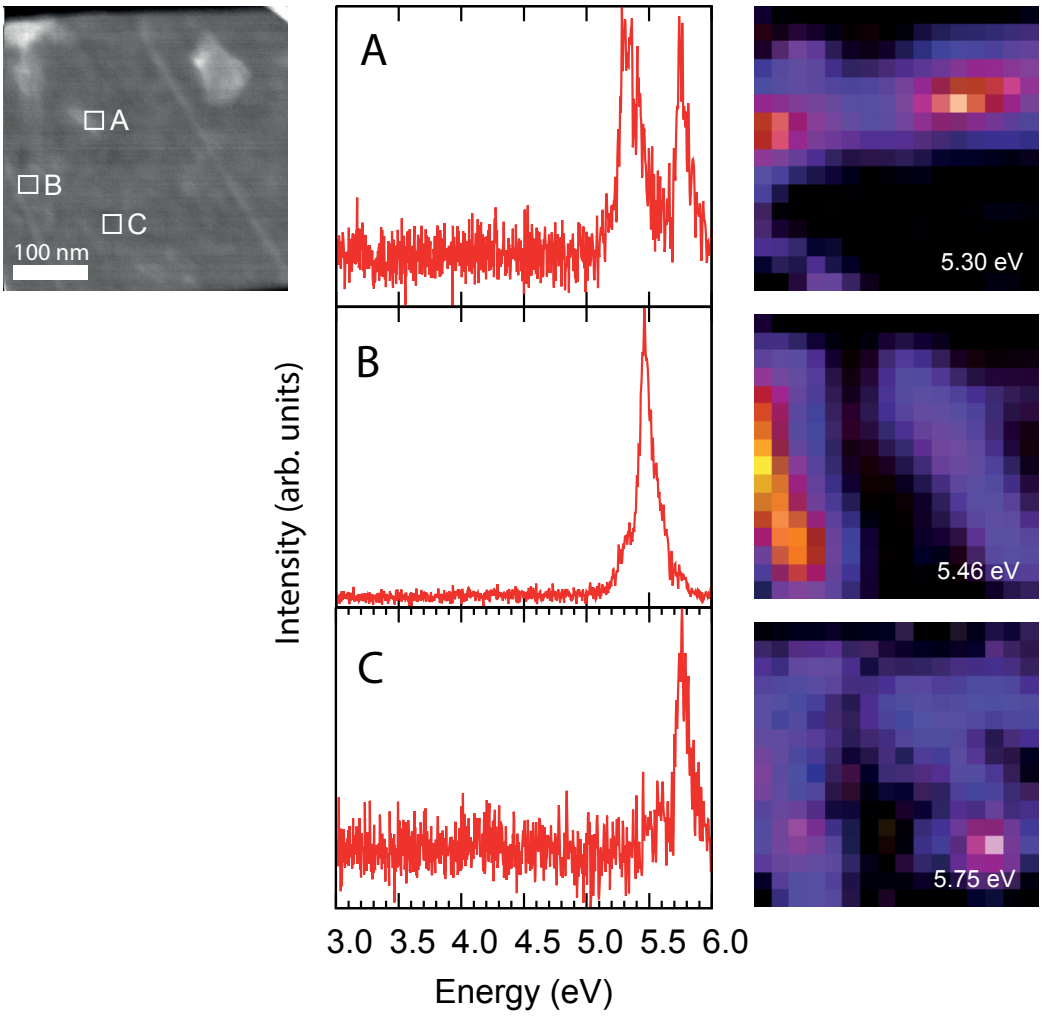

Figure 4.4: *HADF image displaying 2 parallel bright lines. Three examples spectrum taken at random probe position and intensity emission maps associated to emission peaks detected.*

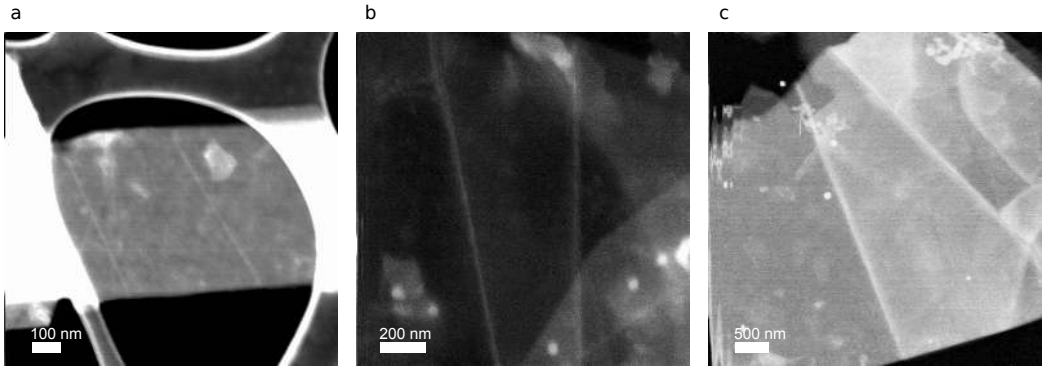

Figure 4.5: *HADF images showing the bright line where emission seems highly localized.*

4.5). Samples obtained by mechanical exfoliation from macroscopic monocrystals display only a few flakes with visible lines in HAADF images, and no additional features at 5.62 eV and 5.86 eV were detected in the recorded spectrum.

Lines crossing the flakes are then most probably induced by the chemical exfoliation process and in particular during sonication. For a better understanding on how specific emission peaks are associated with specific structural features, these lines have been characterized by bright field images in an aberration corrected STEM.

4.4 HREM on folds

High resolution electron microscopy images have been performed in a NION ULTRA STEM 200 operating at 60 kV to avoid beam irradiation damage. Bright lines in HAADF images are easily identifiable using this microscope. To study at the atomic scale the structure of the complex bright parallel lines, we focused only on lines separated by a few tens of nanometers. These structures are rather thick, and no well defined crystallographic orientation can be found. These conditions do not allow to have HAADF images at the atomic scale and thus, we performed high resolution scanning bright field images.

In Figure 4.6.g we present a HAADF image for a pair of parallel bright

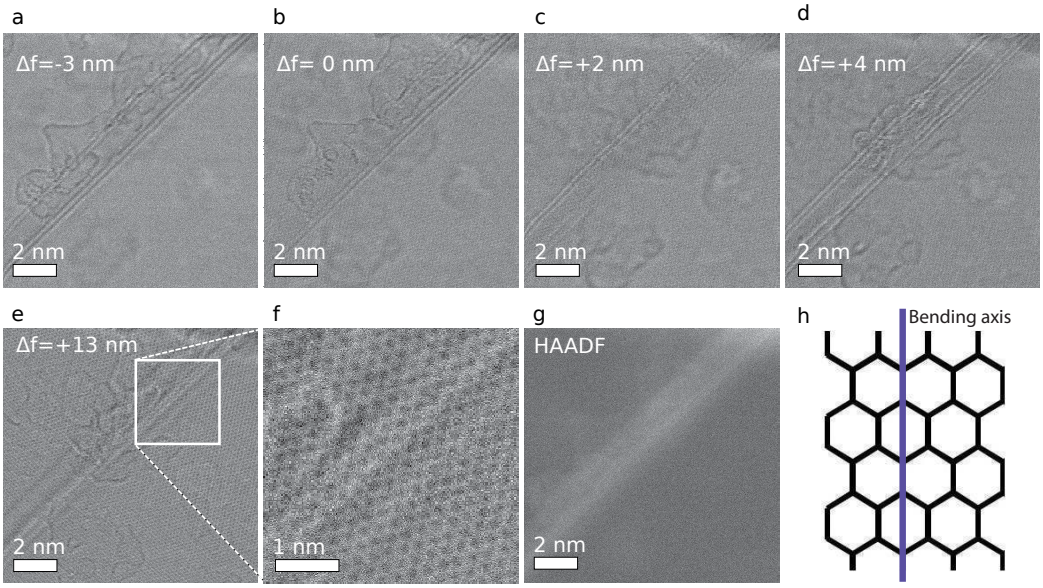

Figure 4.6: ***a-e.*** *Five micrograph of two couples of parallel fringes extracted from a 34-images focal series. The two pairs of fringes are focused at different focal depths.* ***f*** *Magnified image showing that the fringes are aligned along an arm-chair direction of the h-BN lattice.* ***g.*** *Dark field image of the region showing a local increase of the projected density at the fold.* ***h*** *Bending axis observed at the fold.*

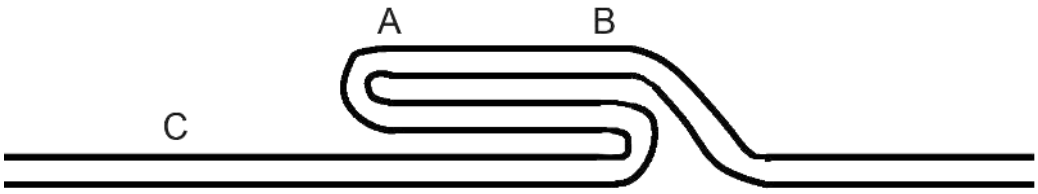

Figure 4.7: *Schematic representation of the defect characterized to be a double fold within the flakes.*

lines and the corresponding scanning transmission bright field focal series (Fig. 4.6.a-f). Each line is formed by two parallel fringes indicating layers parallel to the electron beam direction. The under-focused image is rather similar to the image of a double walled h-BN nanotube (Fig. 4.6.a), but unlike the case of a nanotube the focus for the two series of fringes occurs at two different de-focus values (Fig. 4.6.b,c). This corresponds to a situation where the two series of fringes lie at different depths. Finally, when both pairs of fringes are over focused the image of the underlying h-BN lattice is recovered (Fig. 4.6.e,f). The behavior described here can be explained by a model in which a layer stack can deform, forming two almost parallel folds (see Fig. 4.7).

This double folded structure has been proposed to occur in neutron irradiated graphite [110] and it has been recently imaged by electron and atomic force microscopy in CVD grown few-layers graphene [111, 112]. Local layer folding is also an extremely common defect, occurring in the early stage of hexagonal to cubic BN transformation through high pressure and temperature methods [113, 114].

These results suggest that emission peaks at energies of 5.30 eV and 5.46 eV are thus associated with folds as seen in Figure 4.8. This image shows CL intensity maps (Fig. 4.8.b-e) and BF focal series (Fig. 4.8.g-l) recorded on the same object and gives a clear correlation between these bright lines where additional luminescence peaks are localized and the defective structure corresponding to folds. Figure 4.8.g-l shows the same defocus described for fewer layers structures and thus the same kind of defect is expected.

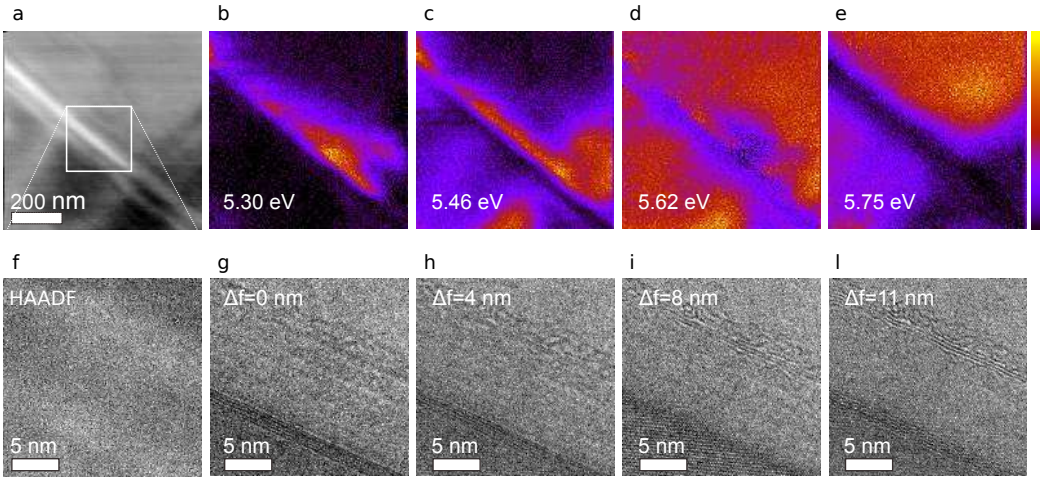

Figure 4.8: ***a.*** *Low magnification HAADF image of a line in a h-BN flake and* ***b-e*** *cathodoluminescence maps of the region corresponding to different excitons.* ***f.*** *Higher magnification HAADF image of the same zone and four bright field micrograph extracted from a 40 images focal series.*

It is also possible to notice that in intensity map corresponding to the additional peak at 5.46 eV (Fig. 4.8.c), emission appears asymmetric along the line. This asymmetric localization of the emission can be explained by the shape of the defect (Fig. 4.7) combined to the charge carrier diffusion effect. Considering the folded part labeled A in Figure 4.7 , when the electron probe excitation is in position B, due to charge carrier diffusion it is possible to collect emission from the folded structure A. On the contrary, when the electron probe excitation is in position C, it is clearly visible that the charge career diffusion effect cannot excite the folded structure A due to a longer distance. This easily explains the asymmetric character of the emission observed at very high magnification along the fold for the additional emission occurring along the line.

4.4.1 Model

According to our HREM characterization, and in good agreement with the literature [115, 116, 117], we propose a 3D schematic model of the fold in *h*-BN flakes (Fig. 4.9).

The different curvature of the layers at the fold induces, as for any

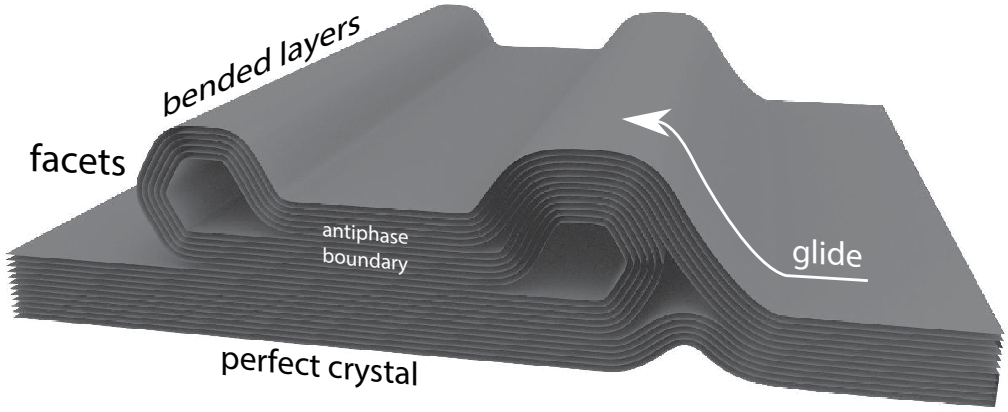

Figure 4.9: *Schematic representation of the faceted fold characterized by HREM BF focal series.*

multi layered structure, a relative glide of the layers (Fig. 4.10) and thus a loss of the original AA′ stacking sequence of the perfect h-BN crystal (Fig. 4.11). The local atomic structure of the folds is thus analogous to the structure of multi walled nanotubes where in principle no defined stacking sequence exists. However, in multiwalled BN nanotubes the competition between bending and inter-plane energies tends to localize the curvature and to promote polygonal tube sections with facets of well defined stacking, not necessarily AA′ [118, 119]. The local atomic structure at the folds should thus correspond to stacking sequences that can be generated from the original AA′ structure by a glide of the layers. Two metastable configurations can then be obtained: AB_1, where, following an analogous nomenclature as for graphite nitrogen,boron atoms lie at α and β sites respectively, and AB_2, where atoms positions are inverted (Fig. 4.11) [120, 121, 122]. The two metastable configurations AB_1 and AB_2 can be obtained from the AA′ structure by translating one of the basal planes by a vector $t \cdot (1/3, 2/3, 0)$ where t assumes the value 1 and 2 respectively (Fig. 4.10).

If the fold follows an armchair direction, as it is seen most often in scanning transmission bright field images (Fig. 4.6.f,g), anti-phase domains appear in the region between the folds. Zig-zag directions of the

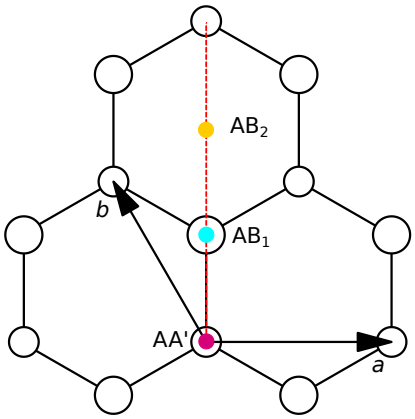

Figure 4.10: *Schematic representation of the transformation of AA′ h-BN in the AB_1, AB_2 and intermediate stacking configurations obtained by gliding one basal plane by a vector* $t \cdot (1/3, 2/3, 0)$.

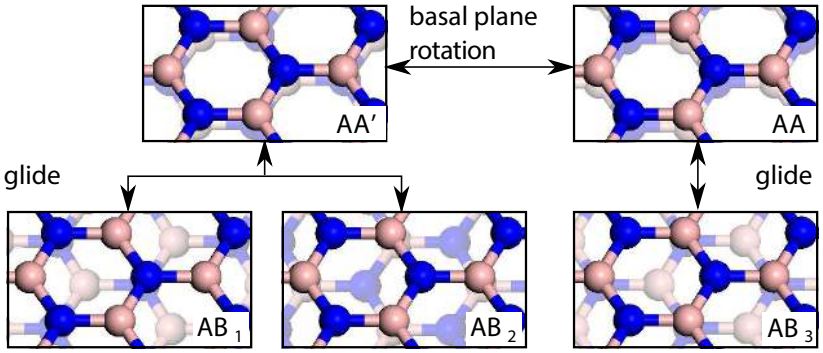

Figure 4.11: *Different stacking generated at the fold by glide and basal plane rotation.*

fold are less energetically stable, thus they are harder to be characterized. The stacking of planes at anti-phase domain boundary corresponds to a metastable AA order or, by applying an additional translation, an AB_3 order (Fig. 4.11). Besides the specific fold case, anti-phase domains are, as for graphite, a common defect in h-BN and indeed AA stacking orders have been recently identified in few layer h-BN crystals [123].

Structure	Space group	a (Å)	c (Å)	Total energy (meV)
AA′	P63/mmc	2.485	6.49	0
AB_1	P63/mmc	2.484	6.487	18
AB_2	P63/mmc	2.484	7.048	3.8
AB_3	P3m1	2.485	6.423	0.4
AA	P6m2	2.485	6.912	18

Table 4.1: *Space group, lattice parameters and DFT derived formation energy in respect to the AAóf the five different stackings (extracted from [120, 122]).*

4.5 *h*-BN stacking configurations

The energy stability of the five different high symmetry stackings described before have been already discussed theoretically in the literature [120, 121, 122, 123]. All stacking are not necessary energetically stable (DFT derived formation energy in respect to the AAśtructure are displayed in Table. 4.1) but constrains at folds or additional structural defects can stabilize these structures (see for instance Ref. [123]).

It has also already been discussed in the literature ground states electronic structure of the different stacking configurations and changes in the nature (direct or indirect) and the value of the band gap. However up to now the optical response of these systems necessary to completely correlate each stacking with specific emission energies has not yet been explored. In the framework of this thesis work, this theoretical investigation of the optical properties of the five stackings has been conducted using many body perturbation theory techniques. This work was conducted mainly by Michele Amato, who was a joint post doc between our laboratory and the Theoretical Spectroscopy group in the Laboratoire des Solides Irradiés (LSI, Ecole Polytechnique) at the same time of this thesis work. Theory and experiments have thus progressed side by side with continuous mutual interaction. This fruitful collaboration has provided a coherent and complete view of the relation between structure and optical properties of *h*-BN. In this section, that should be considered as a strong complement to this thesis work, it will be provided an overview of the the-

oretical spectroscopy techniques employed and the main result obtained.

4.5.1 Electronic properties of the different stacking

Quantum mechanical calculations of electronic and optical properties for the five stacking configurations of bulk h-BN were performed following a well established computational procedure. Ground state electronic structures were derived using plane waves pseudo-potential density functional theory as implemented in the ABINIT package within the local density approximation (LDA) . A Monkhorst-pack grid of $10\times10\times4$ k-point was used to sample the Brillouin zone of the system. An energy cutoff of 32 Ha was demonstrated to be enough for the convergence of the total energy. Following the ground state calculations, self energy corrections to the Kohn-Sham eigenvalues for high symmetry points of the Brillouin zone were obtained using many body perturbation theory (MBPT) adopting a non self-consistent GW approach. The $6 \times 6 \times 2$ k-grid for GW calculations was not shifted meaning that the Gamma point was included. In a first step, optical spectra were evaluated in the random phase approximation (RPA). Dielectric functions were derived using a $15 \times 15 \times 7$ shifted k-grid and 30 energy bands. Crystal local field effects were included (with 50 G vectors) and a scissor operator was applied to take into account GW self energy corrections. Since for all structures the dispersion of the GW correction was lower than 0.5 eV, the scissor operator was chosen as the GW correction at Gamma. In a second step, we performed optical spectra calculations by using the Bethe-Salpeter equation, which permits to include electron-hole interaction by mixing all the electronic transitions in the resolution of a two particle equation. A $15 \times 15 \times 7$ shifted k-grid was used, with 50 G-vectors and a broadening of 0. 025 eV.

Band structures of different h-BN polytypes (not shown here) are sensitive to different stacking order. For different configurations, the bands do not change their dispersion for directions in the a^* b^* plane. However, for directions parallel to the c^* axis (KH and ML) , the last two occupied and first two unoccupied bands are either degenerated or split depending on

Confi-guration	Direct gap LDA	Direct gap GW	RPA optical gap	First optical active exciton transition energy	Exciton binding energy
AB_1	3.48	5.20	5.20	4.89	0.31
AB_2	3.70	5.45	5.45	4.98	0.47
AA	2.95	4.67	5.70	5.21	0.49
AA′	4.52	6.19	6.19	5.42	0.77
AB_3	4.35	6.09	6.09	5.43	0.66

Table 4.2: *DFT-LDA and GW direct gap, RPA optical gap, BSE first optical active exciton energy and exciton binding energy calculated for different h-BN stacking configurations. All energies are expressed in eV.*

stacking order. This leads to changes in the direct band gap observed both at the DFT and GW level (Table 4.2). This behavior has also a fundamental role in defining the optical properties of different stacking configurations. Indeed, in agreement with the work of Arnaud *et al.* on AA′ *h*-BN [73], we find for all configurations that directions in the reciprocal space parallel to the c^* axis give rise to the first absorption peak of ε_2 both at RPA and BSE levels. This is due to the low dispersion of the last occupied and the last unoccupied band along the HK reciprocal space direction.

Quasi-particle band gaps and exciton binding energies are finally strongly dependent from the stacking configurations (Table. 4.2). Both effects contribute to the determination of the energy of the first optical active exciton. A further and deeper analysis will be the object of a forthcoming study. In order to investigate the effect on the optical properties of a continuum variation between high symmetry configurations, absorption spectra have been computed following a GW+BSE scheme for three additional configurations with t=0.25, 0.5 and 0.75. In Figure 4.13 it is shown that a different absorption spectrum is associated with each configuration. The experimental observation of only five excitonic emission peaks is thus a clear indication for a limited number of high symmetry stacking configurations present in the crystals.

Bands dispersion changes depending on stacking order for directions

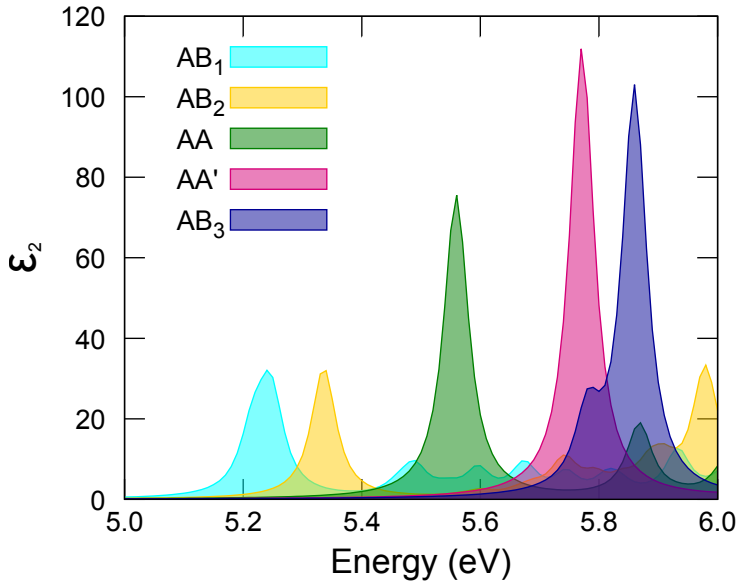

Figure 4.12: *Theoretical spectrum simulated for each different stacking sequences.*

parallel to the c^* whereas it remains invariant for directions in the a^* b^* plane. In agreement with the work of Arnaud *et al.* on AA′ h-BN [73], we find for all configurations that directions parallel to the c^* axis give rise to the first absorption peak of ε_2 both at RPA and BSE levels. Quasi- particle band gaps and exciton binding energies are finally strongly dependent on the stacking order and determine the energies of optically active excitons.

4.5.2 Correlation between structure and additional emission

All absorption spectra presented in Figure 4.12 show strong excitons with well separated energies in the range between 5.2 to 5.9 eV depending on the stacking configuration. Taking as a reference the standard AA′ exciton at 5.75 eV, three additional excitons, associated with the AB_1, AB_2 and AA configurations, occur at lower energies whereas that of the AB_3 configuration is found at a higher one. Energy range and peak distribution coincide with experimental results. Thus, theoretical simulations enable us to associate each of the five measured emission peaks with the five high sym-

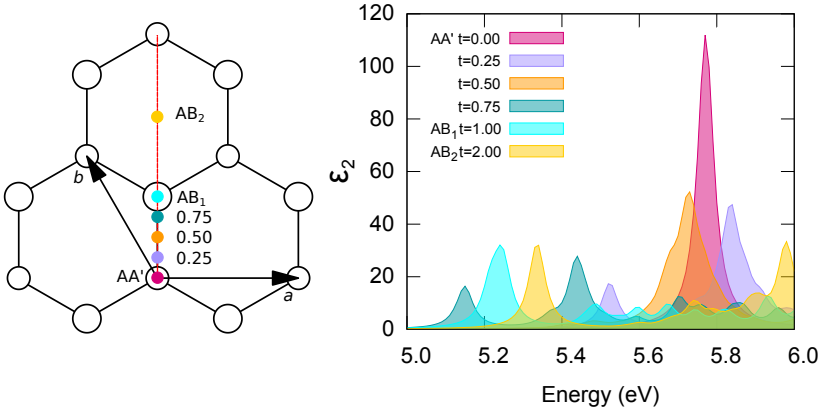

Figure 4.13: ***Left*** *Schematic representation of the transformation of AA′ h-BN in the AB_1, AB_2 and intermediate stacking configurations obtained by gliding one basal plane by a vector $t \cdot (1/3, 2/3, 0)$.* ***Right*** *Imaginary part of the dielectric function (optical absorption spectrum) for different h-BN stacking derived in the framework of GW+BSE calculations.*

metry configurations analyzed. In particular emissions at 5.30 and 5.46 eV, strongly localized at folds, can be attributed to AB_1 and AB_2 stacking sequences respectively. These models are compatible with the fold structure where the layer glides occur. Emissions at 5.62 and 5.86 eV can be associated with the AA and AB_3 stacking respectively. Since these stacking appear at anti-phase boundaries, these excitons occur in large regions of the flake and their signal is weak due to the small number of atomic planes involved. We underline that each intermediate stacking gives rise to different exciton energies. The experimental evidence for only five discrete emission lines is thus a clear indication of a finite number of stacking configurations and it confirms the hypothesis of faceted folds.

This model presented here with the five different stacking at the double folded structure in h-BN differs from the grain boundary model proposed by Pierret *et al.* [106]. However, our interpretation is based on a more complex investigation that combined a better resolved CL system, high resolution images and complementary simulation.

Using a complementary experimental and theoretical approach we have provided a microscopic explanation for the complex emission spectrum of h-BN relating local changes in the layer stacking order to the appearance

of additional excitons. Furthermore, we have shown how these defects and the associated excitonic emissions can be strongly localized at folds crossing the flakes. Finally, our theoretical analysis reveals that, whereas additional emission lines in h-BN can still be interpreted as excitons bound to defects, they can be better described as bulk excitons of different polytype. Recently, h-BN polytype has been discussed from a morphological and energetic point of view but little attention was paid to their optical and electronic properties [120, 121, 122, 123]. This study emphasizes the role of stacking changes in defining the optical properties of h-BN. The importance of stacking faults is thus directly related to the interest in h-BN as one of the most promising materials for high performance far ultraviolet emitters [23]. The low activation energy of stacking faults in layered materials justifies their native abundance, but also the facility to induce them by limited mechanical deformations. This study suggests that deliberately introducing stacking faults in a perfect h-BN crystal can be used as a way to tune the emission spectrum in the far UV region. From a complementary point of view, the analysis of the excitonic response can be employed as a powerful tool to precisely map structural deformations in h-BN crystallites and in the new nano-electric systems constituted by h-BN/graphene hetero-structures.

4.6 Excitons in multiwalled Boron Nitride Nanotubes

It has been shown in the previous section how folding planes induce changes in the stacking of h-BN and lead to additional emission. There are some h-BN nano-forms naturally folded, that is the case of BN nanotubes. Considering that stacking changes are responsible for additional emission of h-BN crystals, one could assume that they all play a role in the optical properties of BN nanotubes. This section is devoted to the exploration of such a hypothesis through the study of multiwalled BN nanotubes with diameters varying from a few tens to a few hundreds of nanometers.

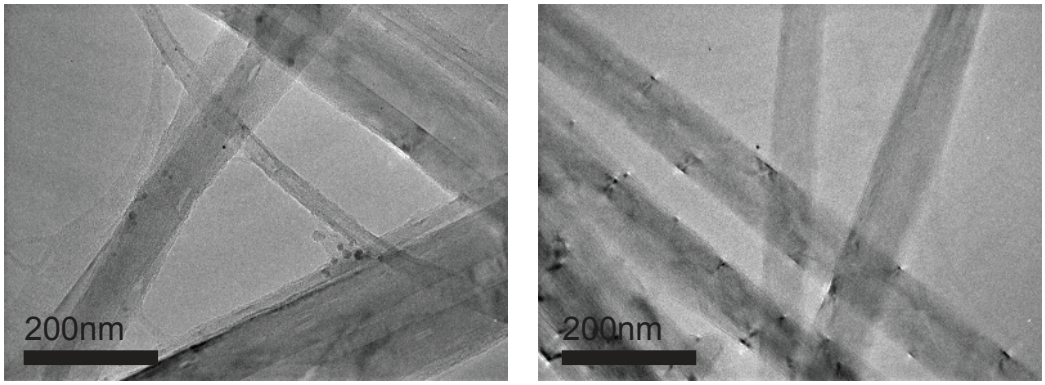

Figure 4.14: *TEM images of multiwalled h-BN nanotubes, where parallel fringes can be seen as well as black spots along the tubes.*

4.7 Structural properties

The BN nanotubes studied were produced using Boron Oxide Chemical Vapor Deposition (BOCVD) by Golberg and co-workers [58]. Some general information about such type of nanotubes has been already given in the first chapter. Here, an overview of the actual knowledge about their structure is presented. Figure 4.14 shows a typical multiwalled BN nanotube image acquired by TEM, displaying a series of parallel fringes corresponding to the successive layers constituting the walls of the tubes together with some equidistant black spots along both sides of the tubes. The origin of these black spots is still unclear. In 2005, Kim *et al.* [124] showed from an EDX study that such BN nanotubes contain boron, nitrogen but also magnesium and oxygen which are used as precursor elements during the synthesis process. The authors claimed for a correlation between the precursors localization within the walls and the presence of these black spots in TEM images. Their results have been contradicted by Golberg *et al.* [125] in 2007 as EELS measurements only showed the presence of boron and nitrogen, even at the black spot locations. A more accurate structural study on BOCVD BN nanotubes was performed in 2005 by Celik-Aktas [126], which clearly showed that the black spots originated from a variation in the layers orientation, which induced diffraction contrast (Fig. 4.15). Indeed, based on the analysis of Bright Field TEM im-

ages and Dark Field images obtained from the (002) reflexion the authors could conclude that these black spots occur when the basal planes (associated with (002) reflection) are in Bragg conditions i.e. when the layers are tangent to the incident beam. Importantly, the observed huge diffraction contrast indicates that Bragg conditions are perfectly fulfilled, which implies that the nanotube walls are not curved contrary to usual nanotubes. The authors confirmed this hypothesis, showing high resolution images of this back spots in which walls are very well imaged contrary to others areas. This specific orientation has also been characterized using EEL spectroscopy looking at fine structures of boron and nitrogen K edges. All these observations give a strong indication that in certain areas the nanotubes facets. When tilting the nanotubes along their axis, the black spot moves and keep a constant separation distance indicating that facets are rotating around the nanotube axis to form an helix. The Authors of $cite-CAnt05 concluded that these multiwalled BN nanotubes are formed by a double helix, the first one faceted, and a second one circular and less ordered.

Tomography Very recently, Pierret *et al.* performed tomography on BO-CVD nanotubes and provided a convincing confirmation of the faceting of the tubes [127] with a fine characterization of the different facets. The tomography experiment of Figure 4.16 gives a clear evidence of the polygonal character of the section a nanotube. It was shown that the typical numbers of facets range from 6 to 9, with predilection for 7 or 8 facets. Furthermore, images taken at different positions along a nanotube also confirmed that facets turn around the tube axis to form a helix as predicted in 2005 by Celik-Aktas [126]. To finish the authors concluded on the hypothesis of a non-constant helix step along the tube. However a clear characterization of the grain boundaries could not be provided due to insufficient spatial resolution.

Characterization of the number of facets by HRTEM In this section, we suggest a fast and easy technique to determine the number of facets

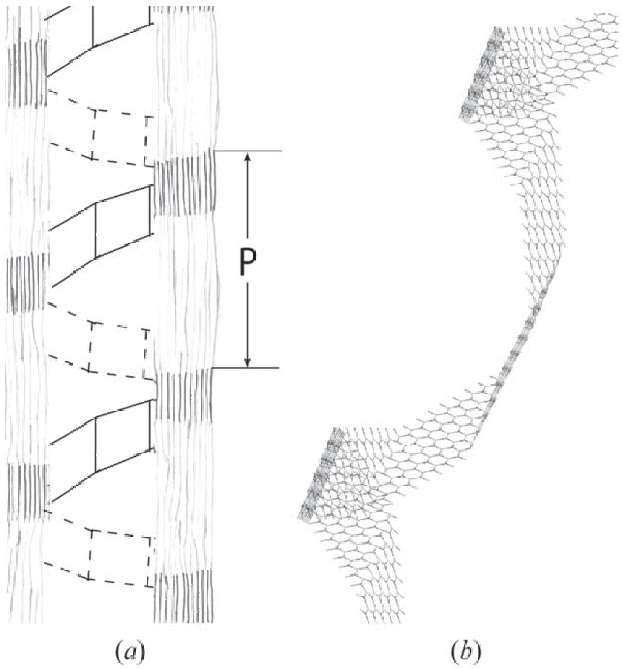

Figure 4.15: *Schematic model of multiwalled hBN nanotubes proposed by Celik-Aktas [126]. This model shows a helix model for faceted nanotubes.*

in BOCVD nanotubes. This method relies on HRTEM images obtained with the TOPCON microscope and on the structural specificity of these nanotubes. As a matter of fact, BOCVD nanotubes very commonly show extended defective structures. These defects appear inside the nanotube, along the wall structure. In very localized areas, some breaks in the walls of the nanotubes can be clearly seen. This leads to a bonding of the broken walls, forming bonded edges as displayed in Figure 4.17.a.b and as already observed at h-BN bi-layers edges [40]. In our observations, this bonded edge have been seen for different numbers of walls from two to six. This bonded wall structure coupled to the rotation of the facets along the nanotube axis leads to the formation of polygonal pattern when imaged by TEM (Fig. 4.17.c). This polygonal pattern exhibits a number of facets equivalent to the number of facets of the nanotubes when seen in projection perpendicularly to the tube axis. The imaging of such a pattern can therefore be used as a fast and easy technique to determine the number of facets of a multiwalled BN nanotubes in a conventional TEM. In the

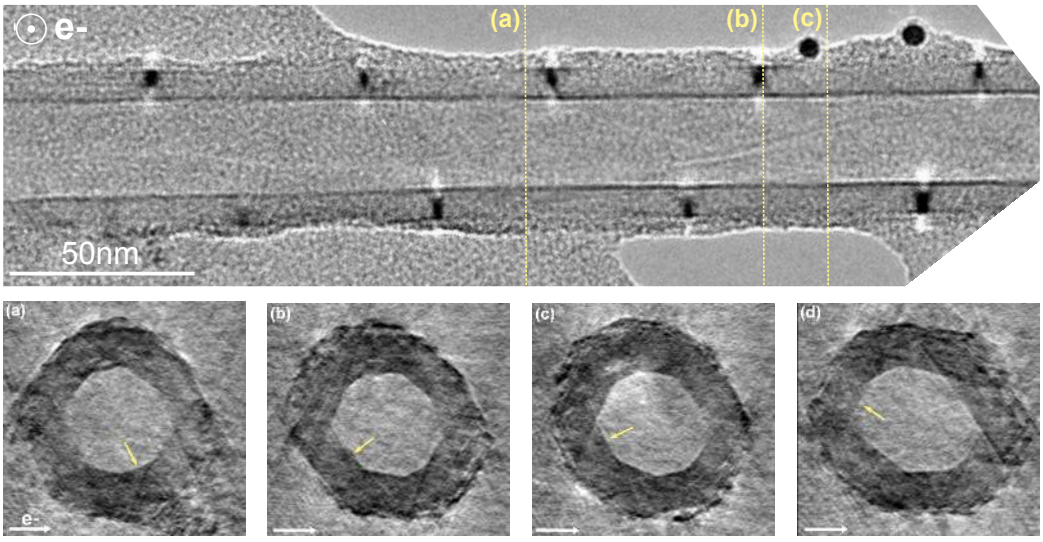

Figure 4.16: *TEM tomography experiment performed at IPCMS (Strasbourg) on a multiwalled BN nanotube showing polygonal section at different positions along the tube [127].*

case presented in Figure 4.17, a number of six facets are identified.

4.7.1 BF HRSTEM

High resolution scanning transmission electron microscopy (HRSTEM) in the bright field mode has been used to investigate the structure of BN nanotubes at facets boundaries. These experiments have been carried out in an aberration corrected NION USTEM 200 microscope operating at 60 kV in order to minimize radiation damages. Figure 4.18 displays a STEM BF image in the strongly diffracting areas (dark spots) of a nanotube. A closer look at the wall from such a region shows some fringes which are not parallel to the tube axis. These reflect the presence of a grain boundary between two facets scrolling around the nanotube axis to form a helix. Using such a BF image allows to measure the angle between the nanotube axis and the grain boundary (1.54 ° in this case). Now, using simple trigonometry, it is possible to calculate the helix step. Considering a measured nanotube diameter of 60 nm, the helix step (separation distance between 2 black spots formed by the same grain boundary) is about 4 μm.

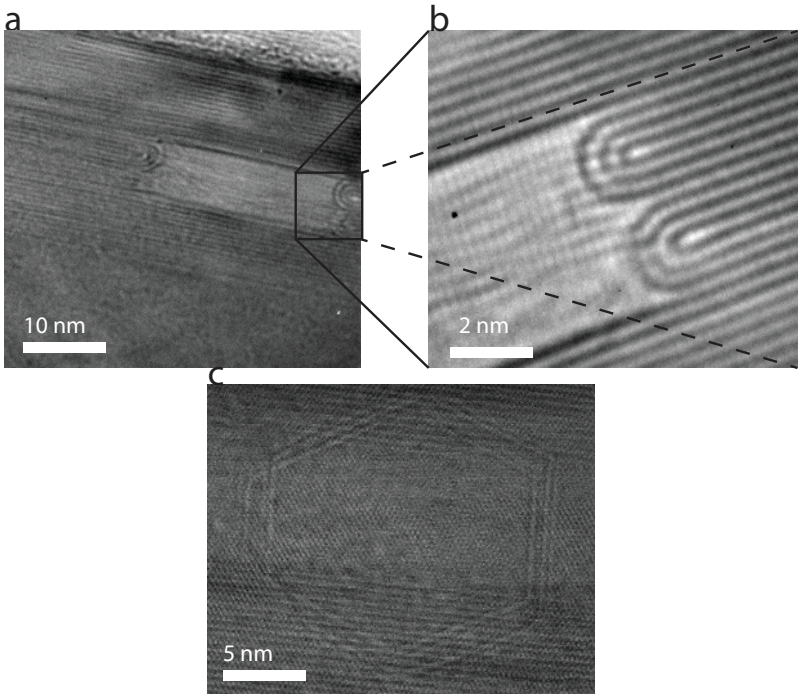

Figure 4.17: ***a,b*** *TEM images of defects in multiwalled BN nanotubes seen in HRTEM where bonded walls can be seen.* ***c*** *Polygonal pattern observed.*

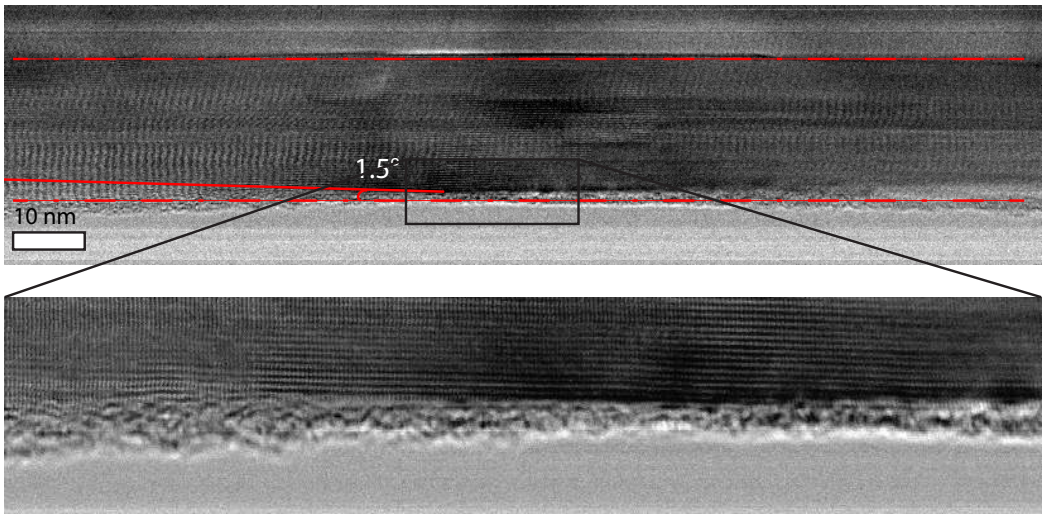

Figure 4.18: *BF HRSTEM image of a multiwalled BN nanotube in the vicinity of a highly diffracting area. The grain boundary at the join of two facets is clearly visible making a small angle with the nanotube axis.*

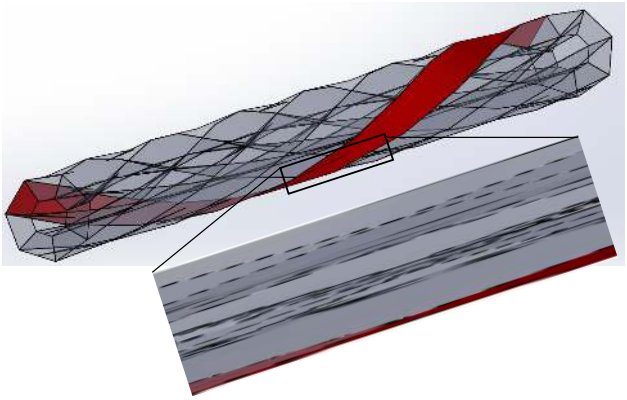

Figure 4.19: *3D structural model of the nanotube from Fig. 4.18 as characterized HRSTEM and a zoom in the part where the angle can be characterized.*

A schematic 3D representation of the nanotube structure using such a helix step value is presented in (Fig. 4.19). For a better understanding, one of the facets has been colored in red. The part of the nanotube where the angle is measured is also enlarged for an easier visualization.

4.7.2 EELS

Beside HREM imaging on multiwalled BN nanotubes, we have used EEL spectroscopy to characterize with a very high spatial resolution the presence of impurities within nanotubes. The spectrum acquired from the nanotube presented in (Fig. 4.20) shows a boron K edge signal at 188 eV and a nitrogen K edge signal at 399 eV (see also Fig. 4.20). No additional elements have been detected, even at the black spot location, in good agreement with the previous work performed by Golberg *et al.* [125]. This is an important result with significant impact for the interpretation of the optical properties BN nanotubes. Indeed, we can already say that the optical properties of these multiwalled nanotubes are not governed by impurities, but most probably by defects. An introduction to multiwalled BN nanotubes optical properties will be given in the next section.

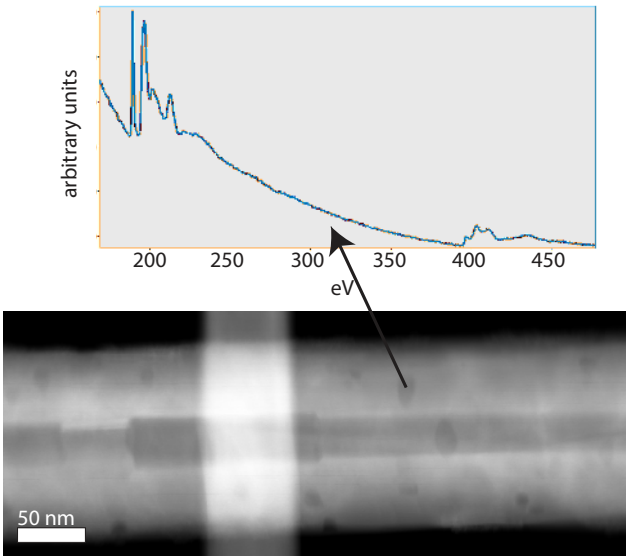

Figure 4.20: *bottom: HAADF image of a multiwalled BN nanotube; top: single spectrum extracted from a hyper spectral image and associated to 1 pixel in a defective area indicating that there is no significant impurity amount.*

4.8 Optical properties of BN nanotubes

Until now, in the literature, multiwalled BN nanotubes optical properties were derived from those known for BN crystals [128, 51]. Since the discovery of BN nanotubes, their optical properties have been investigated by photoluminescence using a laser at 193 nm [129], by photoluminescence excitation at 10 K in a synchrotron [130] and finally using a cathodoluminescence system integrated into a SEM [131]. The main result of these experiments is that BN nanotubes emit in the same energy range as the h-BN crystal (Fig. 4.21), displaying similar features at high energy and a broad band around 4 eV.

More precisely, photoluminescence experiments performed on BN multiwalled nanotubes show a series of emission peaks around 5.1-5.6 eV and also a broad band around 4 eV [128]. This work shows that luminescence is higher when the nanotube is suspended as compared to when contacted with the carbon grid. Other works performed on BN nanotubes report on the same kind of luminescence band around 5.4 eV [131, 132, 133, 134, 135].

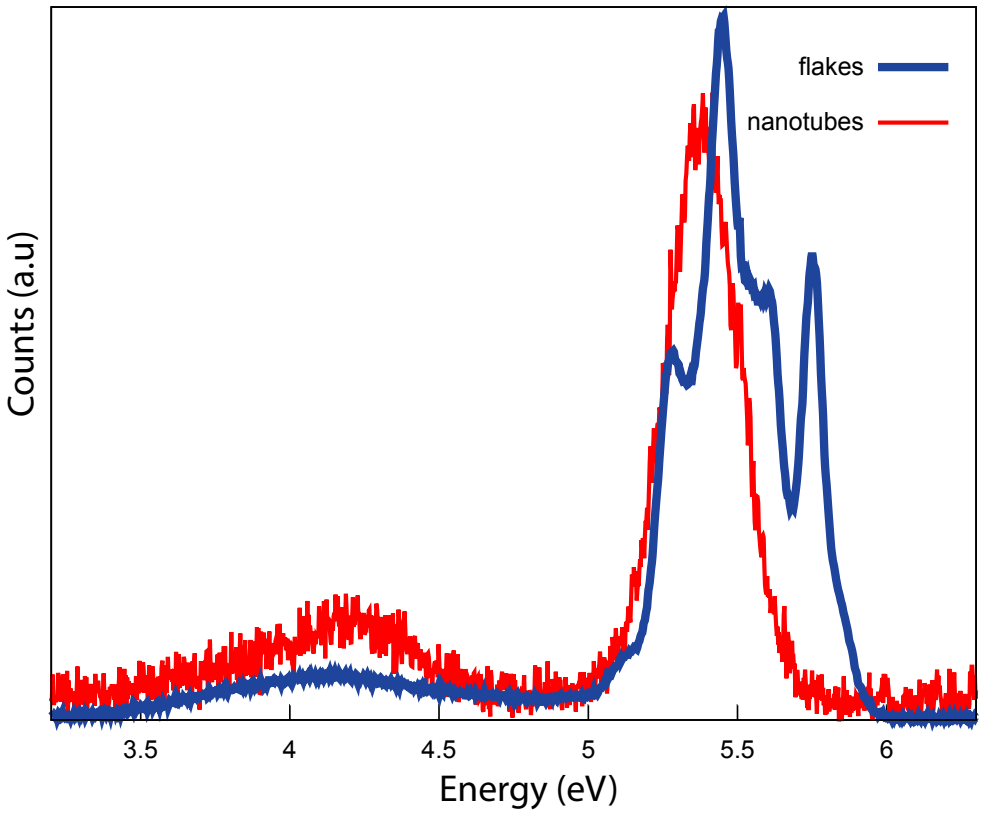

Figure 4.21: *CL spectra from h-BN crystal in blue and from multiwalled BN nanotubes in red. Both spectra display features in the same energy range, composed of a series of sharp peaks at high energy and a broad band around 4 eV*

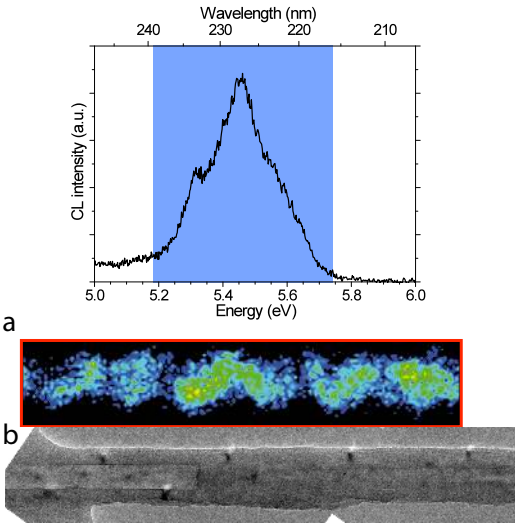

Figure 4.22: *Full CL spectrum.* ***a*** *CL filtered images recorded respectively at 5.49 eV [127].* ***b*** *TEM image of the same nanotubes.*

However, despite a large number of studies, no clear correlation between emission and structural characteristics has been provided until very recently. Pierret *et al.* [127] extending their results obtained on BN crystals [106] suggested that additional the emission of multiwalled BN nanotubes originated from self trapped excitons at grain boundaries between the facets of the tube. They provided a correlation between structural images of the nanotubes and CL filtered images recorded at a specific wavelength (see Fig. 4.22).

4.8.1 Spatially resolved CL

In this section, nanometric resolved cathodoluminescence experiments performed on multiwalled BN nanotubes within a STEM will be presented. The spectral features show strong inhomogeneities in the relative intensities as a function of the probe position (Fig. 4.23). Contrary to h-BN crystals, a nanotubes overall spectrum displays less shaped peaks at high energy. Figure 4.23 displays three example spectra recorded at random positions along the nanotube as well as an average spectrum. We will first

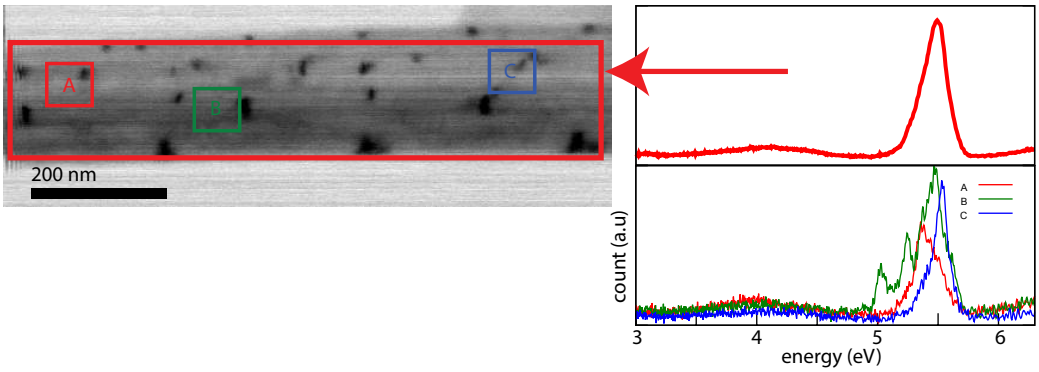

Figure 4.23: *Full cathodoluminescence spectrum recorded on multiwalled BN nanotubes and specific spectra recorded at different probe positions.*

focus our interest on the 4 eV broad band emission feature.

Broad band emission The broad band emission peak can be modeled by two Gaussian functions. It appears however that the emission maps associated with these two components show similar spatial distribution. Therefore, for a sake of simplicity, this bimodal feature will be referred later as a whole as "the broad band emission peak". This broad band emission is strongly localized within the nanotube (Fig. 4.24), typical emission spot size is around 100 m. This strongly localized emission could be associated to impurities or localized structural defects. Since the presence of impurities within the nanotubes has been excluded by the previous EELS study, only localized defective structures such as point defect can explain this strongly localized emission of the 4 eV peak. A deeper characterization of this emission within the h- BN flakes will be presented in the next chapter.

Excitonic emission (5-6 eV spectral range) Each of the energy peaks measured at high energy (in the 5- 6 eV spectral range) using our CL system appears at energy values very similar to what has been already reported in the literature for BN nanotubes and h-BN crystals. The characteristic energies are 5.46 eV, 5.52 eV, 5.62 eV, 5.32 eV. An additional emission peak at 5.1 eV of much weaker intensity is also detected. This emission

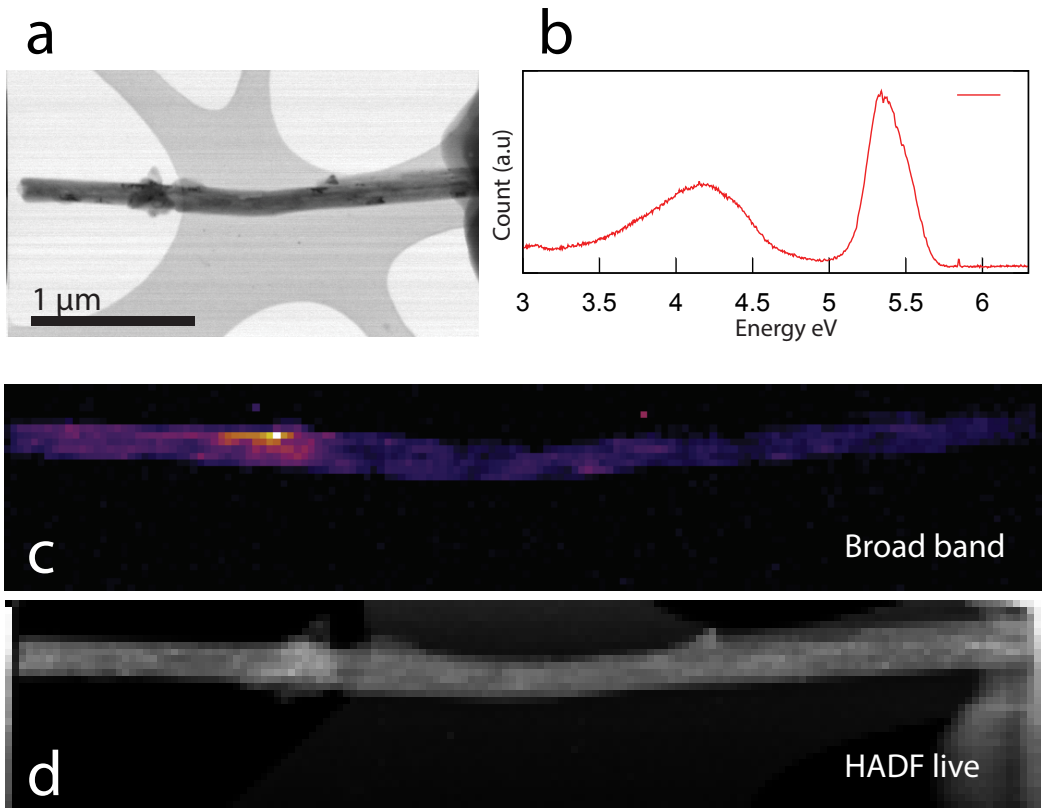

Figure 4.24: ***a*** *BF image showing the nanotube where is recorded the hyper-spectral image.* ***b*** *Full spectrum recorded on the nanotube.* ***c*** *emission map of the broad band emission.* ***d*** *HADF live image recorded simultaneously with the hyper-spectral image.*

is highly localized and is much scarcely detected. No correlation between this emission line and any specific defective structure has been evidenced yet. The peak at 5.52 eV can actually be described as a sum of two neighboring peaks at 5.62 eV and 5.46 eV as visible on Figure 4.23. It is streaking that the emission peaks detected in multiwalled BN nanotubes appear at the same energies as in h-BN crystals. According to our previous interpretation, these energies should correspond to emission peaks associated to different stacking configurations (see section 4.5 for a description of these stacking). Stacking changes within BN nanotubes is a reasonable hypothesis considering the faceted structure of the tubes, showing strong similarities with the faceted structure characterized along the folds. Furthermore the total absence of the 5.75 eV emission is compatible with a complete loss of the h-BN AA′ original stacking. From a more general point of view, despite their very large thickness, multiwalled BN nanotubes emission is very low as compared to h-BN flakes, which can be explained by the large quantity of defects seen in these nanotubes which surely quench the luminescence.

In figure 4.25.(a,b) are displayed the BF and BF live image synchronously acquired with a hyper-spectral image (spectrum image). A series of four emission lines at 5.10, 5.32, 5.46 and 5.62 eV is clearly visible in the overall cathodoluminescence spectrum of the tube (Fig. 4.23). As already mentioned, the 3 highest energy values (5.32, 5.46 and 5.62 eV) correspond to previously reported values for h-BN crystals and multi- walled BN nanotubes. In order to extract the spectral weight of each individual emission line, a multi-Lorentzian fitting routine has been applied to each spectrum of the spectrum image. Whereas peak energies were free parameters of the fitting procedure, no relevant energy shifts were detected within individual nanotubes and between different nanotubes. Intensity maps as derived from this analysis are shown in figure 4.25. Each map has been normalized independently on the basis of the most intense pixel. The resulting cathodoluminescence maps show an inhomogeneous localization of the emission all over the tube. A closer look at these emission maps points out a distribution of emission in a wave shape along the nanotube

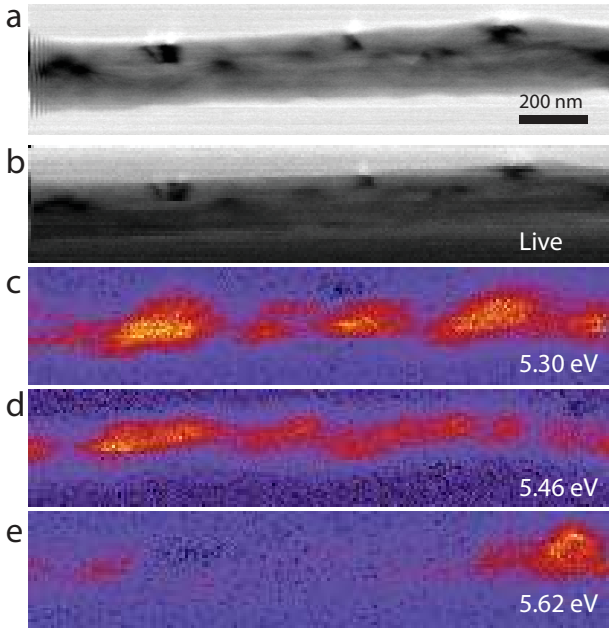

Figure 4.25: ***a**BF image and **b** live BF image from an isolated multiwalled BN nanotube. **c-e** CL intensity maps produced at 5.30 eV, 5.46 eV and 5.62 eV.*

axis. This wave shape along the nanotube can be explained if we consider one facet associated with a specific stacking. The emitting region associated with this facet rotating over the tube axis appears in projection as a wave . Therefore, we suggest that the overall emission pattern of a nanotube as seen in CL can be explained by the presence of facets of different stacking configurations. Additionally, we did not find any correlation between individual CL maps, which is compatible with our hypothesis that the observed pattern results from the additive contribution of different facets. Finally, it is worth mentioning the strong localization of the 5.62 eV peak. Considering the results obtained for h-BN crystals, this emission correspond to AA stacking configuration. Such emission could be associated to the bonded wall defect seen previously by HREM BF imaging where such high changes in the stacking are possible.

While investigating optical properties of different nanotubes with different diameters and helicities, no energy shift were detected and emission maps produced with the same components as used in the previous exam-

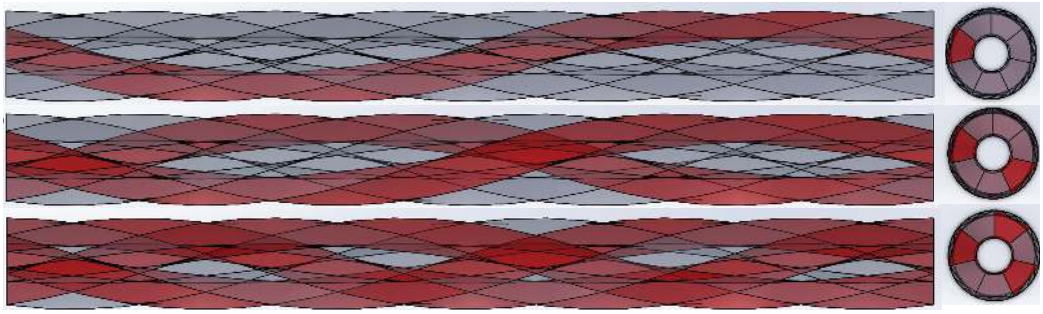

Figure 4.26: *schematic representation of CL maps for one, two or three facets with the same stacking configuration.*

ple leads to the same pattern of emission.

Using the 3D model presented in Figure 4.20 it is possible to produce a schematic representation of the emission pattern. Using transparency and lighting a single facet in red, the emission pattern seen in CL is reproduced successfully without taking into account the charge careers diffusion. With this representation, emission pattern when lightening one, two or three facets can be obtained. This schematic representation is just used as a help to understand cathodoluminescence maps obtained on the nanotubes. It cannot be considered as an accurate representation of the multiwalled nanotube structure. Figure 4.26 shows a representation for one, two and three facets with the same stacking. It shows that up to two facets with the same stacking it is still possible to see the wave shape pattern. For three facets with the same stacking, and considering the charge carrier diffusion in the system (few tens of nanometers), the wave shape pattern is not visible anymore.

In practice, in the case of multiwalled BN nanotubes it appears difficult to identify any existing correlation or anti-correlation relation between each intensity map due to their very close emission pattern. A useful representation is obtained by building an RGB image using each intensity map as a color component. In this image (Fig. 4.27), intensity maps for the 5.30 eV peak correspond to the blue color component, the 5.46 eV intensity map corresponds to the red color component and finally the 5.62 eV intensity map correspond to the green color. The result displayed in

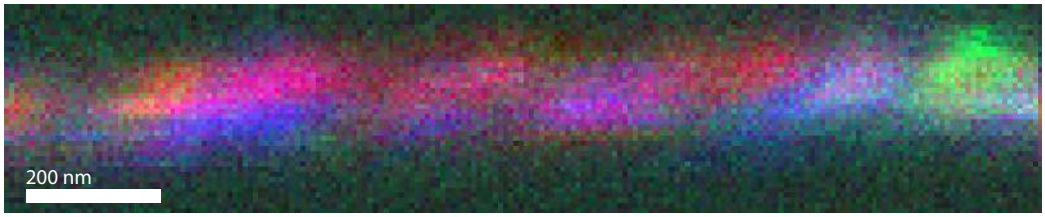

Figure 4.27: *RGB image reconstructed using each CL map as a color.*

Fig. 4.27 clearly shows the absence of correlation between the different emission maps. Therefore, this means that the different emission peaks are associated with one emission pattern extending along the tube, all single emission pattern being different from to another associated to single different facets of different stacking configuration.

To conclude, the results obtained on h-BN crystals, and extended to multiwalled BN nanotubes, allows to explain the correlation between optical properties and structural defects within multiwalled BN nanotubes. Five different stacking have been identified within the defects of h-BN crystals. The optical signature of three of them has been identified in multiwalled BN nanotubes as originating from different facets rotating along the nanotube axis. These results could be generalized to any types of h-BN nano-forms which should share the specificity that their emission properties are highly dependent on local changes in the stacking configuration. Moreover, the combination of nanometer resolved CL and high resolution microscopy coupled to mechanical quantum calculation has demonstrated to be a more appropriate tool to understand the optical properties of such semi-conducting nano forms.

CHAPTER 5

EMISSION RELATED TO POINT DEFECTS IN h-BN

IN THE PREVIOUS chapter, we discussed the emission of h-BN in the 5-6 eV energy range and we observed how several excitonic emission can be associated to stacking changes within the system. However, we mentioned already that the luminescence of h-BN can be far more complex. Indeed, quite often it is possible to observe in h-BN crystals an additional broad emission within the electronic band gap (3.0-4.5 eV) and four emission lines superposed to it (see for instance the full cathodoluminescence spectrum presented in Figure 5.1). These emission lines have been usually attributed to the presence of defect or impurities, but despite a large number of studies, their exact chemical nature and their structure have not been revealed yet. In this chapter we will give a new look on this problem, thanks to the unprecedented spatial resolution of our specific cathodoluminescence system. We will show that these middle band gap signals can be attributed to specific intrinsic or extrinsic point defects. In the latest part of the chapter, we will explore the quantum character of these emission lines using a Handburry-Brown-Twiss interferometer coupled to the cathodoluminescence set-up integrated in the STEM microscope. We will then demonstrate that a specific emission line at 4.2 eV has a non classical behavior corresponding to a previously unidentified single photon source in the far UV.

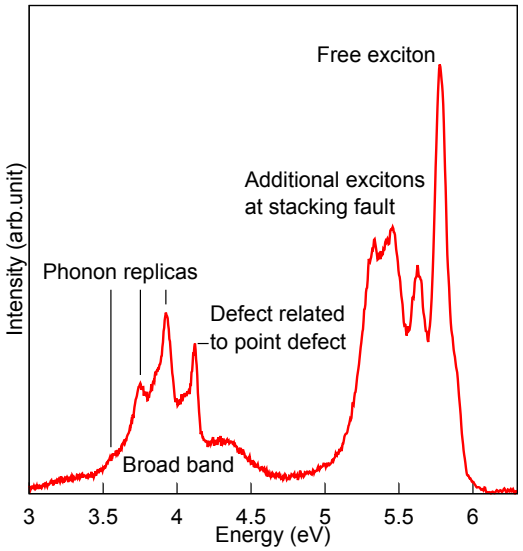

Figure 5.1: *Full cathodoluminescence spectrum obtained on a thin h-BN flakes. The two parts are visible, excitonic emission and middle of band gap emission.*

5.1 Broad band emission, (3.0-4.5 eV)

5.1.1 Previous studies

Common h-BN crystallite, as those available in commercial powders, present a broad band emission in the 3.0-4.5 eV range with a tail that can extend up to more than 5 eV. Although the first experimental observations date to more than fifty years ago, the origin of this middle band gap emission remains still unsettled [136, 137]. The very first photoluminescence experiments performed on h-BN crystals attributed this broad band to the main inter band transition emission. This lead to a strong underestimation of h-BN band gap that remained up to 2004.

Important new insights on the nature of this luminescence signal came from the works of Museur and coworkers [35, 36]. By variating the photoluminescence excitation laser energy they were able to demonstrate that the broad band disappears for a radiation energy below 5.2 eV. This demonstrated that the broad band can be described as a high energy zero phonon line followed by numerous phonon replicas. The same authors demonstrated also that this emission has a multiple exponent decay time be-

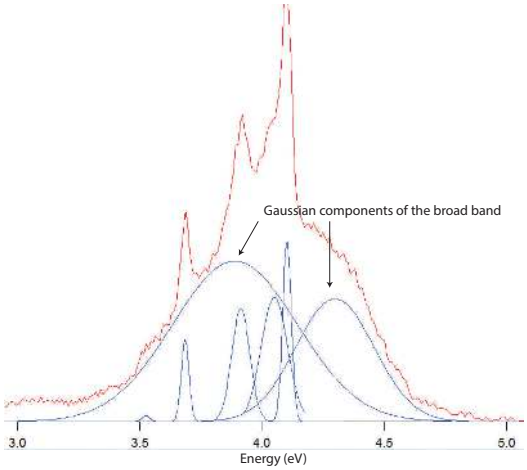

Figure 5.2: *Middle band gap emission with the 2 Gaussian component for the fit of the broad band.*

havior (in the time window 22-200 ns) which is compatible with recombination at donor acceptor pairs. This interpretation is now widely accepted [35, 36, 34, 44, 45] but many questions remain still open on the nature of this emission with a complete a lack of spatially resolved experiments.

5.1.2 Nanometric resolved CL

The broad band emission can be described as two large peaks correlated between each other that can be fitted by two Gaussian functions with fixed relative intensities (Fig. 5.2). Besides h-BN flakes, this emission has been observed identical in multiwalled BN nanotubes (see Sec. 4.8.1). Figure 5.3.a,b displays the DF image acquired simultaneously with the hyperspectral image and the HAADF image. Similarly to what described in the previous chapter for excitonic emissions, spatially resolved CL intensity maps can be produced for this spectral feature after fitting each spectrum of the spectrum image. A map of the spatial localization of this broad emission is presented in Figure 5.3.c. A very strong localization of the signal is clearly visible appearing as spots with typical sizes ranging from 80 up to few hundreds of nanometers. This behavior is described here for the first time and it is compatible with the presence of point defects or

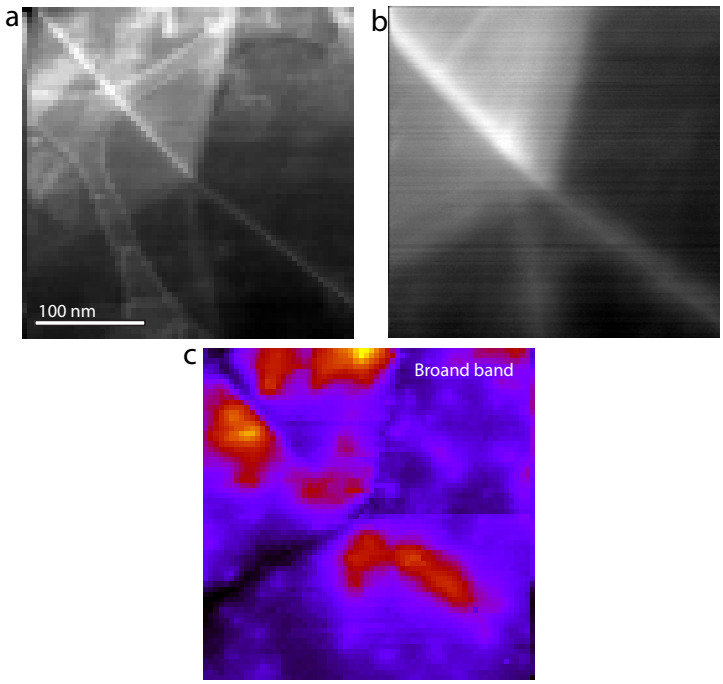

Figure 5.3: ***a*** *HAADF image acquired synchronously with the hyper-spectral image.* ***b*** *HAADF image.* ***c*** *Extracted intensity map of the broad band emission.*

donor acceptor pairs. It is important to notice that in correspondence to these intense emission spots excitonic emissions are very weak or totally absent (Fig. 5.3). This suggests that recombination effects at the origin of the broad band can strongly quench higher energy transitions.

Complementary information on the nature of this emission can be obtained from an observation of the time evolution of the signal under electron irradiation. In Figure 5.4 we present a CL spectrum acquired before irradiation (red line) and after 120 s of continuous irradiation with a 60 keV, ∼100 nA electron beam (blue line). Before irradiation the spectrum is dominated by four sharp peaks (this spectroscopic feature will be further discussed in section 5.2) and the broad emission is shallow. After irradiation the broad band has strongly increased. This indicates that the broad band is solely associated with intrinsic defects that can be generated by electron irradiation. Extrinsic defects such as impurities should thus be excluded.

Electron irradiation effects on BN materials have been largely studied by transmission electron microscopy in h-BN few layer flakes where atomic resolutions can be easily accessed [39, 138]. It has been shown that perfect h-BN is stable if irradiated with electrons below 80 keV [139, 140] but this threshold energy is strongly decreased in the presence of defects of degraded vacuum. After irradiation atomic vacancies are generated solely in the h-BN boron sub-lattice. Higher irradiation doses lead to the expansion of these primer defective sites and the formation of triangular holes whose borders are always nitrogen terminated [39, 38]. These results have been obtained in few layer h-BN flakes where knocked atoms can easily be sputtered from the system.

On few layer flakes, we suppose that sputtered atoms could be trapped within the layers leading to the presence of Frenkel pairs. The broad band observed by cathodoluminescence should thus be most likely associated to boron vacancies or Frenkel pairs. The theoretical work of Attacalite and coworkers have shown that boron vacancies would introduce additional optical active states within the optical band gap [141]. From another side, the Frenkel pair hypothesis would also eventually support the donor acceptor pair previously suggested by the works of Museur [36].

5.2 Sharp peaks related emission

Besides the broad emission band, both Figure 5.1 and 5.4 show a series of four sharp peaks within the band gap at 4.09 eV, 3.91 eV, 3.73 eV and 3.54 eV. The constant energy separation of 180 meV has suggested that the four peaks are phonon replicas of a zero phonon line. This hypothesis was confirmed by the work of Museur et al. who showed that when the crystal is irradiated with a photon energy below the highest energy peak, all other peaks disappear [35, 36]. The intensity of the peaks can strongly vary from sample to sample and they are totally absent in high purity crystals. This behavior indicates a correlation between sharp peak emission and extrinsic defects. The role of carbon or oxygen impurities has

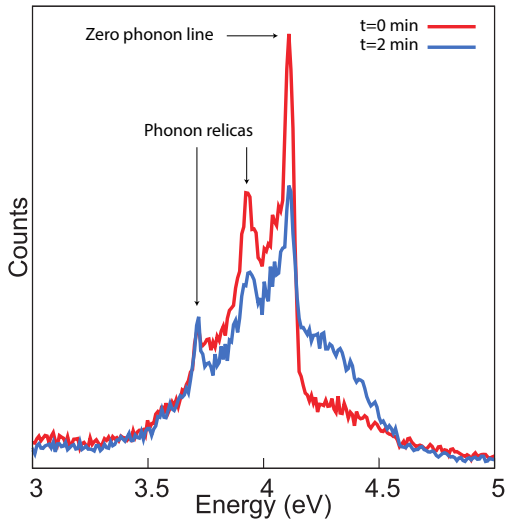

Figure 5.4: *CL spectra recorded on a h-BN flake, and a CL spectra recorded of the same area after two minutes of continuous irradiation with a 60 KeV electron beam. A strong increase of the broad band emission is clearly visible.*

been proposed [46]. Very recently Hara and coworkers [47] have reported strong photoluminescence changes when *h*-BN crystals were annealed in different atmospheres. Emission of the four sharp peaks was decreased by annealing in N_2, H_2 and NH_3 atmospheres at 1200 °C, with H_2 and NH_3 having more effect than N_2 . The annealing in a O_2 atmosphere increased the CL intensity remarkably at temperatures higher than 800 °C. These results suggested that the sharp peaks emission should be related to the presence of oxygen which can be removed in a reductive atmosphere. To conclude, time resolved photoluminescence experiments have shown that, unlikely the broad emission band, the sharp peaks emission has a very short exponential decay time of the order of 2 ns.

5.2.1 Nanometric CL characterization

In Figure 5.5 we present a CL hyper-spectral image obtained for an individual few-layer *h*-BN flake. The HADF image in Figure 5.5.a demonstrates the thickness homogeneity of a large part of the scanned region. In Figure 5.5.b we present three example spectra acquired at different excita-

tion probe positions showing strong inhomogeneities in the middle band gap luminescence. In the overall hyper-spectral image no relevant energy shifts neither changes in peaks shapes have been detected. The local weight of individual spectral features has been obtained through a multi-gaussian fitting routine applied to each individual spectrum (Fig. 5.5.c-f). Peaks at 3.73 eV, 3.91 eV and 4.09 eV are strongly spatial correlated, in a perfect agreement with the previously proposed phonon replicas hypothesis, whereas the broad band occurs at different zones of the *h*-BN flake. All emissions are strongly spatially localized and appear in the maps as bright spots with a full width half maximum of about 80 nm. This behavior, analogous to what previously observed for other semiconductor materials, suggests that both broad band and the sharp peaks might be associated to recombination at point defect.

5.2.2 Chemical investigations attempts

A way to characterized whether the sharp peak emission is effectively correlated to oxygen, is to be able to correlate spectroscopic information at a high spatial resolution with chemical analysis at the same scale. This capability is in principle accessible to our specific cathodoluminescence system which is integrated in a STEM microscope. Indeed, it is possible to simultaneously acquire CL with core EELS spectroscopy for constructing 4D hyper-spectral images. The main limitation is represented by the eventually different illumination times required by the two techniques to have a reasonable signal over noise ratio. The case of few layer boron nitride flakes appeared as a good compromise since both EELS and CL spectra could be obtained with a few tens of millisecond. However, if CL is a good technique for detecting point defects, EELS sensitivity is much lower and point defects can be easily seen only in the few layer limits where the CL signal gets too weak. After many attempts we were not able to detect any oxygen signal at the emission spots.

We explored then a different approach by increasing the oxygen content in the flakes in order to make it visible to core EELS. We tried to repro-

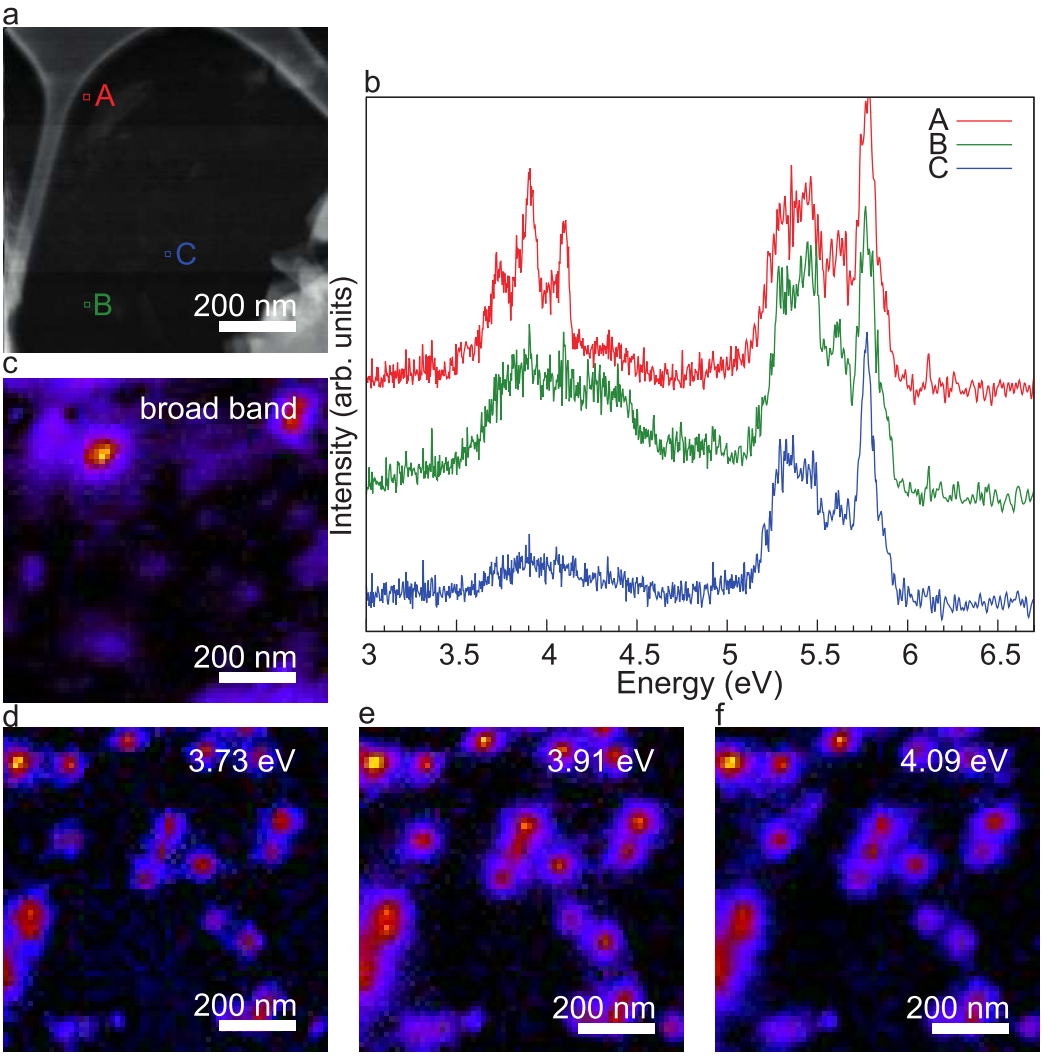

Figure 5.5: ***a*** *dark field images of an homogenous area of an individual BN flake.* ***b*** *individual spectra taken at specific probe positions indicated in panel* ***a****.* ***c-f*** *Emission maps for individual emission peak. Intensity is normalized independently within each individual map.*

duce the literature results illustrated in the previous section [47] by heating on$h$-BN powder in a pure oxygen atmosphere at 900°C for 10 hours. Successively TEM grids were prepared using the exfoliation techniques described in chapter 2 but avoiding purification techniques that might have reduced the sample. TEM observations confirm that flakes obtained after this thermal treatment keep the same aspect as non heated flakes and they show still a high crystalline level. However, neither an higher intensity for these sharp peaks was detected, neither a larger extension of the emitting regions. This result can certainly be attributed to the difficulty to oxidize h-BN many times discussed in the literature [142]. We can also not exclude that grid preparation post process to the thermal treatment might eventually alternate the flakes. If we were not able to oxidize the flakes we shown however, that flakes heaten in an H_2 atmosphere have many less emission spots.

5.3 Additional emission in h-BN in the near visible range

Most studies on the luminescence of h-BN are limited to the UV range. Only few works considered emissions in the visible for h-BN crystals and BN nano-forms doped with rare earths [143] but no reports exists in undoped forms. Our CL investigations showed a series of previously not reported three very sharp peaks at relatively low energies: 2.17 eV, 2.26 eV and 2.32 eV (Fig. 5.6.a). The 2.17 eV and 2.32 eV are spatially correlated and thus most probably associated to the same structure. All maps present typical bright spot of a lateral size of about 100 nm (Figure 5.6). Once more considering the localized character of the emission, and charge career diffusion lengths, these peaks could be associated to individual point defects within h-BN flakes.

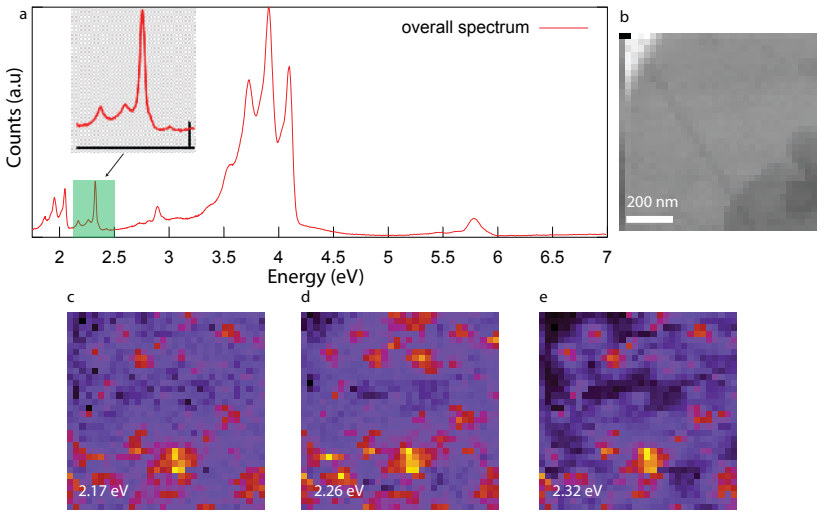

Figure 5.6: ***a*** *Overall spectrum recorded on a h-BN flakes covering a large energy range from the far UV to the visible.* ***b*** *HADF image recorded in parallel with the hyper-spectral image.* ***c*** *Intensity maps of the 2.17 eV emission peak.* ***d*** *Intensity maps of the 2.26 eV emission peak.* ***e*** *Intensity maps of the 2.32 eV emission peak.*

5.4 Point defects as single photon emitter sources

Single photon emitter sources are key factors for many applications in quantum computing. An assembly of such emitter sources coupled to linear optic elements and photo-detectors could be used to built up a quantum computer [99]. The easiest idea to produce an on demand photon emitting source consists in using an impulsive excitation on a two quantum levels system [100, 101] where for every excitation impulse, the system emits only one photon. An ideal photon emitter source should have the following properties:

- A high repetition time, thus a very short lifetime for the excited state.
- A very high quantum efficiency, all the impulse are then transformed into unique photons.

Quantum cryptography applications require no specific characteristics on the spectral width. However, a sharp emission allows a better isolation

of the light coming from the quantum system through the surrounding noise. Furthermore the wavelength of the emission have to be adapted to the propagation field.

In the sight of application, the single photon emitter system must be stable over long time, easy to set up and preferably composed of a cheap material. Nowadays, a large number of single photon emitter sources covering a large range of emission wavelength have already been characterized. At a first look, molecules seems the best candidates, their chemical properties are very well known and they are very easy to prepare in low concentration samples. However, their biggest drawback is their low photo-stability. Under optical excitation, molecules show an irreversible chemical transformation after emitting a certain numbers of photons (about 10^6). This phenomena is called photo-blanking and it appears after few milliseconds of excitation at saturation.

Other systems have also been studied, quantum boxes (Quantum Dots) of semi-conducting materials present good characteristics at low temperatures (4 K). These systems are photo-stable and excited states have a short lifetime of only about few nano-seconds. Another very well known single photon emitter source are color centers in diamond. Their major advantages come from a high photo-stability at room temperature, a short lifetime (11.6 ns) and a very high quantum efficiency close to one.

An efficient and high-quality single-photon source is needed to implement quantum key distribution, quantum repeaters and photonic quantum information processing. In a recent study it has been identified a new ultra-bright, room-temperature, photo-stable single photon sources at 694 nm in a device-friendly material, silicon carbide (SiC) [144]. This source is based on a unique punctual carbon anti-site vacancy pair, created by carefully optimized electron irradiation and annealing of ultra-pure SiC. At long wavelength, single photons should be transmitted in optical fibers due to large losses in the air. Oppositely ultraviolet single photon sources could be used in free space communication and would benefit to miniaturized quantum information circuits [145, 146] However, it is still challenging to produce a high-efficiency high energy single photon source based

on wide-bandgap semiconductors. Only very recently it has been obtained a bright UV single photon source in a single InGaN quantum dot embedded in an obelisk-shaped GaN nano-structure [147]. This structures requires a hard synthesis process and thus it is not suitable for high scale applications.

In section

5.4.1 The 4.09 eV peak

Using the HBT interferometer coupled to the VG-STEM microscope described in Sec. 3.3.2 we have investigated the quantum nature of the series of sharp lines in the middle band gap. Figure 5.7.a, shows an HADF image of a large h-BN flake with a rather homogeneous thickness. Figure 5.7.b presents a CL filtered image of the same region obtained employing an optical filter in the 300 nm to 340 nm wavelength gamma which selects the 4.2 eV zero phonon line emission and two of its phonon replicas plus part of the broad emission band (see Figure 5.7.c). The sharp lines are significantly more intense than the broad band and thus they appear as brighter spots in the filtered image.

Spectrum 5.7.c was acquired in the highlighted region of Figure 5.7.b, the broad band contribution appears particularly weak. Due to the strong intensity of the signal only few seconds are necessary to perform the interferometry experiments. This short time limits irradiation effects that, as described in section 5.1, would have enhanced the broad band emission and thus generated a parasite background.

The auto-correlation function $g(^2)(t)$ recorded at this bright spot is displayed on Figure 5.7.d. A dip at a delay time $\Delta t = 0ns$ is visible in the graph with $g(^2)(t)$ reaching a minimum of about 0.5. Shallower values of the dip are obtained in regions where the broad band is stronger. This is a clear indication of a single photon emitting source. Furthermore, the width of the dip, about 3 ns allows to have a direct measure of the lifetime of the excited state. The value obtained is in a good agreement with estimations obtained by time resolved photoluminescence ex-

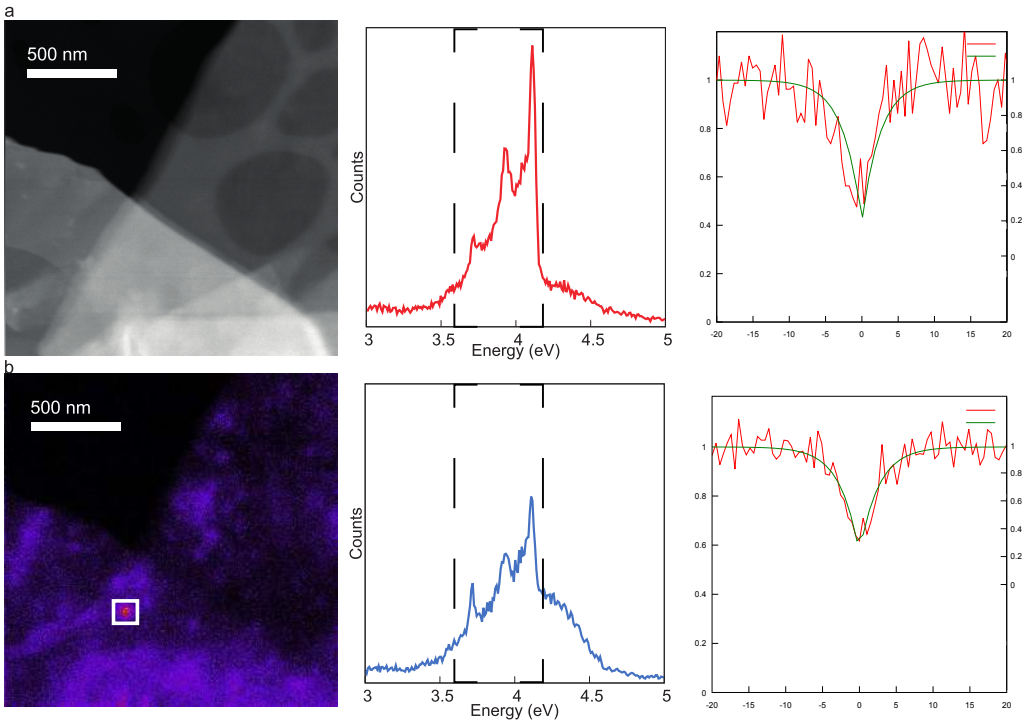

Figure 5.7: ***a*** *HADF of an h-BN flakes.* ***b*** *Filtered images obtain using the energy widow show on spectrum.* ***c*** *CL spectrum recorded on the bright spot on the filtered image.* ***d*** *Auto-correlation function recorded on this bright spot displaying a dip at 0 delay.*

periments [36]. This experiment provides a definitive confirmation of the hypothesis that sharp peaks in the h-BN middle band gap is associated to point defects. Furthermore, we have identified that defective h-BN is an extremely promising single photon source in the near UV. Both the strong intensity of the signal and the short life time of the excited state appears favorable behaviors to possible technological applications.

5.4.2 The 2.1-2.3 eV peaks

In order to investigate the quantum nature of emission described in section 5.3, all lenses and collection system used in the interferometer experiment have been adapted to work in the visible range. Contrary to UV defects described in section 5.4.1, these emission lines appear to be strongly unstable under the electron beam. In Figure 5.8 we present a series of successive filtered images acquired using the detectors of the HBT experiment. While scanning the surface of the sample, it is possible to observe the formation of a defect (Fig. 5.8.b): half a spot is clearly visible indicating that emission is produced after the electron has illuminated the center. This emission spot is relatively stable under the beam for one or two scan (Fig. 5.8.c.d) with no intensity variation. After few more scans, the emission spot completely disappears (Fig. 5.8.e). This behavior has been reported for numerous emission spot, and it can only be explained by intrinsic defects generated and annihilated by electron irradiation. These instabilities were a major problem to perform interferometer experiments which usually need quite long acquisition times[1] and haven't allowed thus to conclude on the quantum nature of this emission

[1]The intensity of single photon emitter sources is solely related to the life time of the exited state and not to illumination. The time to acquire an auto-correlation function with an acceptable signal over noise ratio is thus mostly associated to the system investigated and in only a minor part to the instrumentation.

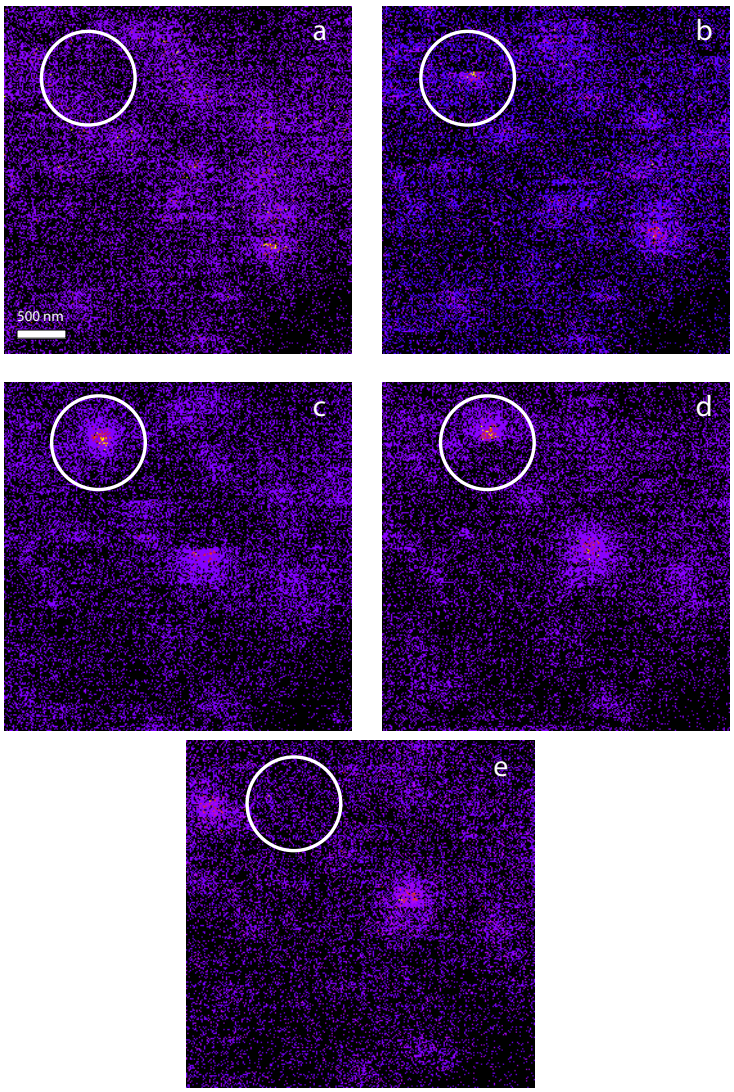

Figure 5.8: ***a*** *Filtered image corresponding to the first time this area is scanned.* ***b*** *Fileted image corresponding the the second scanning time where the emission spot is created in the white circle .* ***c*** *Filtered image where it is clearly seen that the emission spot is stable under the third scanning time of the area.* ***d*** *Filtered image corresponding to the fourth scanning time where the emission spot start to be destroyed.* ***e*** *Filtered image of the fifth scan where the emission spot is completely destroyed.*

CHAPTER 6

CONCLUDING REMARKS AND PERSPECTIVES

IN THIS THESIS works several aspects of the optical properties of h-BN crystals and nanotubes have been investigated using an approach combining different imaging and spectroscopy techniques in electron microscopy. Further information complementary to experiments was provided by state of the art theoretical spectroscopy simulations. The purpose of this chapter is to summarize the main results obtained and to give an overview of new research lines that might be opened by this study.

The origin of the complex emission spectrum of h-BN was a long term question to which only partial answers had been provided. This was mainly due to the incapability of previous studies to combine spectroscopic measurements and structural characterization at the necessary spatial resolution. Photoluminescence techniques can be highly resolved in energy, but they provide an information averaged over a wide region of the samples and thus they are not optimal for studying optical active centers in semiconductors. Cathodoluminescence is a much more adapted technique since electrons can be focused in narrow probes and thus very limited regions can be illuminated. Furthermore the high energy of the electron beam allows to excite high energy states that otherwise would have required short wavelength lasers.

Energy filtered cathodoluminescence images previously reported on h-BN had shown inhomogeneities in the spatial localization of the emission spectrum. The sub-micrometric spatial resolution of these experiments was however still larger than the characteristic scale of defects in-

volved in the luminescence process. Furthermore filtered image can fail in separating emission signals too close in energy. In this work we were able to go beyond literature results thanks to the capabilities of the new cathodoluminescence system integrated in a STEM microscope recently installed in our laboratory. This experimental setup provides a spatial resolution as low as a few nanometers and it permits to acquire at each probe position a full emission spectrum and thus to build hyper-spectral images. Our study on the luminescence of BN materials have been separated into two parts: in a first part we have investigated high energy sharp peaks close to the free exciton, in a second part emissions in the middle of the band gap were explored.

Cathodoluminescence maps in the high energy region have shown strong localizations at lines crossing the sample which appeared also clearly in HAADF images. Successive high resolution bright field focal series in a STEM microscope allowed to identify these lines as plane folds crossing the sample. For the first time, the dominant luminescence in h-BN flakes could be associated with a specific class of line defects, plane faults which were previously not described in this material. A more in-depth interpretation of these experimental observations came from complementary simulations conducted in the framework of the many body perturbation theory (collaboration with M. Amato LSI, Ecole Polytechnique). For multi-layer BN structures such as BN nanotubes, it is well known that the energy excess due to curvature is relaxed through faceting. Different stacking orders correspond to different facets, in the case of h-BN five high symmetry configurations can be obtained. Theoretical simulations on bulk structures have shown that to these discrete stacking correspond different excitons with well defined energies in the range of what is observed experimentally. The observation of different cathodoluminescence signals at different facets of multi-walled BN nanotubes provided a further confirmation of our interpretation for BN flakes. We should mention however that whereas the stacking changes model was proposed on the basis of microscopy images, theoretical consideration and previous observation on analogous flakes, they were not directly observed in this study.

A further microscopy study on the atomic structure at folds in h-BN and at facets in multiwalled BN nanotubes was thus highly suitable. In this thesis high resolution images were performed into a different microscope that used for cathodoluminescence. The observation of both atomic structure and luminescence on the same object was achieved only thanks to a big effort to locate precisely individual flakes on the TEM grid. More complete information could eventually be provided if the atomic resolution could be directly combined to CL.

The scale at which additional excitons appear in cathodoluminescence images is larger than the effective size of the folds. This is mainly due to the diffusion length of the excitation which can reach several tens of nanometers. A much higher localization could be achieved when looking at absorption phenomena, like in EEL spectroscopy, in which diffusion does not take place. To clearly observe excitons in BN, it is however fundamental to have very thin samples for which the loss function can be well approximated by the absorption function [148]. Excitons at 6.1 eV have been observed already by low loss EELS in few layer h-BN flakes and few walled BN nanotubes [149, 150]. On the basis of this thesis work, we expect that a shift might be observed by EELS at stacking changes in few layer systems. However, since all excitons occur in a narrow energy range, a monochromatic system integrated in the microscope is most likely to be needed. Ideally, cathodoluminescence and EELS measurements should be performed at the same time.

This study has emphasized the role of stacking changes in h-BN flakes in defining the specific optical response in the ultraviolet regime. Up to now metastable h-BN stackings were discussed from a morphological and energetic point of view but little attention was paid to their optical and electronic properties [151, 120, 121, 122]. Only recently it has been demonstrated that few layer h-BN structures with non centro-symmetric configurations (flakes with odd number of layers or twisted bi-layer flakes) have remarkable second harmonic generation and thus a great potential for nonlinear optics applications [152, 153, 154]. Stacking faults in layered materials are native abundant due to their low activation energy and they can

be easily induced by limited mechanical deformations. Furthermore, recent developments in 2D crystals transfer techniques allow to build multilayer structures with arbitrary stacking orientations [153, 155]. This study suggests that deliberately introducing stacking faults in h-BN flakes can be used as a way to tune the emission spectrum in the far UV region. From a complementary point of view, the analysis of the excitonic response can be employed as a powerful tool to precisely map structural deformations in h-BN crystallite and in new 2D hetero-structures. Finally we should mention that the role of stacking might be relevant when considering the optical behavior of 2D hetero-structures.

The latest part of this thesis work was dedicated to the study of middle band gap emissions in *h*–BN, mainly the 3.0–4.5 eV broad band and the series of sharp lines superposed to it. Previous studies have suggested that these signals could be related to point defects. Cathodoluminescence maps obtained in this work have shown that all these signals appear as bright spots with a lateral size of only few tens of nanometers. This high localization is of the order of magnitude of excitation diffusion lengths and it supports the hypothesis of a correlation to point defects. The observation of an enhancing of the broad band emission under constant illumination has demonstrated that the origin of this spectral feature are intrinsic defects that can be commonly generated by electron irradiation (boron vacancies or Frenkel pairs).

The cause of the sharp lines in the middle of the band gap had been previously attributed to the presence of oxygen. Several attempts to correlate CL and EELS chemical analysis were unable to confirm this statement but we attribute this fail mostly to instrumental limitations. Indeed, it is not yet possible to combine these spectroscopic techniques within microscopes with atomic electron probes as required for point defects imaging and chemical analysis. The quantum nature of the middle band gap sharp emission peaks was investigated through an Handburry-Brow-Twiss spectrometer coupled to the cathodoluminescence system of our STEM microscope. The presence of a dip in the auto-correlation function demonstrated a non classical emission behavior thus the presence of a single photon

source in the far UV. Currently, the search for new single photon sources is a very dynamic research area. Up to now only few emitters have been identified in the UV and thus we expect that our might have a relevant impact in the field.

During this thesis, we began to investigate the optical behavior of the cubic phase of boron nitride in which several questions remain still open [156, 157]. Preliminary results have shown an emission spectrum as rich as those of *h*-BN with several localized emission peaks in the visible and far UV spectral region. The possibility of previously unidentified new single photon emission sources is currently under investigation.

To conclude, some of the instrumental limitations that were encountered in this work could be overcome in a close future. The cathodoluminescence system employed is currently still under active development and it will be soon adapted to a large class of transmission electron microscopes. Within our laboratory, we are currently integrating the CL system into a STEM microscope equipped with a Helium cooled sample stage that could thus allow a better spectral resolution. Furthermore, new experimental capabilities are expected by the forthcoming installation at our laboratory of a new aberration corrected STEM microscope equipped with a monochromator and cathodoluminescence. For instance, it will be possible to correlate cathodoluminescence and low loss EELS spectroscopy in a lower energy region and thus to study a big class of low band gap materials.

BIBLIOGRAPHY

[1] S. Nakamura, T. Mukai, and M. Senoh, *High-Power GaN P-N Junction Blue-Light-Emitting Diodes*, J. Appl. Phys. **30**, L1998 (1991).

[2] M. A. Khan, J. N. Kuznia, A. R. Bhattarai, and D. T. Olson, *Metal semiconductor field effect transistor based on single crystal GaN*, Applied Physics Letters **62**, 1786 (1993).

[3] A. Denis, G. Goglio, and G. Demazeau, *Gallium nitride bulk crystal growth processes: A review*, Materials Science and Engineering: R: Reports **50**, 167 (2006).

[4] J. Nelayah, M. Kociak, O. Stan, F. J. Garcde Abajo, M. TencL. Henrard, D. Taverna, I. Pastoriza-Santos, L. M. Liz-Marz and C. Colliex, *Mapping surface plasmons on a single metallic nanoparticle*, Nat Phys **3**, 348 (2007).

[5] M. Kociak and O. Stéphan, *Mapping plasmons at the nanometer scale in an electron microscope.*, Chem. Soc. Rev. **43**, 3865 (2014).

[6] J. Christen, M. Grundmann, and D. Bimberg, *Scanning cathodoluminescence microscopy: A unique approach to atomic scale characterization of heterointerfaces and imaging of semiconductor inhomogeneities*, Journal of Vacuum Science & Technology B **9**, 2358 (1991).

[7] M. Grundmann, J. Christen, N. N. Ledentsov, J. Bohrer, D. Bimberg, S. S. Ruvimov, P. Werner, U. Richter, U. Gosele, J. Heydenreich, V. M. Ustinov, A. Y. Egorov, A. E. Zhukov, P. S. Kopev, and Z. I. Alferov, *Ultranarrow Luminescence Lines From Single Quantum Dots*, Physical Review Letters **74**, 4043 (1995).

[8] J. P. Garayt, J. M. Gerard, F. Enjalbert, L. Ferlazzo, S. Founta, E. Martinez-Guerrero, F. Rol, D. Araujo, R. Cox, B. Daudin, B. Gayral, L. S. Dang, and H. Mariette, *Study of isolated cubic GaN quantum dots by low-temperature cathodoluminescence*, Physica E-Low-Dimensional Systems & Nanostructures **26**, 203 (2005).

[9] D. Bimberg and J. Christen, *Cathodoluminescence Investigations of Gaas Multiple Quantum-wells*, Acta Physica Polonica A **69**, 841 (1986).

[10] P. R. Edwards, L. K. Jagadamma, J. Bruckbauer, C. Liu, P. Shields, D. Allsopp, T. Wang, and R. W. Martin, *High-Resolution Cathodoluminescence Hyperspectral Imaging of Nitride Nanostructures*, Microscopy and Microanalysis **18**, 1212 (2012).

[11] L. F. Zagonel, S. Mazzucco, M. Tence, K. March, R. Bernard, B. Laslier, G. Jacopin, M. Tchernycheva, L. Rigutti, F. H. Julien, R. Songmuang, and M. Kociak, *Nanometer Scale Spectral Imaging of Quantum Emitters in Nanowires and Its Correlation to Their Atomically Resolved Structure*, Nano Letters **11**, 568 (2011).

[12] D. Bimberg and J. Christen, *Cathodoluminescence Images of Quantum-wells and Wires*, Microscopy of Semiconducting Materials 1993 (1993).

[13] S. K. Lim, M. Brewster, F. Qian, Y. Li, C. M. Lieber, and S. Gradecak, *Direct Correlation between Structural and Optical Properties of III-V Nitride Nanowire Heterostructures with Nanoscale Resolution*, Nano Letters **9**, 3940 (2009).

[14] H. S. Leipner, R. Scholz, F. Syrowatka, H. Uniewski, and J. Schreiber, *Interaction of copper with dislocations in GaAs*, Journal De Physique Iii **7**, French Minist Res; Univ Aix Marseille III; SGS Thomson Co (1997).

[15] N. Yamamoto, H. Itoh, V. Grillo, S. F. Chichibu, S. Keller, J. S. Speck, S. P. DenBaars, U. K. Mishra, S. Nakamura, and G. Salviati, *Cathodoluminescence characterization of dislocations in gallium nitride using a transmission electron microscope*, Journal of Applied Physics **94**, 4315 (2003).

[16] K. Maehashi, H. Nakashima, F. Bertram, P. Veit, and J. Christen, *Threading dislocation reduction in GaAs films on thin Si substrates*, Physica E **2**, 772 (1998).

[17] M. Bickermann, S. Schimmel, B. M. Epelbaum, O. Filip, P. Heimann, S. Nagata, and A. Winnacker, *Structural defects in aluminium nitride bulk crystals visualized by cathodoluminescence maps*, Physica Status Solidi C: Current Topics In Solid State Physics, Vol 8, No 7-8 **8**, European Mat Res Soc (EMRS) (2011).

[18] I. Tischer, M. Feneberg, M. Schirra, H. Yacoub, R. Sauer, K. Thonke, T. Wunderer, F. Scholz, L. Dieterle, E. Mueller, and D. Gerthsen, *Stacking fault-related luminescence features in semi-polar GaN*, Physica Status Solidi B-basic Solid State Physics **248**, 611 (2011).

[19] Y. Taniyasu, M. Kasu, and T. Makimoto, *An aluminium nitride light-emitting diode with a wavelength of 210 nanometres*, Nature **441**, 325 (2006).

[20] A. Khan, K. Balakrishnan, and T. Katona, *Ultraviolet light-emitting diodes based on group three nitrides*, Nat. Photon. **2**, 77 (2008).

[21] K. Watanabe, T. Taniguchi, and H. Kanda, *Direct-bandgap properties and evidence for ultraviolet lasing of hexagonal boron nitride single crystal*, Nat. Mater. **3**, 404 (2004).

[22] L. Wirtz, A. Marini, M. Gruning, and A. Rubio, *Excitonic effects in optical absorption and electron-energy loss spectra of hexagonal boron nitride*, arXiv:cond-mat/0508421 (2005).

[23] K. Watanabe, T. Taniguchi, T. Niiyama, K. Miya, and M. Taniguchi, *Far-ultraviolet plane-emission handheld device based on hexagonal boron nitride*, Nat. Photon. **3**, 591 (2009).

[24] H. W. Kroto, J. R. Heath, S. C. O'Brien, R. F. Curl, and R. E. Smalley, *C60: Buckminsterfullerene*, Nature **318**, 162 (1985).

[25] S. Iijima, *Helical microtubules of graphitic carbon*, Nature **354**, 56 (1991).

[26] K. S. Novoselov, A. K. Geim, S. V. Morozov, D. Jiang, Y. Zhang, S. V. Dubonos, I. V. Grigorieva, and A. A. Firsov, *Electric Field Effect in Atomically Thin Carbon Films*, Science **306**, 666 (2004).

[27] X. Blase, A. Rubio, S. G. Louie, and M. L. Cohen, *Stability and Band Gap Constancy of Boron Nitride Nanotubes*, EPL (Europhysics Letters) **28**, 335 (1994).

[28] N. G. Chopra, R. J. Luyken, K. Cherrey, V. H. Crespi, M. L. Cohen, S. G. Louie, and A. Zettl, *Boron nitride nanotubes*, Science **269**, 966 (1995).

[29] W.-Q. Han, L. Wu, Y. Zhu, K. Watanabe, and T. Taniguchi, *Structure of chemically derived mono- and few-atomic-layer boron nitride sheets*, Applied Physics Letters **93**, 223103 (2008).

[30] C. R. Dean, A. F. Young, I. Meric, C. Lee, L. Wang, S. Sorgenfrei, K. Watanabe, T. Taniguchi, P. Kim, K. L. Shepard, and J. Hone, *Boron nitride substrates for high-quality graphene electronics*, Nat Nano **5**, 722 (2010).

[31] J. Xue, J. Sanchez-Yamagishi, D. Bulmash, P. Jacquod, A. Deshpande, K. Watanabe, T. Taniguchi, P. Jarillo-Herrero, and B. J. LeRoy, *Scanning tunnelling microscopy and spectroscopy of ultra-flat graphene on hexagonal boron nitride*, Nat Mater **10**, 282 (2011).

[32] W. Gannett, W. Regan, K. Watanabe, T. Taniguchi, M. F. Crommie, and A. Zettl, *Boron nitride substrates for high mobility chemical vapor deposited graphene*, Applied Physics Letters **98**, 242105 (2011).

[33] R. Decker, Y. Wang, V. W. Brar, W. Regan, H.-Z. Tsai, Q. Wu, W. Gannett, A. Zettl, and M. F. Crommie, *Local Electronic Properties of Graphene on a BN Substrate via Scanning Tunneling Microscopy*, Nano Lett. **11**, 2291 (2011).

[34] T. Taniguchi and K. Watanabe, *Synthesis of high-purity boron nitride single crystals under high pressure by using Ba solvent*, Journal of Crystal Growth **303**, 525 (2007).

[35] L. Museur, D. Anglos, J.-P. Petitet, J.-P. Michel, and A. V. Kanaev, *Photoluminescence of hexagonal boron nitride: Effect of surface oxidation under UV-laser irradiation*, J. Lumin. **127**, 595 (2007).

[36] L. Museur, E. Feldbach, and A. Kanaev, *Defect-related photoluminescence of hexagonal boron nitride*, Phys. Rev. B **78**, 155204 (2008).

[37] N. Alem, R. Erni, C. Kisielowski, M. D. Rossell, W. Gannett, and A. Zettl, *Atomically thin hexagonal boron nitride probed by ultrahigh-resolution transmission electron microscopy*, Phys. Rev. B **80**, 155425 (2009).

[38] J. C. Meyer, A. Chuvilin, G. Algara-Siller, J. Biskupek, and U. Kaiser, *Selective Sputtering and Atomic Resolution Imaging of Atomically Thin Boron Nitride Membranes*, Nano Lett. **9**, 2683 (2009).

[39] C. Jin, F. Lin, K. Suenaga, and S. Iijima, *Fabrication of a Freestanding Boron Nitride Single Layer and Its Defect Assignments*, Phys. Rev. Lett. **102**, 195505 (2009).

[40] N. Alem, Q. M. Ramasse, C. R. Seabourne, O. V. Yazyev, K. Erickson, M. C. Sarahan, C. Kisielowski, A. J. Scott, S. G. Louie, and A. Zettl, *Subangstrom Edge Relaxations Probed by Electron Microscopy in Hexagonal Boron Nitride*, Phys. Rev. Lett. **109**, 205502 (2012).

[41] O. Cretu, Y.-C. Lin, and K. Suenaga, *Evidence for Active Atomic Defects in Monolayer Hexagonal Boron Nitride: A New Mechanism of Plasticity in Two-Dimensional Materials*, Nano Lett. **14**, 1064 (2014).

[42] J. H. Warner, M. H. Reli, A. Bachmatiuk, and B. Bner, *Atomic Resolution Imaging and Topography of Boron Nitride Sheets Produced by Chemical Exfoliation*, ACS Nano **4**, 1299 (2010).

[43] K. Suenaga, H. Kobayashi, and M. Koshino, *Core-Level Spectroscopy of Point Defects in Single Layer h-BN*, Phys. Rev. Lett. **108**, 075501 (2012).

[44] B. Clubine, *Synthesis and characterization of bulk single crystal hexagonal boron nitride from metal solvents*, Thesis, Kansas State University, 2012, National Science Foundation; Department of Homeland Security.

[45] M. G. Silly, P. Jaffrennou, J. Barjon, J.-S. Lauret, F. Ducastelle, A. Loiseau, E. Obraztsova, B. Attal-Tretout, and E. Rosencher, *Luminescence properties of hexagonal boron nitride: Cathodoluminescence and photoluminescence spectroscopy measurements*, Phys. Rev. B **75**, 085205 (2007).

[46] L. Liu, T.-K. Sham, W. Han, C. Zhi, and Y. Bando, *X-ray Excited Optical Luminescence from Hexagonal Boron Nitride Nanotubes: Electronic Structures and the Role of Oxygen Impurities*, ACS Nano **5**, 631 (2011).

[47] K. Hara, X. Liu, M. Yamauchi, Y. Kawanishi, H. Kominami, and Y. Nakanishi, *Effects of annealing on 320 nm cathodoluminescence from hexagonal boron nitride powders*, Phys. Status Solidi C **8**, 2509 (2011).

[48] W. H. Balmain, *Bemerkungen r die Bildung von Verbindungen des Bors und Siliciums mit Stickstoff und gewissen Metallen*, J. Praktische Chemie, **27** (1842).

[49] P. Wer, Liebigs Ann. Chem, **74** (1850).

[50] D. Golberg, Y. Bando, Y. Huang, T. Terao, M. Mitome, C. Tang, and C. Zhi, *Boron nitride nanotubes and nanosheets*, ACS nano **4**, 2979 (2010).

[51] K. Watanabe, T. Taniguchi, and H. Kanda, *Direct-bandgap properties and evidence for ultraviolet lasing of hexagonal boron nitride single crystal*, Nat Mater **3**, 404 (2004).

[52] A. Rubio, J. Corkill, and M. Cohen, *Theory of graphitic boron nitride nanotubes*, Phys. Rev. B **49**, 5081 (1994).

[53] N. Chopra, R. Luyken, K. Cherrey, V. Crespi, M. Cohen, S. Louie, and A. Zettl, *Boron Nitride Nanotubes*, Science **269**, 966 (1995).

[54] T. Oku, Synthesis, atomic structures and properties of boron nitride nanotubes, in *Physical and Chemical Properties of Carbon Nanotubes*, edited by S. Suzuki, InTech, 2013.

[55] A. Loiseau, F. Willaime, N. Demoncy, G. Hug, and H. Pascard, *Boron nitride nanotubes with reduced numbers of layers synthesized by arc discharge*, Phys. Rev. Lett. **76**, 4737 (1996).

[56] D. Golberg, Y. Bando, and M. Eremets, *Nanotubes in boron nitride laser heated at high pressure*, Applied physics (1996).

[57] R. S. Lee, J. Gavillet, M. L. de la Chapelle, A. Loiseau, J.-L. Cochon, D. Pigache, J. Thibault, and F. Willaime, *Catalyst-free synthesis of boron nitride single-wall nanotubes with a preferred zig-zag configuration*, Phys. Rev. B **64**, 121405(R) (2001).

[58] C. Zhi, Y. Bando, C. Tan, and D. Golberg, *Effective precursor for high yield synthesis of pure BN nanotubes*, Solid State Communications **135**, 67 (2005).

[59] C. Tang, Y. Bando, T. Sato, and K. Kurashima, *A novel precursor for synthesis of pure boron nitride nanotubes*, Chemical Communications , 1290 (2002).

[60] Y. Huang, J. Lin, C. Tang, Y. Bando, C. Zhi, T. Zhai, B. Dierre, T. Sekiguchi, and D. Golberg, *Bulk synthesis, growth mechanism and properties of highly pure ultrafine boron nitride nanotubes with diameters of sub-10 nm*, Nanotechnology **22**, 145602 (2011).

[61] O. Stephan, *Formation of small single-layer and nested BN cages under electron irradiation of nanotubes and bulk material*, Applied Physics A-Materials Science & Processing **67**, 1071 (1998).

[62] D. Goldberg, Y. Bando, O. Stephan, and K.Kurashima, *Octahedral boron nitride fullerenes formed by electron beam irradiation*, Appl. Phys. Lett. **73**, 2441 (1998).

[63] P. W. Fowler, K. M. Rogers, G. Seifert, M. Terrones, and H. Terrones, *Pentagonal rings and nitrogen excess in fullerene-based BN cages and nanotube caps*, Chemical Physics Letters **299**, 359 (1999).

[64] A. Nagashima, N. Tejima, Y. Gamou, T. Kawai, and C. Oshima, *Electronic Structure of Monolayer Hexagonal Boron Nitride Physisorbed on Metal Surfaces*, Physical Review Letters **75**, 3918 (1995).

[65] D. PacilJ. C. Meyer, . . Girit, and A. Zettl, *The two-dimensional phase of boron nitride: Few-atomic-layer sheets and suspended membranes*, Applied Physics Letters **92**, 133107 (2008).

[66] K. S. Novoselov and A. H. C. Neto, *Two-dimensional crystals-based heterostructures: materials with tailored properties*, Phys. Scr. **2012**, 014006 (2012).

[67] W. S. Hummers and R. E. Offeman, *Preparation of Graphitic Oxide*, Journal of the American Chemical Society **80**, 1339 (1958).

[68] J. N. Coleman et al., *Two-Dimensional Nanosheets Produced by Liquid Exfoliation of Layered Materials*, Science **331**, 568 (2011).

[69] A. Balan, R. Kumar, M. Boukhicha, O. Beyssac, J.-C. Bouillard, D. Taverna, W. Sacks, M. Marangolo, E. Lacaze, R. Gohler, W. Escoffier, J.-M. Poumirol, and A. Shukla, *Anodic bonded graphene*, Journal of Physics D: Applied Physics **43**, 374013 (2010).

[70] J. Zupan, *Energy Bands in Boron Nitride and Graphite*, Physical Review B **6**, 2477 (1972).

[71] A. Catellani, M. Posternak, A. Baldereschi, H. J. F. Jansen, and A. J. Freeman, *Electronic interlayer states in hexagonal boron nitride*, Physical Review B **32**, 6997 (1985).

[72] X. Blase, A. Rubio, S. Louie, and M. Cohen, *Quasiparticle band structure of bulk hexagonal boron nitride and related systems*, Physical Review B **51**, 6868 (1995).

[73] B. Arnaud, S. Lebe, P. Rabiller, and M. Alouani, *Huge Excitonic Effects in Layered Hexagonal Boron Nitride*, Physical Review Letters **96**, 026402 (2006).

[74] L. Wirtz, A. Marini, M. Gruning, and A. Rubio, *Excitonic effects in optical absorption and electron-energy loss spectra of hexagonal boron nitride*, arXiv:cond-mat/0508421 (2005), arXiv: cond-mat/0508421.

[75] S. Larach and R. E. Shrader, *Electroluminescence from Boron Nitride*, Physical Review **102**, 582 (1956).

[76] S. Larach and R. E. Shrader, *Multiband Luminescence in Boron Nitride*, Physical Review **104**, 68 (1956).

[77] R. Geick, C. H. Perry, and G. Rupprecht, *Normal Modes in Hexagonal Boron Nitride*, Physical Review **146**, 543 (1966).

[78] A. Zunger, A. Katzir, and A. Halperin, *Optical properties of hexagonal boron nitride*, Physical Review B **13**, 5560 (1976).

[79] C. A. T. Ii, S. W. Brown, V. Subramaniam, S. Kidner, S. C. Rand, and R. Clarke, *Observation of near band gap luminescence from boron nitride films*, Applied Physics Letters **65**, 1251 (1994).

[80] G. H. Wannier, *The Structure of Electronic Excitation Levels in Insulating Crystals*, Physical Review **52**, 191 (1937).

[81] A. Marini, *Ab Initio Finite-Temperature Excitons*, Physical Review Letters **101**, 106405 (2008).

[82] R. Arenal, O. Stan, M. Kociak, D. Taverna, A. Loiseau, and C. Colliex, *Electron energy loss spectroscopy measurement of the optical gaps on individual boron nitride single-walled and multiwalled nanotubes*, Physical Review Letters **95**, 127601 (2005).

[83] C. Zhi, Y. Bando, C. Tang, D. Golberg, R. Xie, and T. Sekigushi, *Phonon characteristics and cathodolumininescence of boron nitride nanotubes*, Applied Physics Letters **86**, 3110 (2005).

[84] J. S. Lauret, R. Arenal, F. Ducastelle, A. Loiseau, M. Cau, B. Attal-Tretout, E. Rosencher, and L. Goux-Capes, *Optical transitions in single-wall boron nitride nanotubes*, Physical Review Letters **94**, 037405 (2005).

[85] John Spence, *Advanced Computing in Electron Microscopy, Earl J. Kirkland 1998. Plenum Press, New York and London. 260 pages. ($72.50)*, Microscopy and Microanalysis **5**, 371 (1999).

[86] A. Zobelli, A. Gloter, C. P. Ewels, G. Seifert, and C. Colliex, *Electron knock-on cross section of carbon and boron nitride nanotubes*, Phys. Rev. B **75**, 245402 (2007).

[87] A. Losquin, *Surface Plasmon modes revealed by fast electron based spectroscopies : from simple model to complex*, PhD thesis, Universitaris Sud - Paris XI, 2013.

[88] M. Kociak, O. Stan, M. G. Walls, M. Tencand C. Colliex, Spatially resolved EELS: The spectrum-imaging technique and its applications, in *Scanning Transmission Electron Microscopy*, edited by S. J. Pennycook and P. D. Nellist, pages 163–205, Springer New York, 2011.

[89] F. J. Garc´ de Abajo, *Optical excitations in electron microscopy*, Rev. Mod. Phys. **82**, 209 (2010).

[90] B. Yacobi and D. Holt, *Cathodoluminescence Microscopy of Inorganic Solids*, Springer US, 1990.

[91] L. F. Zagonel, S. Mazzucco, M. Tence, K. March, R. Bernard, B. Laslier, G. Jacopin, M. Tchernycheva, L. Rigutti, F. H. Julien, R. Songmuang, and M. Kociak, *Nanometer Scale Spectral Imaging of Quantum Emitters in Nanowires and Its Correlation to Their Atomically Resolved Structure*, Nano Lett. **11**, 568 (2011).

[92] U. Jahn, J. Ristic, and E. Calleja, *Cathodoluminescence spectroscopy and imaging of GaN/(Al,Ga)N nanocolumns containing quantum disks*, Applied Physics Letters **90**, 161117 (2007).

[93] M. Grundmann, J. Christen, N. N. Ledentsov, J. Ber, D. Bimberg, . Ruvimov, S. S., P. Werner, U. Richter, U. Gle, J. Heydenreich, V. M. Ustinov, A. Y. Egorov, A. E. Zhukov, P. S. Kop'ev, and Z. I. Alferov, *Ultranarrow Luminescence Lines from Single Quantum Dots*, Phys. Rev. Lett. **74**, 4043 (1995).

[94] J. RodriguezViejo, K. F. Jensen, H. Mattoussi, J. Michel, B. O. Dabbousi, and M. G. Bawendi, *Cathodoluminescence and photoluminescence of highly luminescent CdSe/ZnS quantum dot composites*, Applied Physics Letters **70**, 2132 (1997).

[95] M. Kociak, O. Stéphan, A. Gloter, L. F. Zagonel, L. H. Tizei, M. Tencé, K. March, J. D. Blazit, Z. Mahfoud, A. Losquin, and others, *Seeing and measuring in colours: Electron microscopy and spectroscopies applied to nano-optics*, Comptes Rendus Physique **15**, 158 (2014).

[96] M. T. M. Kociak, L.F. Zagonel and S. Mazzucco, Systeme de detection de cathodoluminescence reglable et microscope mettant en oeuvre un tel systeme.

[97] C. TencC. Jeanguillaume, *Electron-Energy-Loss Spectrometry Mapping*, Mikrochim. Acta **28**, 114 (1984).

[98] JEANGUILLAUME, *Spectrum-Image - The Next Step In Eels Digital Acquisition And Processing*, Ultramicroscopy **28**, 2527 (1989).

[99] E. Knill, R. Laflamme, and G. J. Milburn, *A scheme for efficient quantum computation with linear optics*, Nature **409**, 46 (2001).

[100] C. K. Law and H. J. Kimble, *Deterministic generation of a bit-stream of single-photon pulses*, Journal of Modern Optics **44**, 2067 (1997).

[101] F. De Martini, O. Jedrkiewicz, and P. Mataloni, *Generation of quantum photon states in an active microcavity trap*, Journal of Modern Optics **44**, 2053 (1997).

[102] M. Fsch, J. U. Ft, C. Wittmann, D. Strekalov, A. Aiello, M. V. Chekhova, C. Silberhorn, G. Leuchs, and C. Marquardt, *A versatile source of single photons for quantum information processing*, Nature Communications **4**, 1818 (2013).

[103] L. H. G. Tizei and M. Kociak, *Spatially Resolved Quantum Nano-Optics of Single Photons Using an Electron Microscope*, Physical Review Letters **110**, 153604 (2013).

[104] K. Watanabe, T. Taniguchi, T. Kuroda, and H. Kanda, *Band-edge luminescence of deformed hexagonal boron nitride single crystals*, Diamond Relat. Mater. **15**, 1891 (2006).

[105] P. Jaffrennou, J. Barjon, T. Schmid, L. Museur, A. Kanaev, J.-S. Lauret, C. Y. Zhi, C. Tang, Y. Bando, D. Golberg, B. Attal-Tretout, F. Ducastelle, and A. Loiseau, *Near-band-edge recombinations in multiwalled boron nitride nanotubes: Cathodoluminescence and photoluminescence spectroscopy measurements*, Phys. Rev. B **77**, 235422 (2008).

[106] A. Pierret, J. Loayza, B. Berini, A. Betz, B. Plas, F. Ducastelle, J. Barjon, and A. Loiseau, *Excitonic recombinations in h-BN: From bulk to exfoliated layers*, Physical Review B **89**, 035414 (2014).

[107] K. Watanabe, T. Taniguchi, T. Kuroda, and H. Kanda, *Effects of deformation on band-edge luminescence of hexagonal boron nitride single crystals*, Appl. Phys. Lett. **89**, 141902 (2006).

[108] P. Jaffrennou, J. Barjon, J. S. Lauret, B. Attal-Trétout, F. Ducastelle, and A. Loiseau, *Origin of the excitonic recombinations in hexagonal boron nitride by spatially resolved cathodoluminescence spectroscopy*, J. Appl. Phys. **102**, 116102 (2007).

[109] K. Watanabe and T. Taniguchi, *Jahn-Teller effect on exciton states in hexagonal boron nitride single crystal*, Physical Review B **79**, 193104 (2009).

[110] M. I. Heggie, I. Suarez-Martinez, C. Davidson, and G. Haffenden, *Buckle, ruck and tuck: A proposed new model for the response of graphite to neutron irradiation*, J. Nucl. Mater. **413**, 150 (2011).

[111] A. W. Robertson, A. Bachmatiuk, Y. A. Wu, F. Schäffel, B. Büchner, M. H. Rümmeli, and J. H. Warner, *Structural Distortions in Few-Layer Graphene Creases*, ACS Nano **5**, 9984 (2011).

[112] K. Kim, Z. Lee, B. D. Malone, K. T. Chan, B. Alemán, W. Regan, W. Gannett, M. F. Crommie, M. L. Cohen, and A. Zettl, *Multiply folded graphene*, Phys. Rev. B **83**, 245433 (2011).

[113] L.-L. He, M. Akaishi, and S. Horiuchi, *Structural evolution in boron nitrides during the hexagonal-cubic phase transition under high pressure at high temperature*, Microsc. Res. Tech. **40**, 243 (1998).

[114] L. Nistor, G. Van Tendeloo, and G. Dinca, *Crystallographic aspects related to the high pressure–high temperature phase transformation of boron nitride*, Philos. Mag. **85**, 1145 (2005).

[115] K. Kim, Z. Lee, B. D. Malone, K. T. Chan, B. Alem W. Regan, W. Gannett, M. F. Crommie, M. L. Cohen, and A. Zettl, *Multiply folded graphene*, Phys. Rev. B **83**, 245433 (2011).

[116] Y. Zheng, N. Wei, Z. Fan, L. Xu, and Z. Huang, *Mechanical properties of grafold: a demonstration of strengthened graphene*, Nanotechnology **22**, 405701 (2011).

[117] A. Castellanos-Gomez, H. S. J. van der Zant, and G. A. Steele, *Folded MoS2 layers with reduced interlayer coupling*, arXiv:1309.4433 [cond-mat] (2013), arXiv: 1309.4433.

[118] A. Celik-Aktas, J.-M. Zuo, J. F. Stubbins, C. Tang, and Y. Bando, *Double-helix structure in multiwall boron nitride nanotubes*, Acta Cryst. A **61**, 533 (2005).

[119] D. Golberg, M. Mitome, Y. Bando, C. Tang, and C. Zhi, *Multi-walled boron nitride nanotubes composed of diverse cross-section and helix type shells*, Appl. Phys. A **88**, 347 (2007).

[120] N. Marom, J. Bernstein, J. Garel, A. Tkatchenko, E. Joselevich, L. Kronik, and O. Hod, *Stacking and Registry Effects in Layered Materials: The Case of Hexagonal Boron Nitride*, Phys. Rev. Lett. **105**, 046801 (2010).

[121] J. Yin, M. Hu, Z. Yu, C. Zhang, L. Sun, and J. Zhong, *Direct or indirect semiconductor: The role of stacking fault in h-BN*, Physica B **406**, 2293 (2011).

[122] G. Constantinescu, A. Kuc, and T. Heine, *Stacking in Bulk and Bilayer Hexagonal Boron Nitride*, Phys. Rev. Lett. **111**, 036104 (2013).

[123] A. Shmeliov, J. S. Kim, K. B. Borisenko, P. Wang, E. Okunishi, M. Shannon, A. I. Kirkland, P. D. Nellist, and V. Nicolosi, *Impurity induced non-bulk stacking in chemically exfoliated h-BN nanosheets*, Nanoscale **5**, 2290 (2013).

[124] Y.-I. Kim, J. K. Jung, K.-S. Ryu, S.-H. Nahm, and D. H. Gregory, *Quantitative phase analysis of boron nitride nanotubes using Rietveld refinement*, Journal of Physics D: Applied Physics **38**, 1127 (2005).

[125] D. Golberg, M. Mitome, Y. Bando, C. C. Tang, and C. Y. Zhi, *Multi-walled boron nitride nanotubes composed of diverse cross-section and helix type shells*, Applied Physics A **88**, 347 (2007).

[126] J. M. Z. Ayten Celik-Aktas, *Double-helix structure in multiwall boron nitride nanotubes.*, Acta crystallographica. Section A, Foundations of crystallography **61**, 533 (2005).

[127] A. Pierret, *Propris structurales et optiques de nanostructures III-N semiconductrices rand gap : nanofils d'AlxGa1-xN synthspar taxie par jets mollaires et nanostructures de nitrure de bore.*, PhD thesis, Universitierre et Marie Curie - Paris VI, 2013.

[128] P. Jaffrennou, *Etude des propris optiques du nitrure de bore hexagonal et des nanotubes de nitrure de bore*, PhD thesis, le normale supeure de Cachan - ENS Cachan, 2008.

[129] L. Museur and A. Kanaev, *Near band-gap photoluminescence properties of hexagonal boron nitride*, Journal of Applied Physics **103**, 103520 (2008).

[130] J. Yu, Y. I. Chen, L. Li, B.-m. Cheng, and D. Yu, *Synchrotron Photoluminescence Spectroscopy of Boron Nitride Nanotubes with Different Metal Impurities*, MRS Online Proceedings Library **1204**, null (2009).

[131] P. Jaffrennou, F. Donatini, J. Barjon, J.-S. Lauret, A. Maguer, B. Attal-Tretout, F. Ducastelle, and A. Loiseau, *Cathodoluminescence imaging and spectroscopy on a single multiwall boron nitride nanotube*, Chemical physics letters **442**, 372 (2007).

[132] J. Yu, D. Yu, Y. Chen, H. Chen, M.-Y. Lin, B.-M. Cheng, J. Li, and W. Duan, *Narrowed bandgaps and stronger excitonic effects from small boron nitride nanotubes*, Chemical Physics Letters **476**, 240 (2009).

[133] C.-Y. Su, W.-Y. Chu, Z.-Y. Juang, K.-F. Chen, B.-M. Cheng, F.-R. Chen, K.-C. Leou, and C.-H. Tsai, *Large-Scale Synthesis of Boron Nitride Nanotubes with Iron-Supported Catalysts*, The Journal of Physical Chemistry C **113**, 14732 (2009).

[134] Y. C. Lu Hua Li, *Single deep ultraviolet light emission from boron nitride nanotube film*, Applied Physics Letters **97**, 141104 (2010).

[135] Y. Huang, J. Lin, C. Tang, Y. Bando, C. Zhi, T. Zhai, B. Dierre, T. Sekiguchi, and D. Golberg, *Bulk synthesis, growth mechanism and properties of highly pure ultrafine boron nitride nanotubes with diameters of sub-10 nm*, Nanotechnology **22**, 145602 (2011).

[136] S. Larach and R. E. Shrader, *Electroluminescence from Boron Nitride*, Phys. Rev. **102**, 582 (1956).

[137] S. Larach and R. E. Shrader, *Multiband Luminescence in Boron Nitride*, Phys. Rev. **104**, 68 (1956).

[138] J. Kotakoski, C. H. Jin, O. Lehtinen, K. Suenaga, and A. V. Krasheninnikov, *Electron knock-on damage in hexagonal boron nitride monolayers*, Phys. Rev. B **82**, 113404 (2010).

[139] A. Zobelli, A. Gloter, C. P. Ewels, G. Seifert, and C. Colliex, *Electron knock-on cross section of carbon and boron nitride nanotubes*, Phys. Rev. B **75**, 245402 (2007).

[140] J. Kotakoski, C. H. Jin, O. Lehtinen, K. Suenaga, and A. V. Krasheninnikov, *Electron knock-on damage in hexagonal boron nitride monolayers*, Phys. Rev. B **82**, 113404 (2010).

[141] C. Attaccalite, L. Wirtz, A. Marini, and A. Rubio, *Efficient Gate-tunable light-emitting device made of defective boron nitride nanotubes: from ultraviolet to the visible*, Sci. Rep. **3** (2013).

[142] L. H. Li, J. Cervenka, K. Watanabe, T. Taniguchi, and Y. Chen, *Strong Oxidation Resistance of Atomically Thin Boron Nitride Nanosheets*, ACS Nano **8**, 1457 (2014).

[143] Q. L. Liu, F. F. Xu, and T. Tanaka, *Visible emission from N-rich turbostratic boron nitride thin films doped with Eu, Tb, and Tm*, Applied Physics Letters **81**, 3948 (2002).

[144] S. Castelletto, B. C. Johnson, V. Iv, N. Stavrias, T. Umeda, A. Gali, and T. Ohshima, *A silicon carbide room-temperature single-photon source*, Nat Mater **13**, 151 (2014).

[145] Y. Wu, M. G. Payne, E. W. Hagley, and L. Deng, *Ultraviolet single-photons on demand and entanglement of photons with a large frequency difference*, Phys. Rev. A **70**, 063812 (2004).

[146] R. H. Hadfield, *Single-photon detectors for optical quantum information applications*, Nat Photon **3**, 696 (2009).

[147] J.-H. Kim, Y.-H. Ko, S.-H. Gong, S.-M. Ko, and Y.-H. Cho, *Ultrafast single photon emitting quantum photonic structures based on a nanoobelisk*, Sci. Rep. **3** (2013).

[148] K. L. Kliewer and R. Fuchs, Adv. Chem. Phys. **27**, 355 (1974).

[149] O. S. R. Arenal, *EELS measurements in single wall Boron Nitride nanotubes*, AIP Conference Proceedings **723**, 293 (2004).

[150] C. T. Pan, R. R. Nair, U. Bangert, Q. Ramasse, R. Jalil, R. Zan, C. R. Seabourne, and A. J. Scott, *Nanoscale electron diffraction and plasmon spectroscopy of single- and few-layer boron nitride*, Phys. Rev. B **85**, 045440 (2012).

[151] L. Liu, Y. Feng, and Z. Shen, *Structural and electronic properties of h-BN*, Phys. Rev. B **68**, 104102 (2003).

[152] Y. Li, Y. Rao, K. F. Mak, Y. You, S. Wang, C. R. Dean, and T. F. Heinz, *Probing Symmetry Properties of Few-Layer MoS2 and h-BN by Optical Second-Harmonic Generation*, Nano Lett. **13**, 3329 (2013).

[153] C.-J. Kim, L. Brown, M. W. Graham, R. Hovden, R. W. Havener, P. L. McEuen, D. A. Muller, and J. Park, *Stacking Order Dependent Second Harmonic Generation and Topological Defects in h-BN Bilayers*, Nano Lett. **13**, 5660 (2013).

[154] M. Grüning and C. Attaccalite, *Second harmonic generation in BN and MoS_2 monolayers: Role of electron-hole interaction*, Phys. Rev. B **89**, 081102 (2014).

[155] A. Castellanos-Gomez, M. Buscema, R. Molenaar, V. Singh, L. Janssen, S. J. d. Z. van Herre, and G. A. Steele, *Deterministic transfer of two-dimensional materials by all-dry viscoelastic stamping*, 2D Materials **1**, 011002 (2014).

[156] R. M. Erasmus and J. D. Comins, *Photoluminescence spectroscopy of electron-irradiation induced defects in cubic boron nitride (cBN)*, phys. stat. sol. (c) **1**, 2269 (2004).

[157] D. A. Evans, A. G. McGlynn, B. M. Towlson, M. Gunn, D. Jones, T. E. Jenkins, R. Winter, and N. R. J. Poolton, *Determination of the optical band-gap energy of cubic and hexagonal boron nitride using luminescence excitation spectroscopy*, J. Phys.: Condens. Matter **20**, 075233 (2008).